

Jagiellonian University  
Faculty of Physics, Astronomy and Applied Computer Science

---

**Optical spectral states of blazars and their relation to VHE  
gamma ray emission in PKS 2155-304**

by

Alicja Wierzholska

A thesis, written under the supervision of  
Professor Michał Ostrowski,  
submitted to the Jagiellonian University  
for the degree of Doctor of Philosophy in Astronomy

Kraków 2013

*To my husband.*



# Acknowledgments

First of all I would like to thank my supervisor Professor Michał Ostrowski for all the time and attention he devoted to the project presented in this dissertation, for all his comments, valuable advice, suggestions and deeply inspiring discussions.

I would also like thank dr Łukasz Stawarz for many fruitful discussions, enlightening comments, helpful suggestions and valuable ideas he shared with me.

Furthermore, I would like to give many thanks to Professor Stefan Wagner for sharing with me his knowledge, for all scientific and highly valuable discussions and also for all his optimism!

I am also very grateful to many scientists with whom I have met during my astrophysical research: dr Michał Dyrda, dr Anna Szostek – my first tutors of the very high energy data analysis and interpretation techniques, dr Yves Gallant, dr Fabio Acero and dr Anna Zajczyk – for all their help, support and knowledge they share with me during my visit in Montpellier.

Many special thanks go to people from Heidelberg Landessternwarte: dr Marcus Hauser, Gabriele Cologna and Felix Jankowsky for an exhaustive introduction to optical data analysis, a lot of help in my first steps with ATOM data and great a atmosphere during my stay in Heidelberg. I would also like to thank all scientists from the H.E.S.S. Collaboration for many constructive remarks to all projects in which I was involved.

Furthermore I acknowledge the financial supports from Ministry of Science and Higher Education and the National Science Center (grants No. 2011/03/N/ST9/01867, 745/N-HESS-MAGIC/2010/0). Financial aid was also kindly provided within Smoluchowski Scholarship.

This research has made use of data from the OVRO 40-m monitoring program (Richards et al. 2011), which is supported in part by NASA grants NNX08AW31G and NNX11A043G, and NSF grants AST-0808050 and AST-1109911.



# Contents

## Contents

<b>1</b>	<b>Introduction</b>	<b>1</b>
<b>2</b>	<b>Active Galactic Nuclei</b>	<b>3</b>
2.1	Overview . . . . .	3
2.1.1	Seyfert type galaxies . . . . .	6
2.1.2	Radio-quiet quasars . . . . .	6
2.1.3	Fanaroff-Riley type galaxies . . . . .	7
2.1.4	Steep Spectrum Radio Quasars . . . . .	7
2.1.5	Blazars . . . . .	7
2.2	Emission models for blazars . . . . .	8
2.3	Optical color-magnitude relation for blazars . . . . .	10
2.4	PKS 2155-304 . . . . .	11
<b>3</b>	<b>VHE Gamma-ray Astronomy</b>	<b>13</b>
3.1	Gamma Radiation . . . . .	13
3.2	Gamma-ray Initiated Air Showers . . . . .	14
3.2.1	Electromagnetic Cascade . . . . .	15
3.2.2	Hadronic Cascade . . . . .	15
3.2.3	Cherenkov Emission . . . . .	17
3.3	High Energy Stereoscopic System (H.E.S.S.) . . . . .	18
3.3.1	Telescope construction . . . . .	19
3.3.2	H.E.S.S.II . . . . .	20
3.3.3	H.E.S.S. data analysis . . . . .	20
3.4	Automatic Telescope for Optical Monitoring . . . . .	28
<b>4</b>	<b>Optical observations of blazars</b>	<b>30</b>
4.1	Analyzed objects . . . . .	30
4.2	Color-magnitude diagrams and variability . . . . .	31
4.3	Multiwavelength properties of the ATOM blazars . . . . .	56

## CONTENTS

<b>5</b>	<b>H.E.S.S. observations of PKS 2155-304</b>	<b>63</b>
5.1	Selected observations . . . . .	63
5.2	Light curves and variability . . . . .	65
5.3	The relation of gamma-ray and optical fluxes . . . . .	69
5.4	Gamma-ray spectra and gamma-optical SEDs . . . . .	76
<b>6</b>	<b>Discussion and Summary</b>	<b>80</b>
6.1	Optical monitoring of the blazars . . . . .	80
6.2	Multiwavelength properties of the blazars . . . . .	85
6.3	Observations of PKS 2155-304 . . . . .	85
<b>7</b>	<b>Outlook</b>	<b>87</b>
	<b>Appendices</b>	<b>89</b>
<b>A</b>	<b>Color coding in color-magnitude diagrams</b>	<b>90</b>
<b>B</b>	<b>Error estimation for the Pearson's correlation coefficient</b>	<b>92</b>
<b>C</b>	<b>Optical spectral index</b>	<b>94</b>
<b>D</b>	<b>Proposal description</b>	<b>95</b>
	<b>Bibliography</b>	<b>96</b>
	<b>List of Tables</b>	<b>103</b>
	<b>List of Figures</b>	<b>104</b>



# Introduction

Blazars are radio-loud Active Galactic Nuclei (AGNs) with relativistic jets pointing at a small (of a few degree) angle to the observer. Their variable emission is observed in a wide energy range: from radio frequencies up to very high energy gamma-rays. Spectra of blazars are dominated by non-thermal emission with a double-humped structure in the spectral energy distribution (SED). The first component in SED is usually explained as synchrotron radiation of relativistic electrons, but the interpretation of the second one is still a matter of debate and may differ from sources to source. Simultaneous multi-wavelength observations, covering the most energetic part of the spectrum in particular, are essential for the modeling of the physical processes responsible for the emission of blazars. This dissertation presents the analysis of the optical observations of 30 BL Lac type blazars conducted by the Automatic Telescope for Optical Monitoring (ATOM). The mean optical luminosities are compared with quasi-simultaneous radio and high energy gamma-ray ones. Finally, a detailed investigation of a relation between Very High Energy (VHE) gamma-ray and optical emission is done for one object from the sample, namely PKS 2155-304, based on the observations gathered by H.E.S.S. and ATOM. The thesis includes extensive observational studies of blazars but does not involve any modeling.

The data analysis and interpretative part of the dissertation is preceded by a short presentation of Active Galactic Nuclei, their unified model and types, blazars and their emission models in particular (Chapter 2). In Chapter 3 the basics of VHE gamma-ray astronomy are introduced, including a brief description of gamma-ray induced air showers and the Cherenkov detection technique. Moreover, this chapter presents are presented: the H.E.S.S. experiment, its calibration and data analysis and the Automatic Telescope for Optical Monitoring.

The results include an outcome of a long-term optical monitoring in two bands ( $B$  and  $R$ ) done by the ATOM telescope, presented in Chapter 4, involving 30 BL Lac type blazars observed in the period of 2007-2012. In the case of 14 analyzed sources the

"bluer-when-brighter" trend is observed. Remaining objects from the sample show more complex color-magnitude relation, and, in particular, in a few cases separate branches, which correspond to different spectral states, are visible in the color-magnitude diagrams.

Then, Chapter 5 of the dissertation presents a detailed analysis of emissions in the optical band and in the VHE gamma-rays of PKS 2155-304. It is the brightest VHE blazar in the Southern Hemisphere and has been frequently observed by H.E.S.S. since 2004. The analysis of the color-magnitude diagram for PKS 2155-304 does not show general color-magnitude correlation, but it reveals a complex structure in the plot, including two separate substructures ("branches") with a significant bluer-when-brighter correlation within each one of them. The study of the simultaneous observations in the optical and VHE gamma-rays ranges, strongly suggests an existence of a correlation between these two bands, which is even more significant when considering the data for the upper branch. The lower branch data reveal a high-soft state of the blazar, with very bright optical emission, but weak VHE flux. In the final Chapters 6 and 7 the results are discussed and summarized, and an outlook for future projects is presented.

# Active Galactic Nuclei

## 2.1 Overview

Active Galactic Nuclei (AGNs) form a class of sources including the brightest objects in the Universe. Their activity is related to the central engine hosting a supermassive black hole. The observed bolometric luminosities AGNs are between  $10^{40}$  erg s<sup>-1</sup> and  $10^{47}$  erg s<sup>-1</sup>. The class of AGNs includes very different objects. The attempt to build a consistent AGN picture, have led to an unified model (Urry & Padovani 1995). In their scheme a standard active galaxy consists of:

- **Super Masive Black hole**

A supermassive black hole ( $M_{\text{BH}} = 10^7$ - $10^9 M_{\odot}$ ) is located at the center of the AGN. Matter is accreted onto the black hole and in this process, gravitational potential energy is converted into radiation: thermal (e.g. from the disc) and non-thermal (e.g. from the jets). Usually the black hole mass scales with the luminosity and velocity dispersion of the bulge of the host galaxy (Bettoni et al. 2003).

- **Accretion disk**

The accretion disk in AGN is an optically thick disk surrounding the central black hole. The size of the disk is approximately 100-1000 Schwarzschild radii and the density of the disk is about  $10^{15}$  cm<sup>-3</sup>. The formation process of this part of AGN is closely related to the accretion phenomenon. The disk is formed by a gas swirling around a central black hole. The gravity of the central body attracts the matter, but before it can move to the vicinity of the black hole it needs to lose its angular momentum. It can be done by the viscosity processes, which transfer the angular momentum to the outer regions of the disk. One may note that in AGNs the accretion episodes may have angular momentum of the accreted matter uncorrelated with earlier or later episodes, unlike in e.g. accretion disks in binary stars.

- **Broad-line region** (BLR) produces lines from atomic transitions broadened by the Doppler effect. The characteristic widths of the broadening correspond to the velocities of few thousand  $\text{km s}^{-1}$ . The dynamics of these clouds is still unknown, but the gravitational influence of the central source is sufficient to estimate the black hole mass from their velocity dispersion. The surface of these clouds is illuminated by radiation from the accretion disk and the gas is ionized, with the most abundant ions: He III, O IV-VI, C III-IV. The internal part of the clouds is neutral and can be penetrated by X-ray photons. This part produces strong lines of H I, Mg II and Fe II. The size of the BLR scales with luminosity, both globally from object-to-object and in a particular source as the luminosity varies with time.
- **Narrow-line region** (NLR) is located within 3 pc from the center. The ionization is similar to the one in the BLR, but the velocities of the clouds are lower, within the about 200-2000  $\text{km s}^{-1}$ . The clouds are slightly less dense and they can be even optically thin in the hydrogen Lyman continuum. Under such circumstances radiation pressure force may be important and the line profiles may include non-gravitational components. On the average the optically thin gas is higher ionized than the thick gas, and this has an influence on the spectrum. Additionally, because of the low densities, the spectra include intense forbidden lines. The internal parts of the clouds are predicted to emit coronal lines, produced by fine-structure transitions, and observed mostly in infrared.
- **Torus** is made of dust and surrounds the accretion disk. It absorbs the emission from the central region and then re-emits the absorbed energy at the infrared frequencies.
- **Jets** are giant collimated plasma outflows from the centers of a radio-loud AGN, transporting energy, momentum and angular momentum from the central black hole over large distances (Blandford & Rees 1974). Complicated physical processes underlying energy dissipation and the emission mechanisms in jets are not well understood. Several fundamental questions about the structure and composition of jets (leptonic or hadronic), mechanisms of their formation, propagation processes, location of the emission sites in blazar jets or main energy dissipation processes leading to the observed emission are without the answers. Current observations suggest that in a few parsecs scale the jets are dominated by the Poynting flux, while further may be dominated by particle-dominated plasma (Sikora et al. 2005).

A simple illustration of the unified scheme is presented in Fig. 2.2. This model assumes that every AGN “fits” to this general layout and the orientation of the object determines the exact type of the observed source.

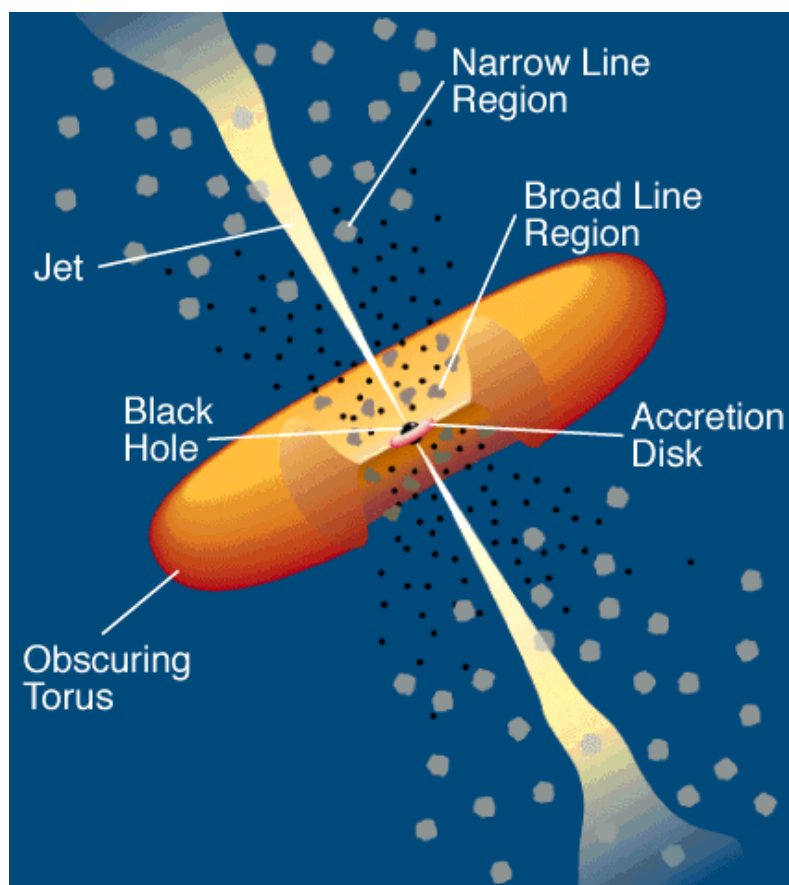


Figure 2.1: The AGN in unified scheme by Urry & Padovani (1995). The main ingredients of the active galaxy are presented: central black hole, accretion disk, broad lines region, narrow lines region, torus and jets. Credits: NASA<sup>1</sup>.

The unified model of AGNs divides sources into two main classes: radio-loud (Fanaroff-Riley type galaxies, steep spectrum radio quasars and blazars) and radio-quiet (Seyfert type galaxies and radio-quiet quasars). AGNs with strong radio emission are called radio-loud and they stand for only 10% of the whole population of AGNs (Kellermann et al. 1989). It is worth to mention that the division between radio-loud and radio-quiet sources is still a matter of debate (e.g. Sikora et al. 2007). Radio-loudness is described as a ratio of flux densities in the radio and the optical wavebands:  $R = \frac{F_{\text{radio}}}{F_{\text{optical}}}$ , also known as the loudness parameter. Kellermann et al. (1989) classified radio-loud objects as these with  $\frac{F_{\text{radio}(6\text{ cm})}}{F_{\text{optical}(440\text{ nm})}} \geq 10$ . The origin of radio emission in the case of radio-loud sources seems to be well understood, but the case of radio-quiet sources is not well established. The characteristic features of mentioned AGNs' classes are briefly described below.

<sup>1</sup><http://heasarc.gsfc.nasa.gov/docs/cgro/images/epo/gallery/agns/index.html>

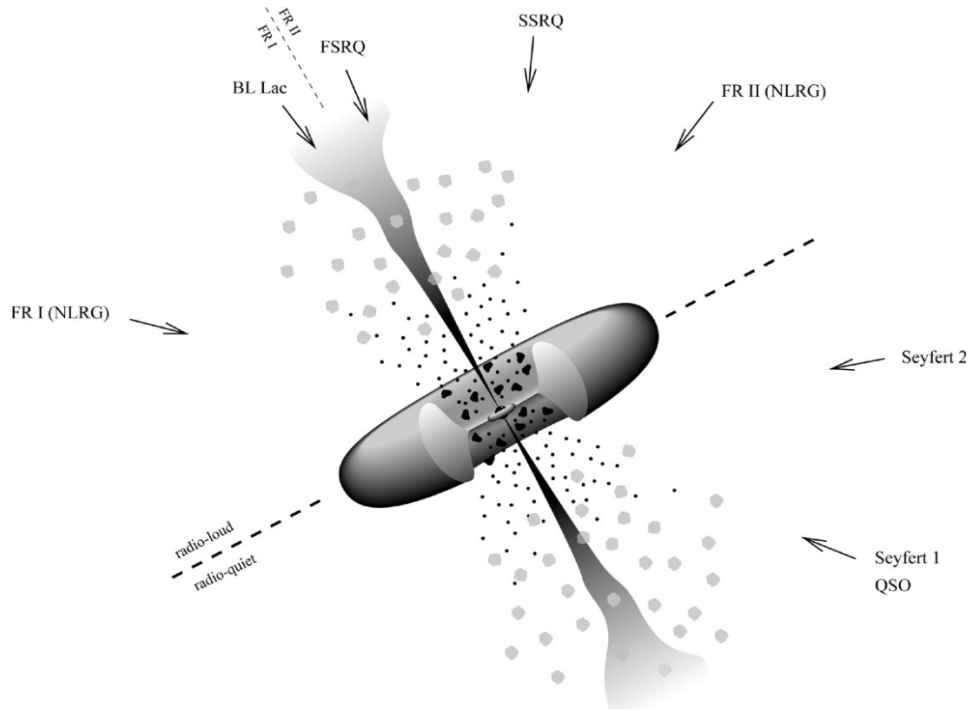


Figure 2.2: The unified scheme of AGN by Urry & Padovani (1995). The main types of the observed AGNs, depending of the inclination angle, are presented. Credits: Padovani (1997).

### 2.1.1 Seyfert type galaxies

Seyfert type galaxies are AGNs categorized as low-luminosity ( $M_{B\text{-band}} > -23$  mag) (Schmidt & Green 1983) and radio-quiet (Kellermann et al. 1989). These sources are divided into two classes: Seyfert I (Sy I) and Seyfert II type galaxies (Sy II). The difference in the classification depends upon whether the spectra show narrow and broad emission lines (type I), or only narrow lines (type II). In the unification scheme the Seyfert I and II galaxies are supposed to be the same population of objects, with different observational properties caused by the dusty molecular obscuring material having a torus-like geometry around the AGN. Radio-quiet sources such as Seyfert galaxies are much fainter at the radio wavelengths with the emission observed in the sub kiloparsecs scales.

### 2.1.2 Radio-quiet quasars

The classes of radio-loud and radio quiet quasars (RLQs and RQQs, respectively) differ in their radio properties, and in the luminosity of their host galaxy (e.g. Dunlop et al. 2003; Falomo et al. 2004). The host galaxy of RLQs is usually more luminous than of RQQs. This group of AGNs is similar to Seyfert type I galaxies, but they are more luminous. Like the Seyferts, RQQs emit a weak radio emission, the ones located at  $z < 0.3$ , can be often detected at radio frequencies with the mJy flux level.

### 2.1.3 Fanaroff-Riley type galaxies

Fanaroff & Riley (1974) proposed a classification of radio galaxies based on their different morphological properties. Fanaroff-Riley type I sources (FR-I) are those which luminosities decrease with distance from the central galaxy, while Fanaroff-Riley type II sources (FR-II) exhibit increasing luminosity in the lobes. At small redshifts ( $z < 0.5$ ) FR-I type sources are found to be located in dense environments like galaxy clusters, while FR-II type sources are usually hosted by field galaxies. At higher redshifts FR-I and FR-II sources are located in rich intergalactic environment (Hill & Lilly 1991). Fanaroff-Riley sources are hosted by elliptical galaxies. Host galaxy of FR-II are less massive than in the cases of FR-I sources (Owen 1993; Govoni et al. 2000). The difference between type I and type II objects is also noticeable in their optical spectra. The emission lines, which are observed in FR-II galaxies are only rarely visible in the spectra of FR-I (Govoni et al. 2000).

### 2.1.4 Steep Spectrum Radio Quasars

Steep Spectrum Radio Quasars (SSRQs) form a radio-loud type of AGNs. They are usually lobe-dominated, i.e. the radio lobe emission dominates over the radio core emission. Jets in SSRQs are viewed at larger angles than it is in the case of blazars and the beaming effects in jets are not strong (Liu et al. 2006). For SSRQs jet emission is not expected to dominate at optical bands (e.g. Gu & Ai 2011). The observational properties of SSRQs classify them between FSRQs (see below) and radio-quiet quasars in the discussed AGNs framework.

### 2.1.5 Blazars

Blazars are radio-loud AGNs with relativistic jets pointing at small angles to the line of sight (e.g. Blandford & Rees 1978; Begelman et al. 1984; Urry 1999). The emission of blazars is produced predominantly by non-thermal processes. Blazars are observed at wide range of frequencies of the electromagnetic spectrum from radio to X-rays, and in the case of the most energetic sources, up to very high energy gamma rays (e.g. Gupta et al. 2008; Wagner 2009; Vercellone et al. 2011; Giommi et al. 2012). Up to now almost 50 blazars have been identified as TeV sources<sup>2</sup>. The variability of blazars is observed on different timescales from years down to minutes and at different wavelengths (e.g. Wagner & Witzel 1995). Blazars split into two subclasses: the Flat Spectrum Radio Quasars (FSRQs) and the BL Lacertae type objects (BL Lacs) (Urry 1999). In the FSRQs broad or narrow emission lines are observed, while BL Lacs do not show lines in their spectra.

---

<sup>2</sup><http://tevcat.uchicago.edu>

Spectral energy distribution (SED) of blazars is characterized by two distinct components manifesting as low- and high-energy bumps in the  $\nu - \nu F_\nu$  representation. The emission is explained mainly by non-thermal processes. The synchrotron, low-energy part of the spectrum (the first bump) often extends from radio up to X-ray frequencies, while the high-energy one, generated by Inverse Compton or/and hadronic processes is located between the X-ray and gamma-ray ranges. The group of BL Lac objects can be divided into three subtypes: low-, intermediate- and high-energy peak BL Lac objects (LBLs, IBLs and HBLs, respectively). The difference between these subclasses is in the position of the synchrotron peak in the SED. For IBLs the maximum is located at optical frequencies and if the maximum is found at lower or higher frequencies than in IBLs then we deal with LBLs and HBLs, respectively. The shape of the spectrum and peaks' location shows so-called "blazars sequence" (for review see Ghisellini & Tavecchio 2008), which starts from FSRQs, through the low and intermediate energy peak objects up to HBL type BL Lacs. Evolution of the sequence is characterized by the increasing peak frequencies and decreasing dominance of  $\gamma$ -ray emission over the low-frequencies, and decreasing bolometric luminosity.

## 2.2 Emission models for blazars

The double-bumped structure of blazars' SED is explained by several models and they mostly differ in the dominant mechanism explaining emission processes in the high energy range. The composition of the jet matter can be either leptonic or hadronic. One should be noted here, that currently there is no model or a group of models, which can explain the emission processes in all blazars. Therefore, it is important to observe such objects simultaneously in many energy ranges to constrain modeling of the blazar emission .

### Leptonic models

The established models for the broad-band blazar emission ascribe the low-energy spectral component to the synchrotron radiation of ultrarelativistic electrons accelerated within the inner parts of a magnetized jet (sub-parsec and parsec scales), and the high energy component to the Inverse-Compton (IC) emission of the same electron population, involving either jet synchrotron photons as seeds for the IC scattering ('synchrotron self-Compton' model, SSC) (e.g., Konigl 1981; Marscher & Gear 1985), or various photon fields originating outside of the jet ('external-Compton' models, EC). The external photons can come from the disk (e.g. Dermer & Schlickeiser 1993), Broad Line Region (e.g. Sikora et al. 1994; Ghisellini & Madau 1996) or dusty torus (e.g. Sikora 1994; Sikora et al. 2002). The emerging agreement is that the SSC model is the most appropriate model for blazars of the BL Lacertae type which accrete at lower rates and as such lack intense

circumnuclear photon fields, while the external-Compton scenarios are best applied in modeling FSRQs known for their high accretion rates and rich circumnuclear environment (see, e.g., Ghisellini et al. 2010).

In the simplest SSC model particles (electrons and positrons) are injected into a radiation region, which is assumed to be spherical blob, and they are moving in a uniform magnetic field. The energy distribution of the particles is described by the broken power-law function. SSC models are the simplest way for the spectrum modeling and were very popular in the past (e.g. see modelling by Maraschi et al. 1992; Ghisellini et al. 1998). It must be noted here that SSC models are rather simple including many simplifications and the number of models' free parameters is of the same order as the number of data points. The typical value of the magnetic field obtained from spectral fitting with SSC models is about 0.1 G and the Doppler factor is in the order of 10.

### **Hadronic models**

An alternative to the leptonic scenario is the hadronic one. Similarly, as in the case of the leptonic model, here also the first peak can be explained as synchrotron radiation. The difference is in the second bump. Hadronic models assume that the jet contains ultrarelativistic protons. Interactions with matter in the jet of these protons can produce the second  $\gamma$ -ray bump (Pohl & Schlickeiser 2000). However, the mentioned models, due to low density of plasma, are not able to explain the fast variability patterns during flares (Aharonian et al. 1999). The alternative was sought in interactions of protons accelerated to high energies, which are able to initiate pion production ('Proton-Induced Cascade' model, PIC). To fit this model to observations one need to assume the number of protons with very high Lorentz factors,  $\gamma_p > 10^{10}$ , which is difficult to explain in terms of the known acceleration processes (Aharonian 2000). Hadronic models also produce too soft X-ray spectrum (Mannheim & Biermann 1992).

### **Hybrid models**

The leptonic and hadronic models assume the idealized composition of blazars' jets: containing only leptonic or only hadronic particles. But, both types of particles can be involved in the emission processes. Simultaneous observations of outbursts in blazars, sometimes show the phenomenon known as "orphan TeV flare", when an outburst is observed in the TeV range without any contemporaneous X-ray flaring activity. This requires consideration of both leptonic and hadronic influences. The examples are Markarian 421 (Błażejowski et al. 2005) or 1ES 1959+650 (Krawczynski et al. 2004). These observations support the importance of hadronic processes in the case of objects for which spectral and temporal properties in their quiescent state can be well reproduced by the

SSC explanation. A few hybrid models were proposed e.g. by Atoyan & Dermer (2003), Pe'er & Waxman (2005), Reimer et al. (2005) or Böttcher (2005).

### 2.3 Optical color-magnitude relation for blazars

Optical observations of blazars allow us to study not only the flux variability, but also the color variations and color-magnitude relations for these sources. Such studies were provided for many objects. Carini et al. (1992) analyzed the optical variability of two blazars OJ 287 and BL Lacertae, observed over 10 years. The photometric monitoring does not show a strong relation between optical color and flux, but they found that sources become bluer when they are brighter.

Ghosh et al. (2000), in the monitoring of 15 objects, shows an indication for a correlation of the optical flux and color only in the case of one object, 3C 66A. A stronger relation between  $V - R$  color and  $R$  magnitude in BL Lacertae was found in 11 nights of observations in 1997 (Clements & Carini 2001). The correlation coefficient for the considered optical outburst is 0.73. Since then the similar relation between color and flux has been found in the faint state of S5 0716+714 (Ghisellini et al. 1997) and in the observations of AO 0235+164 (Raiteri et al. 2001). The long-term monitoring of BL Lacertae presented by Villata et al. (2002) and Villata et al. (2004) has shown bluer-when-brighter relation in this object, but it is observed only for short periods and is not visible in long-term observations.

Gu et al. (2006) reported that in the case of five blazars from the analyzed sample (including BL Lac type objects and FSRQs) the color-magnitude relation was noticed. The authors mention that in FSRQs redder-when-brighter relation is observed, while in the case of BL Lacs the bluer-when-brighter trend is visible. They found a strong positive color-magnitude correlation for: 3C 66A, S5 0716+71, BL Lacertae and a weak correlation for OJ 287 and PKS 0735+178.

Color behavior of OJ 287 during the flaring state was analyzed by Dai et al. (2011). The monitoring results obtained with 60/90 cm Schmidt Telescope on NAOC shows bluer-when-brighter chromatism. The authors considered observations from the years 2005-2006 and they found correlation coefficient of 0.67 for this relation.

Recently Ikejiri et al. (2011) presented a large set of optical data for both blazar types. The authors confirmed that blazars have a universal bluer-when-brighter trend in the optical band. 88% of the well observed blazars sample shows this behavior. There are few exceptions, mostly FSRQs, which show the redder-when-brighter trend, however when these objects are active, the bluer-when-brighter trend can be observed.

## 2.4 PKS 2155-304

PKS 2155-304 located at  $z = 0.116$  (Falomo et al. 1993), is classified as a high-frequency peaked BL Lac object (HBL). It is one of the brightest blazars in the southern sky and this has made it a goal for observations at different wavelengths for already more than 30 years. The source was discovered by the HEAO-1 X-ray satellite (Schwartz et al. 1979; Griffiths et al. 1979). As a particularly bright BL Lac type object, PKS 2155-304 has been analyzed also by several extensive optical/UV studies (Courvoisier et al. 1995; Pesce et al. 1997; Pian et al. 1997). These campaigns established the intraday variability nature of the source with the shortest flux doubling timescales of about 15 min, detected however in only a few isolated epochs (Paltani et al. 1997; Heidt et al. 1997). A comparison between optical/UV and X-ray temporal and spectral characteristics of PKS 2155-304 indicates that the peak of the synchrotron continuum is located around UV frequencies, only occasionally shifting to longer (optical) wavelengths (see Foschini et al. 2008). Also, the flux variability amplitudes at optical and UV frequencies are always significantly smaller than those observed at X-ray frequencies. In general, a variety of optical/UV–X-ray correlation patterns have been found in different epochs and datasets, though several authors noted that such correlations seem to be in general stronger and more pronounced on shorter variability timescales and during the enhanced activity epochs of the source: as the flux decreases and variability timescales get longer, the optical/UV–X-ray correlations become weaker, and at the same time the lags between flux changes at optical/UV and X-ray frequencies increase (see, e.g., Brinkmann et al. 1994; Urry et al. 1997; Zhang et al. 2006; Dominici et al. 2004; Osterman et al. 2007).

The blazar was also observed in high and very high energy  $\gamma$ -rays. The emission of PKS 2155-304 was discovered by EGRET (Vestrand et al. 1995) in the energy range from 30 MeV to 10 GeV, and by the University of Durham Mark 6 telescope above 300 GeV (Chadwick et al. 1999). The first H.E.S.S. detection of the source was made in July and October 2002 (Aharonian et al. 2005a). The first multiwavelength (MWL) campaign for this blazar organized by the H.E.S.S. Collaboration was conducted in 2003 (Aharonian et al. 2005b). The low state of the source was monitored simultaneously in X-rays by RXTE/PCA, in the optical range by ROTSE, at radio frequencies by Nançay Radio Telescope, and in VHE  $\gamma$ -rays by H.E.S.S. The observations do not show any clear relation between observed fluxes at different frequencies.

From 2004 till now PKS 2155-304 was frequently observed by the four H.E.S.S. telescopes. In 2006 an exceptional flare, the outburst with the flux 10 times the average flux was detected (Aharonian et al. 2007), with the flux doubling timescales in the VHE regime of the order of a few minutes. The MWL data collected around the time of the 2006 flare were presented and extensively discussed in Aharonian et al. (2009a) and Abramowski et al. (2012). These revealed a strong X-ray–VHE flux correlation at high flux levels, weak-

ening however at lower flux levels, and characterized in addition by much smaller X-ray flux changes (factor  $\sim 2$ ) than those observed in the VHE range. No optical–VHE correlations were found in the 2006 flaring data.

Detailed statistical analysis of all the VHE data collected for PKS 2155-304 by H.E.S.S. during the period 2005-2007 was presented in Abramowski et al. (2010). The results of the analysis revealed again the red-noise type of the flux changes albeit with relatively short characteristic variability timescales  $\lesssim 1$  day (in particular during the 2006 flaring period; see also Aharonian et al. 2007), the fractional rms correlated with the photon energy, and the excess rms correlated with the flux.

Between the 25th of August and the 6th of September 2008, PKS 2155-304 was observed simultaneously by H.E.S.S., *Fermi*-LAT, RXTE and ATOM (Aharonian et al. 2009b). The source was found again in the low state, with the average  $> 200$  GeV flux of about 15% of Crab. The performed ‘night-by-night comparison’ of the VHE and optical fluxes at that time (11 days of observations) indicated interestingly, for the very first time in the case of this source, indications of for a positive correlation (the Pearson’s correlation coefficient of 0.8 with uncertainties  $< 0.09$ ). In support of the observed trend, the performed broad-band SSC modeling confirmed that for the broadly expected parameters of the source characterizing its quiescence periods, these are indeed the electrons emitting synchrotron photons at optical frequencies which produce bulk of the observed  $\gamma$ -rays via the SSC process.

## VHE Gamma-ray Astronomy

The Earth's atmosphere is not transparent to electromagnetic radiation in several frequency ranges. Such radiation can be observed only by detectors mounted on satellites and balloons, but in the case of the most energetic photons via cascades of secondary particles, which can be registered on the Earth's surface. A schematic view of the transparency of the Earth's atmosphere is shown in Fig. 3.1. Radio waves, low energetic microwaves and visible light can be directly detected by telescopes on the ground. Infrared photons can be observed from above (e.g. from a plane, like SOFIA<sup>1</sup>). Hard UV light and X-rays can only be registered by detectors on board of satellites. At higher energies to directly observe gamma-rays one can use satellites, like the Fermi Gamma-ray Space Telescope<sup>2</sup>, but the most energetic photons generate showers of secondary particles in the atmosphere, and then ground telescopes can make indirect observations of them by registering Cherenkov light emitted by charges particles. Such a technique of observing gamma-rays is used by: MAGIC<sup>3</sup>, VERITAS<sup>4</sup> and H.E.S.S. experiments<sup>5</sup>. The details are described below.

### 3.1 Gamma Radiation

The cosmic  $\gamma$ -ray radiation extends over the wide range of the electromagnetic spectrum. Gamma-rays from space are mostly absorbed by the Earth's atmosphere and its direct detection is possible only by using balloons or satellites. But the most energetic gamma-rays (in 100 GeV/TeV range) are so rare that for their detection we would need a long time of observations and/or a large detector (e.g. a detector with an effective area of

---

<sup>1</sup>Stratospheric Observatory For Infrared Astronomy, <http://www.sofia.usra.edu/>

<sup>2</sup><http://fermi.gsfc.nasa.gov/>

<sup>3</sup><http://magic.mppmu.mpg.de>

<sup>4</sup><http://veritas.sao.arizona.edu>

<sup>5</sup><http://www.mpi-hd.mpg.de/hfm/HESS/>

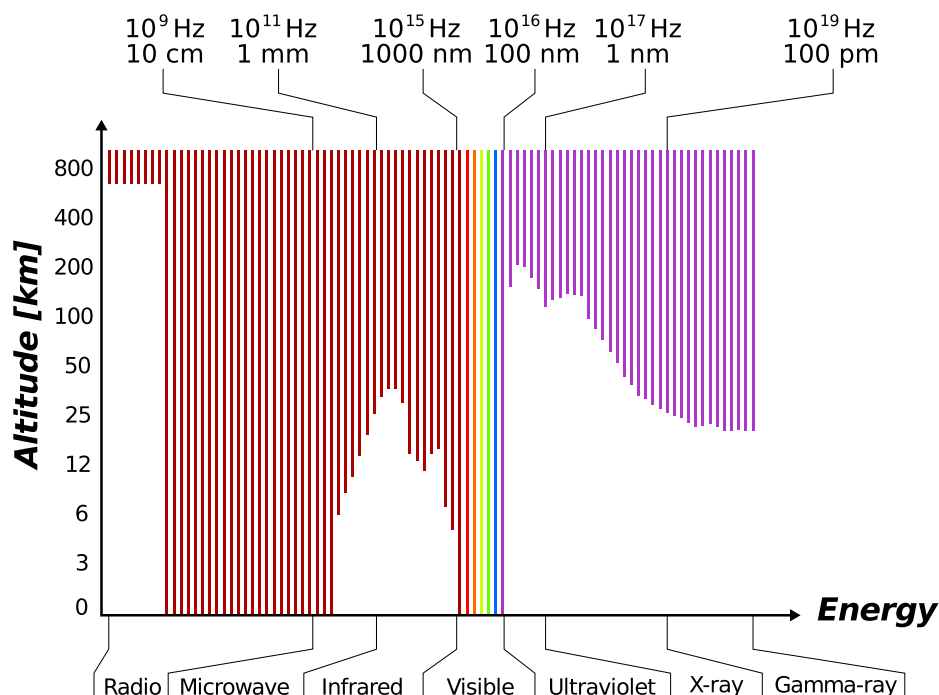


Figure 3.1: The transparency of the atmosphere.

1 m<sup>2</sup> would register 1 photon with the energy of 1 GeV per day and 1 photon with the energy of 1 TeV per year). Hence for the most energetic gamma-ray photons an indirect method of measurements is used, namely observations of Cherenkov light produced in the atmosphere by showers of secondary particles (see Sec. 3.2.3).

The gamma-ray photons are divided in astronomy into five energy ranges (Aharonian 2004): low (LE, below 30 MeV), high (HE, 30 MeV - 30 GeV), very high (VHE, 30 GeV - 30 TeV), ultra high energy (UHE, 30 TeV - 30 PeV) and extremely high energy (EHE, above 30 PeV)

## 3.2 Gamma-ray Initiated Air Showers

When a high energy  $\gamma$ -ray photon or a cosmic ray particle enters the Earth's atmosphere, it interacts with atmosphere's atoms and initiates a cascade of secondary particles. Two different scenarios can be considered with respect to the primary particle: (i) for photons, electrons or positrons the shower has an electromagnetic nature, (ii) for hadronic particles electromagnetic and hadronic sub-cascades are present in the shower.

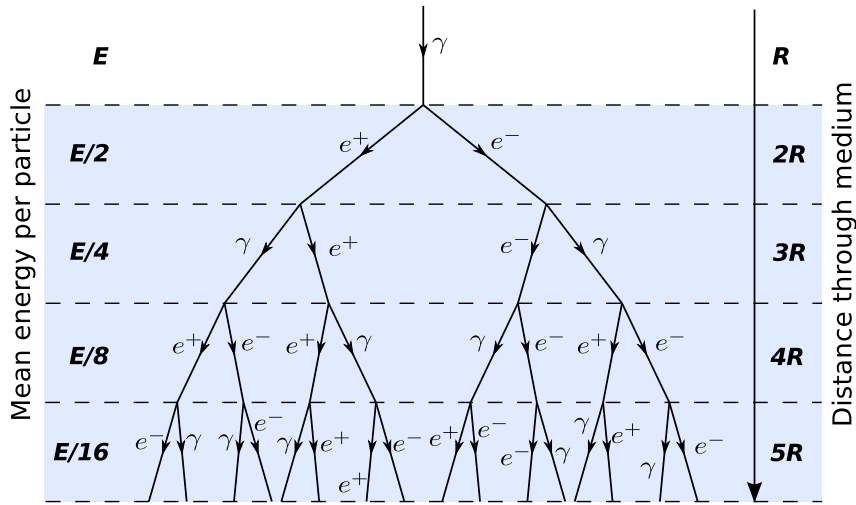


Figure 3.2: A simple model for an electromagnetic shower following Longair (2010).

### 3.2.1 Electromagnetic Cascade

A popular, simple model, which describes the basic properties of electromagnetic cascade, was proposed by Heitler (1954). It assumes: (i) radiation lengths of electrons and photon are the same; (ii) particles are created only via Bremsstrahlung and pair production processes; (iii) energy is shared equally by electrons, positrons and photons. The radiation length is a characteristic of a material related to the energy loss of high energy, electromagnetically-interacting particles with it.

A gamma-ray photon of energy  $E$  entering the atmosphere can produce  $e^+ e^-$  pair in the electric field of a nucleus. These electron and positron produce the next generation of photons in the Bremsstrahlung processes. Then, the photons produce a new electron-positron pair, and the creation process is repeated (Figure 3.2) till the energy per particle will be smaller than some *critical energy*  $E_c$  (about 80 MeV). Below  $E_c$ , the dominant loss process for the electrons is the ionization loss and this causes termination of any further development of the air shower. The final number of high energy photons and particles is proportional to the primary gamma-ray photon energy, roughly  $E/E_c$ , and the creation of particles is repeated along  $n_c = \log(E/E_c)/\log(2)$  radiation lengths (Longair 2010).

### 3.2.2 Hadronic Cascade

The other type of the particle cascades are the hadronic ones. A hadronic particle (e.g. proton) in a strong inelastic interaction, hitting a nucleus in the atmosphere, can produce secondary nucleons, mesons and hyperons. Then the particles can be scattered again and form hadronic sub-cascades. Charged and neutral mesons can initiate an electromagnetic sub-cascade via the decay into leptons and gammas. The electromagnetic part of the shower loses energy by the Bremsstrahlung, pair production or ionization by

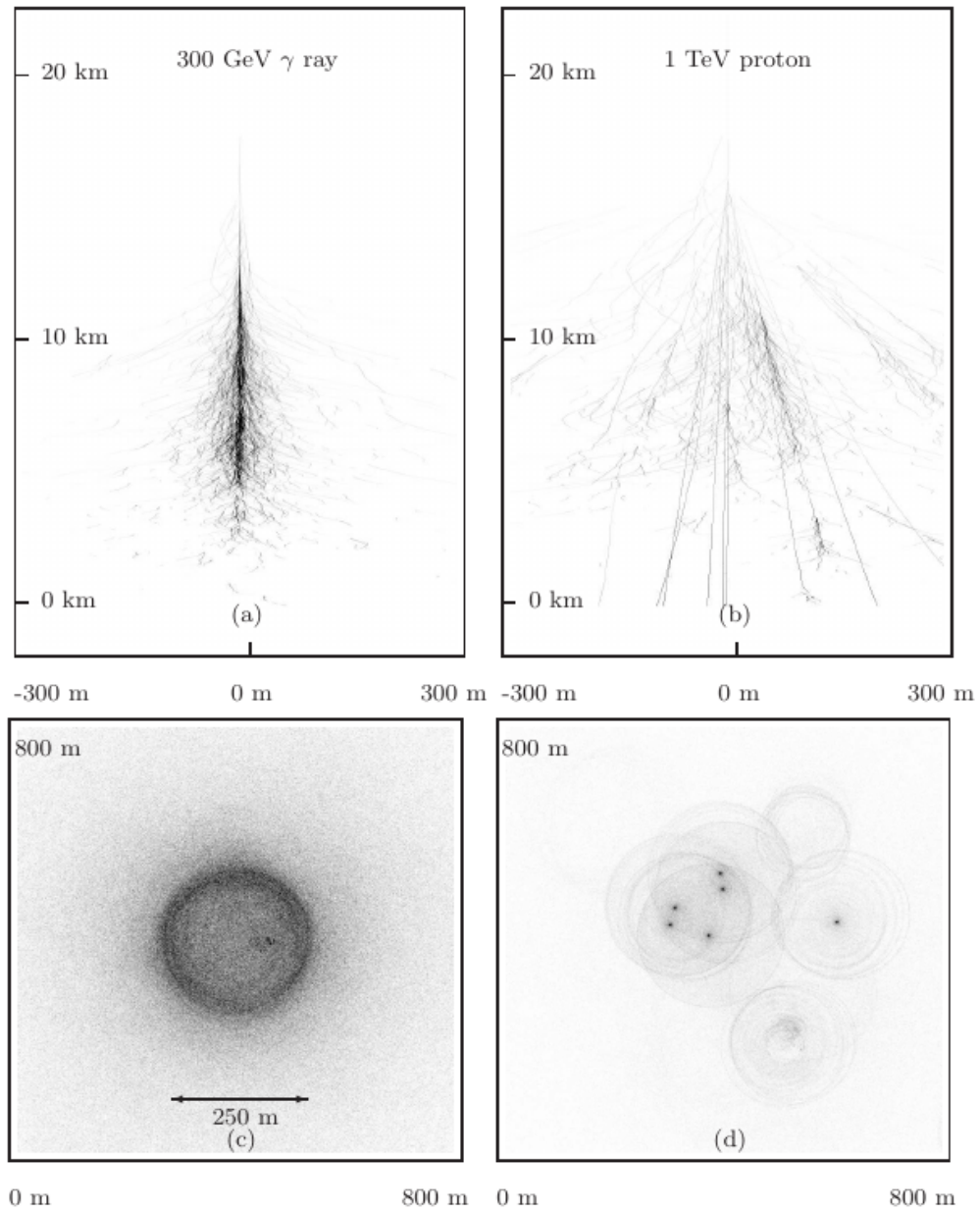


Figure 3.3: The comparison of the electromagnetic cascades initiated by a 300 GeV  $\gamma$ -ray and the hadronic shower induced by a 1 TeV proton modeled with Monte Carlo simulations. The upper panel depicts the vertical development of the shower, whereas the lower panel depicts the lateral shower development perpendicular to its axis. Courtesy of Konrad Bernlöhner.

the electrons, while the hadronic part loses its energy in the production of particles like muons and neutrinos.

### Differences Between Electromagnetic and Hadronic Cascade

- The interaction length for the hadronic shower is bigger than in the case of the electromagnetic ones:  $\sim 85 \text{ g cm}^{-2}$  and  $\sim 35 \text{ g cm}^{-2}$ , respectively.
- The electromagnetic shower is more regular in contrast to more complex hadronic cascade (see Figure 3.3).

### 3.2.3 Cherenkov Emission

When a charged particle is moving in a medium with velocity bigger than the light velocity in the medium, the Cherenkov light is emitted. The moving particle polarizes the medium which returns to the normal state after the particle passed by. If the particle moves faster than the light speed (in the medium), the polarization field is not symmetric along the direction of the moving particle. Then, the medium along the track of the moving particle will radiate short pulses of radiation, which can interfere. The Cherenkov light is emitted in a cone with the angle  $\Theta_C$ :

$$\cos(\Theta_C) = \frac{1}{\beta \cdot n}, \quad (3.1)$$

where  $n$  is the refraction index of the medium,  $\beta = \frac{v}{c}$ ,  $v$  is the velocity of the particle,  $c$  is the speed of light in the vacuum. The  $\Theta_C$  will grow with the increasing  $\beta$ , up to the maximum  $\Theta_{C,\max}$ :

$$\Theta_{C,\max} = \arccos \frac{1}{n} \quad (3.2)$$

This effect, known also as the Vavilov-Cherenkov phenomenon, was discovered by Cherenkov in 1934 during the investigation of the luminescence of uranyl salts under the incidence of gamma rays from radium. The scientist detected a new type of luminescence, which could not be explained by the theory of fluorescence. The observed radiation was generated in a short flash ( $\tau = 10^{-9} \text{ s}$ ). Further studies on the Cherenkov radiation have shown that:

- The radiation is observed at a specific angle with respect to incident particles.
- The intensity of the radiation is independent of the charge  $Z$  of the medium.
- In a magnetic field the polarization of the luminescence changes rapidly - the Cherenkov emission is caused by charged particles.

The phenomenon was theoretically explained by Frank and Tamm (for review see e.g. Nakamura & Particle Data Group 2010). The Frank-Tamm formula shows the number of photons produced per unit path length and per unit energy of a charged particle:

$$\frac{d^2N}{dE dx} = \frac{\alpha Z^2}{\hbar c} \sin^2 \theta_c = \frac{\alpha^2 Z^2}{r_e m_e c^2} \left(1 - \frac{1}{\beta^2 n^2(E)}\right) = \frac{2\pi\alpha Z^2}{\lambda^2} \left(1 - \frac{1}{\beta^2 n^2(\lambda)}\right), \quad (3.3)$$

where  $\alpha$  is the fine structure constant and  $Z$  the particle's charge. A peak of  $\frac{d^2N}{dE dx}$  distribution is located in the UV region, but strong absorption of this radiation in the atmosphere causes that a maximum number of Cherenkov photons registered on the surface is at about 330 nm.

The number of photons in the frequency interval  $\nu$  and  $\nu + d\nu$  emitted by a particle with charge  $Z$  moving with a velocity  $\beta$  in a medium is given by the formula (e.g. Nakamura & Particle Data Group 2010):

$$N(\nu)d\nu = 4\pi^2 \frac{(Zq)^2}{hc^2} \left(1 - \frac{1}{n^2\beta^2}\right) d\nu. \quad (3.4)$$

### 3.3 High Energy Stereoscopic System (H.E.S.S.)

The gamma-ray observatory H.E.S.S. (Fig. 3.4) is an array of imaging atmospheric Cherenkov telescopes located on the Khomas Highland of Namibia, at 1800 m above the sea level. The name H.E.S.S. honors Victor Hess, who discovered cosmic rays in 1912 and received the Nobel Prize in 1936 for the discovery. Observations are carried out using the Cherenkov technique described above. The first phase of the experiment carried with four telescopes is dedicated to observe Very High Energy (VHE)  $\gamma$ -rays in the energy range from approximately 100 GeV up to 10 TeV. Its construction began in 2002, when the first telescope was built. The full array of four telescopes (H.E.S.S. phase I) has been operational since 2004.

The choice of the experiment location was dictated by good observation conditions on site. This type of observations requires: moonless nights and the cloudless, clear, dark sky. The southern location provides also conditions for the observations of the Galactic Plane at low zenith angles. The H.E.S.S.I array consists of four identical telescopes, located in the corners of a square. The distance between the telescopes is 120 m. The spacing has been optimized for maximum sensitivity at the energy of 100 GeV. An angular resolution for reconstruction of the direction of an original gamma ray is better than  $0.1^\circ$  and an uncertainty of the reconstructed energy is approximately 15%. The system can detect a flux as low as  $2.0 \times 10^{-13}$  gamma-rays  $\text{cm}^{-2} \text{s}^{-1}$  with 25 h observations with a significance of 5 standard deviations.



Figure 3.4: A current view of the H.E.S.S.II array. Credits: H.E.S.S. main web page<sup>6</sup>.



Figure 3.5: Front view of a H.E.S.S. small telescope. Credits: Alicja Wiercholska.

### 3.3.1 Telescope construction

Each telescope consists of a heavy, support structure, a dish and camera. The telescopes are built on an altitude-azimuth mount (Figure 3.5). A total area of the mirror dish is  $107 \text{ m}^2$  and has a diameter of 13 m. The dish consists of 382, circular mirrors each of 60 cm in diameter. The mirrors can be aligned separately with high precision. The telescopes are controlled via a computer and it takes between one and three minutes to slew to an object in the sky.

The mirrors direct light to the camera, which is equipped with 960 photon detectors – pixels. They are 8-stage photomultiplier tubes (PMTs) operating at a gain of  $2 \times 10^5$ . To reduce the loss of light each PMT has a Winston cone, which gathers light from a larger area into a smaller entrance of the detector. The pixels are mounted into 16 element drawers in which two separate acquisition cards are installed. For each pixel 3 channels

<sup>6</sup><http://www.mpi-hd.mpg.de/hfm/HESS/pages/about/telescopes/>

Table 3.1: Characteristics of the H.E.S.S. telescopes.

	small telescope	large telescope
Height of elevation axis	10 m	24 m
Dish size	12.0 m; hexagonal	32.6 m by 24.3 m; equivalent to 28 m circular dish
Shape of reflector	Davies-Cotton	Parabolic
Total mirror area	108 m <sup>2</sup>	614 m <sup>2</sup>
Focal length	15 m	36 m
Camera photo sensors	960 1-1/4' photo multipliers	2048 1-1/4' photo multipliers
Camera packaging	60 drawers of 16 PMTs each	128 drawers of 16 PMTs each
Camera pixel size	42 mm (hexagonal, flat-to-flat), equivalent to 0.16 degree	42 mm (hexagonal, flat-to-flat), equivalent to 0.067 degree
Sensitive area / field of view	5.0 degree on the sky	3.2 degree on the sky
Power consumption	5 kW	8 kW
Dimensions of camera body	160 cm wide, 160 cm high, 150 cm deep	227 cm wide, 240 cm high, 184 cm deep
Weight of complete telescope (including mirrors, camera)	60 tons	580 tons

are read out: one triggering and two acquisition channels with high and low gain.

The triggering channel is used to gather information about a positive signal in individual PMTs to determine when the whole camera is to be read out. The camera is triggered when 3 to 5 pixels of a sector of  $8 \times 8$  pixels detect a coincident signal above a set threshold (usually 5 photo electrons). The coincidence time window is about 1.5 ns. Additionally the camera is connected to the central trigger system to allow for multi-telescope triggering. The telescopes are read out if two or more telescopes have sent the trigger signal to the central triggering unit.

### 3.3.2 H.E.S.S.II

On July 26th 2012, the fifth telescope started operation in Namibia, what begins the H.E.S.S.II phase. With 28-meter-sized mirror, it is the largest Cherenkov telescope ever built. The new telescope allows to observe targets with better sensitivity and it has four times more pixels per sky area compared to the smaller telescopes. The new H.E.S.S. telescope fulfills the gap in energy coverage between the old configuration and the Fermi-LAT for the astronomical sources in HE and VHE gamma rays. The main properties of the H.E.S.S. small telescopes and the large one are presented in the Table 3.1. The observations described in this dissertation were done only by the previous H.E.S.S. configuration (4 telescopes). The fifth telescope can work in two modes: hybrid (with small telescopes) and mono (separately).

### 3.3.3 H.E.S.S. data analysis

H.E.S.S. data are gathered in 28 minute-long runs during which the telescopes track a given astrophysical target or position in the sky. The collected observational data are selected on the basis of the standard quality criteria: weather conditions and the infor-

mation coming from the hardware, showing if one can reject runs when the system was not stable and the data may be corrupted. For the hardware the number of active pixels is taken into account. The pixels can be switched off because of malfunction, bright stars or meteors in the field of view. To assure no artifacts in the event reconstruction the telescopes which have more than 10% disabled pixels are not included into the analysis. Additionally, the data quality can be evaluated for the number of running telescopes and how the tracking or triggering system behave. Also, since the optical reflectivity of the mirrors degrades on a timescale of years one has to find proper correction factors. The estimation of the factors is done for each telescope using the registered muon images (see below).

### Calibration and Image Cleaning

Cherenkov photons are recorded using the PMTs and each of them is counted as a single pixel in the camera. The photoelectrons, produced by the photoelectric effect in the PMT, are registered using an analog-to-digital converter (ADC). The cameras need to be calibrated to properly derive the physical properties of the recorded signal. They are calibrated against the timing of the signal integration, the mean ADC counts without any signal, the flat-field to ensure the homogeneity of the efficiency of the camera, and the conversion factors of the ADC counts to photo electrons (p.e.).

Observations of Cherenkov photons are polluted mostly by the night sky background and starlight. Therefore a cleaning procedure is applied to every triggered event to reduce their influence on the data. The standard procedure assumes that all pixels which have more than 10 p.e. and whose one of the neighboring pixels have more than 5 p.e. are kept for further analysis. Also the pixels with more than 5 p.e. are kept if one of their neighbors have more than 10 p.e. All other pixels are excluded from the analysis.

### Event Reconstruction

A primary  $\gamma$ -ray photon can be described by its energy, direction and impact position in the ground, known as the core. The total Cherenkov photon intensity is proportional to the energy of the primary  $\gamma$ -ray photon. To reconstruct this energy from gamma-ray shower image, it is compared to simulations of showers performed by the CORSICA program (Heck et al. 2012). The comparison is done for images from each telescope and then the mean value of the energy is calculated. The final energy resolution is defined as the standard deviation of  $(E_{\text{reco}} - E_{\text{true}})/E_{\text{true}}$ , where the  $E_{\text{reco}}$  and  $E_{\text{true}}$  are the reconstructed and simulated energies, respectively. The accuracy of the energy reconstruction is  $\sim 15\%$  and it depends on observation conditions. For lower energies - near the energy threshold ( $\sim 100$  GeV) - the reconstructed energy is larger than the real one. For higher

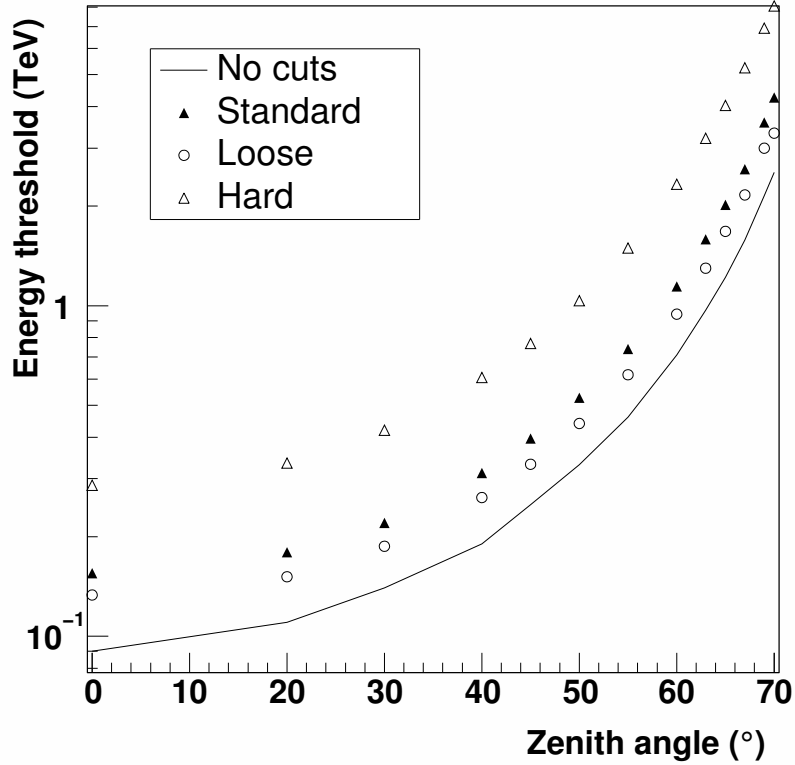


Figure 3.6: The safe threshold before and after selection cuts versus zenith angle, for three sets of selection cuts (Aharonian et al. 2006). The meaning of the *standard*, *loose* and *hard cuts* is explained later in this Chapter.

energies - above the energy threshold - the energy reconstruction accuracy is  $\sim 10\%$ . The safe energy threshold as a function of the zenith angle is presented in Fig. 3.6.

The stereoscopic technique allows to derive the core position from the relative orientation of shower images. Assuming that the core distance - defined as the distance from a telescope to the core - is non-zero, the image of a gamma-ray induced shower is elongated and reveals a roughly elliptical shape. The major axis of this ellipse points back to the core. Having such an image from another telescope we should find an intersection point at the position of the core. To quantify this more precisely the Hillas parameters (Hillas 1985) are introduced as shown in Figure 3.7. The distribution of intensity is characterized quantitatively by the first and second mathematical moments. The first moment is a mathematical equivalent of the center of gravity (COG) of the image. The elongated distribution is approximated as an ellipse of a given width and height described by the second moments matrix. The Hillas parameters are: the position of COG, the lengths of the main axes ( $\sigma_{\text{length}}$  and  $\sigma_{\text{width}}$ ), the orientation of the ellipse and the total number of p.e. in the image (*image size*).

In the case of observation with more than two telescopes the core position is calculated as an average of the intersection points from their shower images. Additionally one can introduce several weighting factors to this averaging to take into account the quality of shower images (e.g. see Hofmann et al. 1999). The direction of a gamma-ray photon, which has induced the shower, can be derived similarly to the core position. In this case the intersection point of major axes of shower images is found on the combined focal plane of different telescopes. The accuracy of the final core position and primary particle direction depends on many additional factors, such as the energy of the particle and the number of telescopes that have detected the shower. The typical accuracy of the shower direction determination is about  $0.1^\circ$  and  $\sim 20$  m for the reconstruction of the core position.

### Image Cuts

The so-called *size cuts* are used to reject events with too few photo electrons. If the number of p.e. is e.g. below 60 (in the case of standard cuts) the events are rejected or otherwise the errors of the reconstruction are very large. The *distance cuts* take into account that the acceptance drops towards the edge of the camera and therefore the images which have light distribution too far from the camera center are also rejected.

Gamma-ray observations with the Cherenkov technique are also polluted by Cherenkov light coming from hadron-induced air showers. Fortunately shower images induced by hadrons are much wider and clumpier, and therefore one can reduce its influence on the observations. To quantify the differences in shower images, following parameters are introduced:

$$l_{\text{scaled}} = \frac{l - \langle l \rangle}{\sigma_l} \quad \text{and} \quad w_{\text{scaled}} = \frac{w - \langle w \rangle}{\sigma_w},$$

where the  $l$  and  $w$  are the measured width and length of the light distribution in an image, and  $\sigma_i$  is the standard deviation of the distribution of value  $i$ . The  $\langle l \rangle$  and  $\langle w \rangle$  are the expected length and width values of the gamma-ray induced shower. These values are derived from the Monte Carlo simulation of gamma-ray induced images and calculated as a function of the image size and the impact parameter for a range of zenith angles. Since there are few telescopes the *mean reduced scaled length* and *width* are calculated by averaging over all contributing camera images. The distribution of these quantities is different in the case of hadron- and gamma-ray induced shower images (Figure 3.7).

The parameters of mean width and length with its standard deviation have been calculated using Monte Carlo simulations for 13 different zenith angles between  $0^\circ$  and  $70^\circ$  and stored as 2D lookup tables. The values for other zenith angles are linearly interpolated in cosine of zenith angle between the nearest simulated values. The cuts on the mean reduced scaled parameters, the size of the image and the core distance squared are

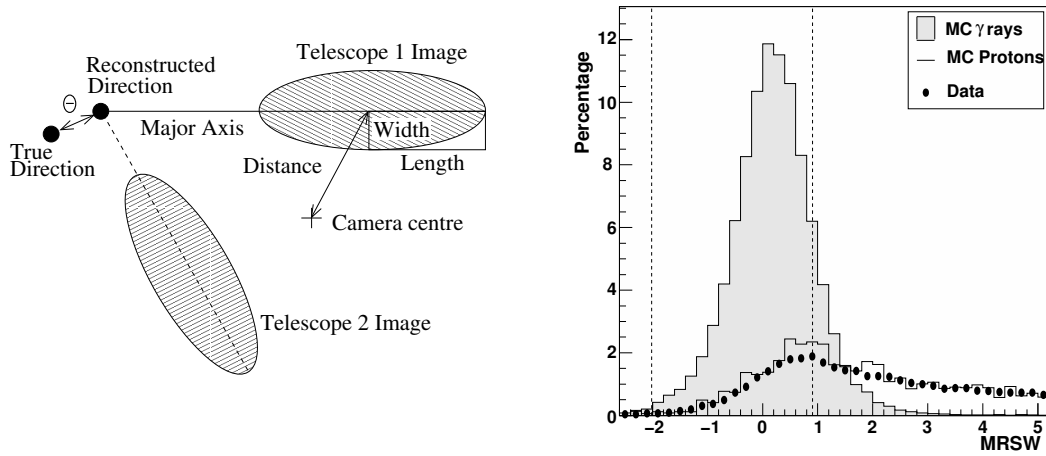


Figure 3.7: *Left panel:* a schematic view of the Hillas parameters; two images of a shower are shown. *Right panel:* distribution of MRSW from the Monte Carlo simulations of a gamma-ray and proton-induced shower and real OFF data. Both figures are taken from Aharonian et al. (2006).

optimized simultaneously using the simulated gamma-ray events and real background data to improve the detection significance derived by Li & Ma (1983). Three sets of cuts are used in the H.E.S.S. typical analysis:

- *hard* – includes events above 120 p.e., optimized for weak sources with 1% of the Crab nebula flux,
- *standard* – includes events above 60 p.e., optimized for sources with  $\sim 10\%$  flux of the Crab,
- *loose* – includes events above 40 p.e., optimized for strong sources with 100% flux of the Crab, which have also the largest acceptance for spectra.

### Muon correction

The system of mirrors, PMTs and other hardware gives decreasing response over time. Therefore to maintain the quality of the reconstruction it is needed to find the proper correction factors. One can use single muon images, because their Cherenkov light pattern can be theoretically predicted and compared with the real measurements, hence the respective correction factors can be derived.

### Background Estimation

Despite the cuts on the image parameters some of the hadron-induced showers are not rejected, because their images are very similar to those induced by gamma rays. To improve the measurements of the gamma-ray flux from a given source it is necessary to es-

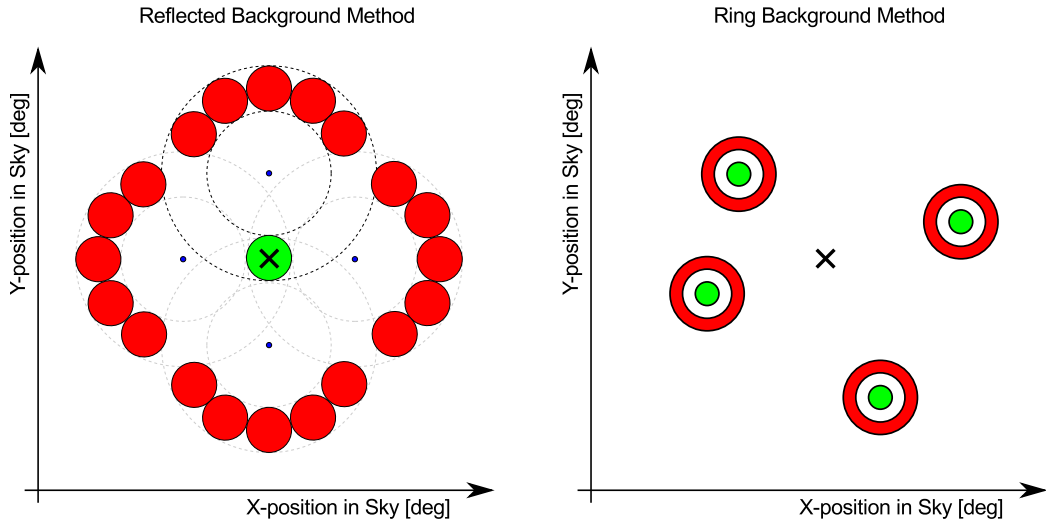


Figure 3.8: The applied methods of the background estimation. The green circles mark the source region (ON) and in the red regions the background is estimated (OFF). The cross marks the source position. In the *left panel* the blue dots show the four pointing positions with an offset from the source.

estimate the number of background events. For most of the background estimation methods used in the standard H.E.S.S. analysis the reconstructed events are filed into a sky map, a 2D distribution of the reconstructed directions of all gamma-ray-like events. The region around the source position of the radius of  $\theta_{\text{cut}}$  is called the ON region, and for this region the total number of events is calculated.

**Reflected Background Method** is used for runs taken in the wobble mode, in which the source is observed with an offset to the source position. The offset should be large enough to avoid the location of the new pointing position in the defined source region (ON). The background can be estimated in the FoV (Field of View) by using the regions of the radius of  $\theta_{\text{cut}}$  (same size as the source region) and distributed around the pointing position with the given radius of the offset (Fig. 3.8). The number of the regions depends on the offset, the size of the source region and the presence of other gamma-ray sources visible in the FoV. These regions, also called the OFF regions, have to be separated from each other and free of gamma-ray sources. The normalization between the ON and OFF counts is given only by the ratio of solid angles, and therefore this method is very simple and robust. However, the acceptance of the camera can depend not only on the radius from the pointing position and therefore the estimation of the background is done for a few other positions around the source. In this method the non-radial acceptance variations can be compensated. The normalization factors in the reflected background method do not depend on energy, so this method is used for flux and spectrum measurements.

**Ring Background Method.** In this method the background is estimated by calculating the background events in a ring around a given position. This can be done for every position in the FoV (Fig. 3.8). The inner and outer radii of the ring are chosen in such a way that the ratio of solid angles of the ring and the ON region is close to 7. The inner radius should be large enough to avoid contamination of the background by the misreconstructed gamma-rays. Regions with known gamma-ray sources are excluded from the ring. The normalization factor is given by the ratio of solid angles weighted according to the variation of camera acceptance on the ring. The acceptance may not be constant as a function of energy and therefore this method is not used for spectral observations.

### Spectrum and light curve measurements

To derive a spectrum data are logarithmically binned in energy. In further analysis only the bins for which the difference between the mean reconstructed energy and the simulated energy is less than 10% are used. This results in an energy threshold, the so-called *safe threshold*.

Gamma-ray flux measurements rely on the *effective area* of the system, which depends on the energy, offset, zenith angle and applied image cuts. The gamma-ray rate is given by the convolution of the flux  $F(E)$  with the effective area  $A_{\text{eff}}(E)$  (Berge 2006):

$$\frac{d^2}{dE_{\text{reco}} dt} N_{\gamma} = \int R(E_{\text{true}}, E_{\text{reco}}) A_{\text{eff}}(E_{\text{true}}) F(E_{\text{true}}) dE_{\text{true}}, \quad (3.5)$$

where  $R(E_{\text{true}}, E_{\text{reco}})$  is the response function. This function gives the probability that for an event with an energy  $E_{\text{true}}$  the reconstructed energy is  $E_{\text{reco}}$ . To find the spectrum  $F(E)$ , equation (3.5) needs to be deconvolved, which can not be easily done analytically. In the standard H.E.S.S. analysis it is assumed that the effective area can be determined for the reconstructed energy, and then the source flux is given by:

$$F(E_{\text{reco}}) = \frac{1}{A_{\text{eff}}(E_{\text{reco}})} \frac{d^2}{dE_{\text{reco}} dt} N_{\gamma}. \quad (3.6)$$

This assumption has a disadvantage that the effective area depends on the simulated spectrum used in its determination, but with the energy resolution of  $\sim 15\%$  this effect is small and can be neglected in most cases. The final formula for the flux in a bin  $i$  is then:

$$F_i = \frac{1}{(\Delta E)_i T_i} \left( \sum_{j=0}^{N_{\text{ON}}} \frac{1}{A_j} - \alpha \sum_{k=0}^{N_{\text{OFF}}} \frac{1}{A_k} \right), \quad (3.7)$$

where  $(\Delta E)_i$  is the width of the bin  $i$ , the  $T_i$  is the exposure time and  $\alpha$  is the normalization factor.  $N_{\text{ON}}$  and  $N_{\text{OFF}}$  are the number of events in ON and OFF regions, respectively.

In the case of weak sources or very short time intervals it might not be possible to derive the energy spectrum. However, the data can be still used to find an integral flux

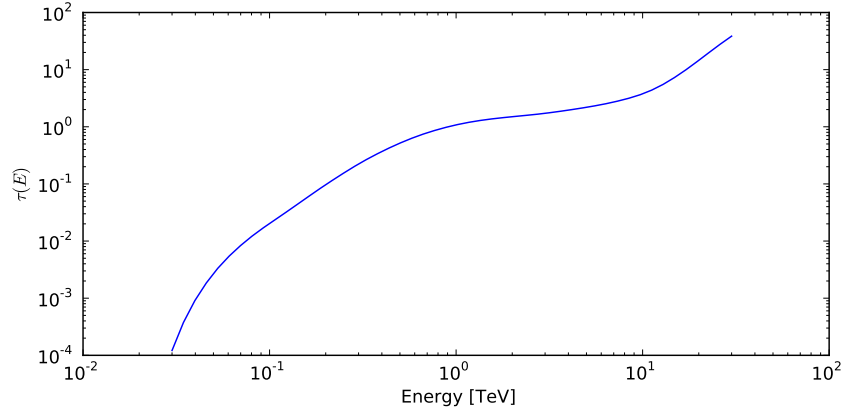


Figure 3.9: An optical depth of EBL as a function of energy for an object at redshift  $z = 0.116$ , e.g. PKS 2155-304 (Domínguez et al. 2011).

under the assumption that the gamma-ray energy spectrum is well approximated by a power-law with an index  $\Gamma$ . The normalization of this power law can be derived from comparing the total excess with the expected one.

### Extragalactic Background Light

Spectra of VHE emission need to be corrected against the photon-photon absorption of VHE gamma-rays on the Extragalactic Background Light (EBL) in the optical-to-infrared waveband. This absorption can be significant for extragalactic sources and needs to be taken into account in their spectral observations. Assuming that from an object at the redshift  $z$  the observed un-attenuated flux would be  $F_0(E)$  at a given energy  $E$ , the attenuated flux  $F$  is then:

$$F(E) = F_0(E)e^{-\tau(E,z)}, \quad (3.8)$$

where  $\tau$  is the optical depth found by integrating the density of the EBL along the line of sight. There have been many attempts to derive the spectral energy distribution of the EBL from observations. In the present work the most recent model from Domínguez et al. (2011) is used.

The optical depth dependence on energy makes VHE gamma-ray spectra steeper. The optical depth as a function of energy for the redshift of PKS 2155-304 ( $z = 0.116$ ) is shown in Figure 3.9.



Figure 3.10: The ATOM telescope. Credits: Alicja Wierzholska.

### 3.4 Automatic Telescope for Optical Monitoring

Automatic Telescope for Optical Monitoring (ATOM) (see Fig. 3.10) is an automatic, optical telescope located in Namibia, near the H.E.S.S. telescopes. The main mirror of the telescope has a diameter of 75 cm and the focal length of the optical system is 600 cm (Hauser et al. 2004). The location of the instrument at the same site allows running simultaneous observations to the H.E.S.S. ones in the same weather and atmospheric conditions as well as in the same observation window at night. Such multiwavelength observations are essential for our understanding of physical processes in blazars. The main scientific goals for this instrument are:

- optical monitoring of variable gamma-ray sources and potential H.E.S.S. targets,
- an atmospheric transmission monitoring to help calibrate the Cherenkov shower image analysis.

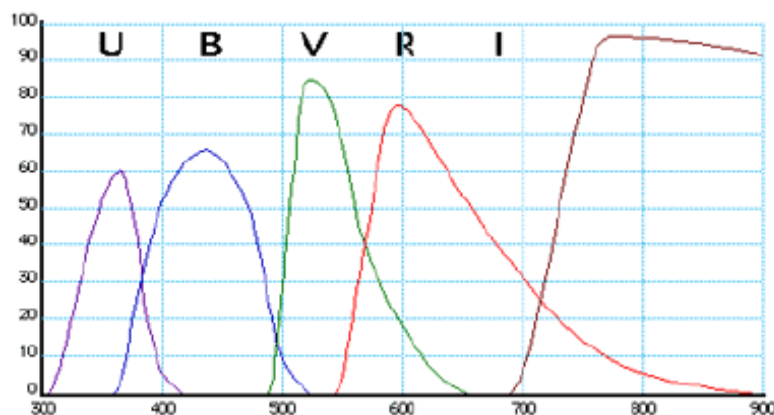


Figure 3.11: The ATOM’s transmission filter curves from “*ATOM user manual*”.

ATOM was originally built by Zeiss as a prototype for a computer controlled azimuthal telescope and it was operated for several decades in Germany in many astronomical projects. Then, in November 2006 it was shipped to Namibia where it has been used since. It conducts observations in five filters: *U*, *B*, *V*, *R* and *I* in the Johnson-Cousins UBVRI broad-band photometric system (Bessell 1990). The transmission curves of the filters are presented in Figure 3.11. To allow observations in the whole optical band, in 2008 the *U* band filter was removed.

The main CCD camera of the ATOM telescope with nominal resolution of  $1024 \times 1024$  pixels is placed at the Cassegrain focus of the instrument. The camera is equipped with a thermoelectric cooling. The camera control and data transfer are done via a standard Ethernet connection.

# Optical observations of blazars

## 4.1 Analyzed objects

The analyzed blazar sample includes 30 blazars of the BL Lac type frequently monitored by the ATOM optical telescope, observed simultaneously in two filters:  $B$  and  $R$ , for at least 20 nights, not necessarily night by night. Here, simultaneous gamma-optical observations are these performed during the same night. In the case when more than one observation was obtained during a night, the average value of the obtained data is used. From 30 of analyzed blazars up to now 21 have been detected as TeV sources<sup>1</sup>. The main properties of the analyzed objects can be found in Table 4.1. The sources were monitored during their visibility periods in 2007-2012, excluding the nights with bad weather conditions. The exact dates (months) of the observations are collected in Table 4.2.

The integration times for the observations are between 100 s and 1000 s for a single observation. The photometric flux scale was calibrated using the reference stars and the uncertainty of each single data point does not exceed 0.1 mag. In addition to the standard automatic analysis of the collected data, the raw images were also checked manually, and bad points (e.g. due to bad weather or exposed by the moon light) were rejected from the final dataset. The rejection does not affect the final results (the difference in Pearson's correlation coefficient, comparing two data set, before and after rejections, is smaller than 0.01). The observed magnitudes were corrected against the Galactic extinction based on the model by Schlafly & Finkbeiner (2011) using the NED's (NASA/IPAC Extragalactic Database) Extinction Calculator ( $A_B$  and  $A_R$  are shown in Table 4.1).

The  $B - R$  color is calculated for observations taken in  $B$  and  $R$  band during the same night. The errors are estimated by the root mean square. A linear fit to data points was receiving using the least squares method (Bevington & Robinson 2003). The computa-

---

<sup>1</sup>Based on the online catalog for TeV Astronomy TeVCat (<http://tevcat.uchicago.edu>), provided by Scott Wakely and Deirdre Horan.

tions and fitting are done by self developed scripts written in Python using the NumPy and SciPy modules (Oliphant 2007), and the visualization part by the Matplotlib library (Hunter 2007).

## 4.2 Color-magnitude diagrams and variability

Figures 4.1-4.16 show the  $B - R$  color index as a function of the  $R$  magnitude for the blazars from the sample and all the details of the observations for all 30 sources are given in Table 4.1. The color coding used in the color-magnitude plots represents the time evolution and is explained in Appendix A. To quantify the relation between the optical color and magnitude for all of the 30 objects Pearson's correlation coefficient (Bevington & Robinson 2003) is calculated and its uncertainty is estimated using a Monte Carlo method (see Appendix B). The linear fit to the  $B - R$  vs.  $R$  data is applied and the slopes of the regression fits are gathered in the same table. To quantify the global properties of the objects the average  $B - R$  color is calculated. To find how the  $B - R$  values translate into the spectral indices see Appendix C.

### SHBL J001355.9-18540

The blazar was observed by ATOM during 138 nights. The brightness of this source changes within 0.3 mag range. The color-magnitude diagram for the object (Fig. 4.1) does not show general color-magnitude relation. Also, it is difficult to distinguish periods (substructures in the color-magnitude plot) of following observations during which such a relation would be noticeable. The distribution of points in the color-magnitude diagram for the blazar looks very random.

### PKS 0048-097

The blazar was monitored during 96 nights in the 2009-2012 period. The brightness of this source changes within 2.8 mag range. The color-magnitude diagram show (Fig. 4.2) only a weak bluer-when-brighter relation. The detailed studies of the color-magnitude diagram for the blazar allow one to distinguish substructures with the bluer-when-brighter correlation. Such a relation is also visible during the outburst observed for this source. A lack of color-magnitude relation for PKS 0048-097 was suggested by Ikejiri et al. (2011).

### RGB J0152+017

The blazar was monitored during 269 nights in the 2007-2012 period. The brightness of this source changes within 0.3 mag range. The color-magnitude diagram (Fig. 4.2) shows a very clear bluer-when-brighter correlation for this blazar. The analysis of shorter periods of observations shows a strong bluer-when-brighter relation. However in the case

Table 4.1: A list of blazars.

Object (1)	RA h m s (2)	DEC ° ' '' (3)	Type (4)	$C_{(B-R,R)}$ (5)	a (6)	$\langle B-R \rangle$ [mag] (7)	$A_B$ [mag] (8)	$A_R$ [mag] (9)
SHBL J001355.9-18540	00 13 55	-18 54 06	HBL	0.08 ± 0.07	0.12 ± 0.13	1.64 ± 0.06	0.054	0.090
PKS 0048-097	00 50 41	-09 29 04	LBL	0.31 ± 0.06	0.041 ± 0.013	1.07 ± 0.07	0.070	0.117
RGB J0152+017	01 52 39	+01 47 17	HBL	0.88 ± 0.04	0.92 ± 0.03	0.98 ± 0.08	0.071	0.118
1ES 0229+200	02 32 48	+20 17 17	HBL	0.44 ± 0.07	0.84 ± 0.13	1.69 ± 0.06	0.292	0.489
AO 0235+16	02 38 38	+16 36 59	LBL	0.052 ± 0.048	0.004 ± 0.001	1.0 ± 0.1	0.172	0.287
PKS 0301-243	03 03 26	-24 07 11	HBL	0.26 ± 0.04	0.045 ± 0.013	0.28 ± 0.03	0.048	0.080
SHBL J032541.0-164618	03 25 41	-09 15 23	HBL	0.88 ± 0.09	0.26 ± 0.02	0.08 ± 0.09	0.083	0.139
1ES 0323+022	03 26 13	+02 25 14	HBL	0.77 ± 0.09	0.53 ± 0.07	0.17 ± 0.07	0.244	0.407
1ES 0347-121	03 49 22	-11 59 26	HBL	0.92 ± 0.05	0.88 ± 0.03	1.19 ± 0.15	0.102	0.170
1ES 0414+00.9	04 16 52	+01 05 23	HBL	0.309 ± 0.308	0.092 ± 0.017	0.24 ± 0.04	0.257	0.430
PKS 0447-439	04 49 24	-43 50 08	HBL	0.51 ± 0.06	0.10 ± 0.02	0.73 ± 0.04	0.031	0.051
PKS 0537-441	05 38 50	-44 05 08	LBL	0.11 ± 0.02	0.0074 ± 0.0056	0.93 ± 0.05	0.082	0.137
PKS 0548-322	05 50 40	-32 16 17	HBL	0.21 ± 0.07	0.29 ± 0.11	1.37 ± 0.03	0.076	0.128
PKS 0735+178	07 38 07	+17 42 19	LBL	0.26 ± 0.05	0.047 ± 0.017	0.49 ± 0.05	0.076	0.128
OJ 287	08 54 49	+20 06 30	LBL	0.05 ± 0.02	0.009 ± 0.014	0.96 ± 0.08	0.062	0.103
SHBL J101015.9-311908	10 10 16	-31 19 09	HBL	0.84 ± 0.12	0.72 ± 0.07	0.81 ± 0.08	0.184	0.307
1ES 1101-232	11 03 37	-23 29 30	HBL	0.47 ± 0.05	0.33 ± 0.04	1.02 ± 0.05	0.128	0.214
Mrk 421	11 04 27	+38 12 31	HBL	0.73 ± 0.05	0.18 ± 0.03	0.69 ± 0.04	0.033	0.055
1ES 1218+304	12 21 21	+30 10 36	HBL	0.92 ± 0.13	0.21 ± 0.02	0.41 ± 0.06	0.045	0.076
W Comae	12 21 31	+28 13 58	IBL	0.86 ± 0.06	0.163 ± 0.014	1.02 ± 0.07	0.049	0.082
1ES 1312-423	13 15 03	-42 36 50	HBL	0.87 ± 0.07	1.40 ± 0.07	1.02 ± 0.12	0.229	0.382
PKS 1424+240	14 27 00	+23 48 00	IBL	-0.26 ± 0.05	-0.062 ± 0.025	1.23 ± 0.03	0.127	0.212
AP Lib	15 17 41	-24 22 19	LBL	0.79 ± 0.06	0.42 ± 0.031	1.02 ± 0.06	0.299	0.500
PG 1553+113	15 55 43	+11 11 24	HBL	-0.19 ± 0.02	-0.027 ± 0.008	0.71 ± 0.03	0.113	0.189
Mrk 501	16 53 52	+39 45 36	HBL	0.56 ± 0.06	0.55 ± 0.09	1.23 ± 0.03	0.042	0.070
RGB J1725+118	17 25 04	+11 52 14	IBL	0.26 ± 0.07	0.044 ± 0.020	0.46 ± 0.04	0.372	0.621
PKS 2005-489	20 09 25	-48 49 53	HBL	0.76 ± 0.01	0.111 ± 0.004	1.36 ± 0.04	0.121	0.203
SHBL J213135.4-091523	21 31 35	-09 15 23	HBL	0.35 ± 0.09	0.096 ± 0.029	-0.005 ± 0.037	0.083	0.139
PKS 2155-304	21 58 52	-30 13 32	HBL	0.296 ± 0.007	0.023 ± 0.003	0.67 ± 0.04	0.047	0.078
BL Lacertae	22 02 43	+42 16 39	IBL	0.69 ± 0.04	0.088 ± 0.011	1.18 ± 0.05	0.714	1.193

(1) Object; (2) Right Ascension; (3) Declination; (4) Blazar type; (5) Correlation coefficient of the  $(B-R)$  vs.  $R$  relation; (6) Fitted slope of the correlation; (7) Average value of  $B-R$ ; (8), (9)  $A_B, A_R$  - Galactic extinction in the corresponding optical bands  $B$  and  $R$ ;

of selected part of observations, the source is redder-when-brighter. It is worth mentioning that the part in the color-magnitude plot with the redder-when-brighter relation includes observations when the magnitude was almost constant.

#### **1ES 0229+200**

The source was observed during 184 nights in the 2007-2012 period. The observed magnitude level is almost the same in each year, including only small variations of  $\sim 0.2$  mag. The linear fit to the color-magnitude diagram (Fig. 4.3) does not indicate a clear bluer-when-brighter relation. Also the analysis of shorter periods of observation (e.g. in one year observations) does not show such a relation.

#### **AO 0235+16**

The source was observed during 77 nights in 2007-2010. During this monitoring the brightness of the blazar changes in a wide range of 4.5 mag. For all observations of AO 0235+16 presented here (Fig. 4.3) there is no clear relation between the color and the magnitude. The first part of the color-magnitude diagram suggests the redder-when-brighter relation. Then the amplitude of the brightness variation is about 3 mag and the trend in the plot rather suggests the bluer-when-brighter correlation.

The source was included in the blazar sample analyzed by Ikejiri et al. (2011) and the authors found a very significant correlation between color and optical magnitude. In the earlier work (Raiteri et al. 2001) a similar color-magnitude relation was found for the faint state of the blazar.

#### **PKS 0301-243**

The source was frequently monitored by ATOM and here the presented observations were collected during 145 nights. The brightness of this source changes within 1.2 mag range. No significant color-magnitude relation apparent in the whole period of the observations, but the color-magnitude diagram (Fig. 4.4) for this object shows several sub-structures. For these shorter selected time intervals, a strong bluer-when-brighter correlations can be noticed.

#### **SHBL J032541.0-164618**

38 nights of observation of the source, collected in 2007-2011, show very clear evidence for color-magnitude correlations (Fig. 4.4). The amplitude of brightness for this set of data changes is about 1.2 mag.

**1ES 0323+022**

As in the case of SHBL J032541.0-164618, for 1ES 0323+022 the bluer-when-brighter relation is very clear (Fig. 4.5). The presented observations were collected during 40 nights the 2008-2012 period and the blazar was observed in each of these year. The brightness of this source changes within 0.3 mag range. The blazar was also one of the objects monitored by Ikejiri et al. (2011) and the authors also found a strong color-magnitude correlation.

**1ES 0347-121**

Similarly, as in the previous object, 1ES 0347-121 is a blazar with a clearly detected bluer-when-brighter chromatism (Fig. 4.5). The source was monitored during 161 nights in the 2007-2012 period. During the whole period of observations the brightness in the  $R$  band changes with the  $\sim 0.7$  mag amplitude. The time evolution shows that at the beginning of monitoring the source was bright, then the brightness was decreasing for next three years. Since then the magnitude has been constant, with only one short outburst. The maximal outburst, observed during the presented monitoring, was of about 0.5 mag.

**1ES 0414+00.9**

The blazar was monitored during 285 nights in 2007-2012. During the whole period of observations the brightness in the  $R$  band changes with the  $\sim 0.7$  mag amplitude. The best linear fit to the collected data does not indicate the bluer-when-brighter correlation for the object, but in the diagram two well separated structures can be distinguished (Fig. 4.6). The separation for these separate substructures is almost 0.1 mag. The first substructure (on the left) includes observations with the  $R$  band magnitude of about 16.7-16.4, the second (on the right) includes the observations with  $R$  magnitude of 16.3-15.9. The analysis of the time evolution shows that the points on the left side of the graph are from the observations earlier than these in the structure on the right hand side. The detailed studies of the substructures show, that it is possible to distinguish series of observations, for which the bluer-when-brighter is visible. The analysis of shorter intervals of observations does not show a clear relation between color and magnitude. In the light curve of the blazar single flares are visible in each year.

**PKS 0447-439**

The blazar was observed during 54 nights in 2009-2012. The brightness of the blazar changes of 0.8 mag in amplitude (Fig. 4.6). Observations of PKS 0447-439 suggest a relation between optical color and magnitude, but the calculated value of the correlation coefficient is not large enough to consider it very significant. There are no visible sub-

structures in the color-magnitude diagram, where the bluer-when-brighter or redder-when-brighter relation could be observed.

#### **PKS 0537-441**

The blazar was observed during 160 nights in 2008-2012. The brightness of the blazar changes of 2.4 mag in amplitude (Fig. 4.7). PKS 0537-441 is an example of a source for which the analysis of long-term data does not indicate clear color-magnitude chromatism. The color-magnitude diagram for this blazar seems to be composed of two parts, with each part having a different slope. The earlier observations have the redder-when-brighter character, while in the recent ones a significant the bluer-when brighter relation.

#### **PKS 0548-322**

Monitoring of this blazar includes 132 nights, during 2007-2012. In the color-magnitude diagram (Fig. 4.7) the distribution of points is random. The magnitude of PKS 0548-322 is almost constant. No significant color-magnitude relation is observed for this source, neither in the case of all observations considered together, nor for shorter intervals.

#### **PKS 0735+178**

The blazar was monitored by ATOM during 104 nights in 2008-2012. The brightness of the source changes of 1.2 mag in amplitude (Fig. 4.8). A weak bluer-when-brighter relation for PKS 0735+178 was reported by Gu et al. (2006), but in the case of observations presented here such trend is not visible. This trend is not either visible in short periods of observations.

#### **OJ 287**

OJ 287 is frequently monitored in the optical band by many instruments, including the ATOM telescope. Presented here monitoring includes 148 nights of observation collected in 2007-2012. The brightness of the blazar changes of 2.0 mag in amplitude (Fig. 4.8). This long-term optical monitoring with ATOM does not confirm a general relation for the whole data set. Color-magnitude correlation is observed only in short intervals of observations. A number of observations, presented in literature, indicate the bluer-when-brighter relation for this blazar (Carini et al. 1992; Gu et al. 2006; Dai et al. 2011; Ikejiri et al. 2011). These authors analysed short intervals of observations, thus their results are consistent with the ones obtained with ATOM.

**SHBL J101015.9-311908**

The source was monitored in 2008-2012 during 45 nights and the observations show a strong color-magnitude correlation (Fig. 4.9). The light curve shows brightness changes of amplitude up to  $\sim 0.3 - 0.6$  mag in  $R$  and  $B$  band.

**IES 1101-232**

The source was observed during 197 nights during 2007-2012. During the observation period, the brightness of the source was changing in a narrow range ( $\sim 0.4$  mag). Indication for the bluer-when-brighter trend is seen for this object (Fig. 4.9).

**Markarian 421**

The object was observed in different periods between 2007 and 2010 during 42 nights. In the presented observations the brightness changes by  $\sim 0.6$  mag. ATOM observations suggest bluer-when-brighter correlation in the case of Mrk 421 (Fig. 4.10). The blazar was also studied by Ikejiri et al. (2011) who also found the bluer-when-brighter relation for the source.

**IES 1218+304**

The object was monitored during 20 nights in 2009-2011. The brightness of the blazar changes of 1.0 mag in amplitude. The statistics is rather poor, but it is clearly visible that data points are concentrated in three substructures (Fig. 4.10). Each of the substructures fits to a significant bluer-when-brighter relation.

**W Comae**

W Comae is a source for which the bluer-when-brighter relation is clearly visible in 50 nights of observations, collected in 2008-2012 (Fig. 4.11). The statistics of observations is rather poor, the source was monitored in different periods during analyzed periods of observations. The light curve shows brightness changes with the amplitude of  $\sim 1.3$  mag.

**IES 1312-423**

The observations of this source were carried out at 122 nights during 4 years (2008-2011). The brightness of the blazar changes of 0.3 mag in amplitude (Fig. 4.11). The collected observations suggest the bluer-when-brighter relation for the object.

**PKS 1424+240**

During 94 nights of observations of PKS 1424+240, collected in 2009-2012, the correlation coefficient for color-magnitude relation is negative and suggests that the source

tends to be redder-when-brighter (Fig. 4.12). The analysis of shorter intervals allows one to indicate periods, when it shows bluer-when-brighter properties. The character of color-magnitude relations for PKS 1424+240 was changing significantly in time and the general trend is generated by substructures. The amplitude of brightness changes in the light curve is  $\sim 0.5$  mag.

#### **AP Librae**

The sampling of three years results (2010-2012) in 112 nights of observations. The source shows a significant bluer-when-brighter correlation (Fig. 4.12). The brightness of the blazar changes of 0.5 mag in amplitude. The color-magnitude diagram shows that the bluer-when-brighter relation is observed not only globally in a three-year-long monitoring but also in the cases of selected shorter intervals e.g. in different years of observations. In the light curves for each year separate flares can be identified.

#### **PG 1553+113**

The blazar was frequently monitored during 2007-2012 (294 nights). The brightness of the blazar changes of 1.0 mag in amplitude. The color-magnitude diagram for this source do not show general correlation (Fig. 4.13). In the plot it is possible to distinguish periods when the source was significantly redder-when-brighter and also these, when the blazar is bluer-when-brighter. The blazar was also analyzed by Ikejiri et al. (2011), where also no consistent relation between the optical color and magnitude was found.

#### **Markarian 501**

The observations of this source were carried out at 79 nights during 6 years (2007-2012). For this source the observed magnitude is almost constant, including small variations of  $\sim 0.2$  mag (Fig 4.13). The color-magnitude relation for Markarian 501 was studied by Ikejiri et al. (2011). The authors show that the blazar becomes bluer when it is brighter. Also, observations collected with ATOM confirm such a relation.

#### **RGB J1725+118**

The monitoring of the source includes 69 nights, collected in 2008-2012. The light curve shows brightness changes by  $\sim 0.8$  mag (Fig. 4.14). The analyzed observations do not show color-magnitude relation for this source. The analysis of short periods of observations also does not suggest neither the bluer-when-brighter not the redder-when-brighter chromatism in this object.

**PKS 2005-489**

The object is frequently monitored by ATOM and here the observations collected during 697 nights are presented. The light curve shows amplitude of the brightness changes of  $\sim 1.3$  mag. In presented data, collected in 2007-2012, there is a significant correlation between the observed  $B - R$  color and magnitude in the  $R$  band (Fig. 4.14). The general trend apparent in the plot is a sum of different observations, during which the bluer-when-brighter relation is observed.

**SHBL J213135.4-091523**

The blazar was monitored by ATOM during 81 nights in 2008-2012. The light curve shows brightness changes by  $\sim 0.6$  mag (Fig. 4.15). The collected observations do not show any indication either for the bluer-when-brighter relation, or for redder-when-brighter one.

**PKS 2155-304**

The blazar was monitored by ATOM during 792 nights in 2007-2012. The light curve shows brightness changes by 2.0 mag (Fig. 4.16). The structure of the color-magnitude diagram for observations from 2007-2009 is presented in Abramowski et al. (HESS Collaboration) (in prep.), in which two separate branches are visible. In current work the analysis extends the observational sample to a larger data set from 2007 up to 2012. Altogether there were 792 nights of observations. Still, in the color-magnitude diagram, the two separate branches can be identified. The observations from 2010-2012, which were not presented in Abramowski et al. (HESS Collaboration) (in prep.) are adding up to the “upper branch” in the graph. For each of separate branches the color-magnitude correlation is significant, while the relation does not occur for the whole data set. The transition between “upper” and “lower” branch occurs at RJD 54385. The light curve shows brightness changes by  $\sim 2$  mag and in each year separate flares (outbursts) can be identified. A deep multiwavelength study of PKS 2155-304 is presented in Chapter 5. PKS 2155-304 is one of the sources described by Ikejiri et al. (2011) for which color-magnitude relation was not detected.

**BL Lacertae**

The source was monitored during 65 nights in 2008-2009. The light curve shows brightness changes by 1.5 mag (Fig. 4.15). In the case of BL Lacertae there is a clear positive correlation between optical color and magnitude. Such a relation for this blazar was reported earlier, see e.g. Villata et al. (2002, 2004). A clear bluer-when-brighter trend was also indicated by observations presented by Ikejiri et al. (2011).

Table 4.2: A list of observations within the long-term monitoring of blazars analyzed in this study.

Object	2007	2008	2009	2010	2011	2012
SHBL J001355.9-18540		11, 12	5-12	8-12	6-12	5-12
PKS 0048-097			8-12	1, 7-12	6-12	5-8, 10
RGB J0152+017	11, 12	1, 6-12	1, 6-12	1, 2, 6-12	1, 6-12	1, 2, 6-10
1ES 0229+200	8-12	1, 8-12	1, 8-12	8-11	7-11	7-10
AO 0235+16	1, 9-11	7, 9-12	1, 7, 8	8		
PKS 0301-243			8-12	2, 3, 6-12	7-12	2, 7-12
SHBL J032541.0-164618		9-12	1, 7-10, 12	3, 7, 8	7, 9, 10, 12	1, 7
1ES 0323+022		10-12	1, 7-10, 12	2, 9-12	9-11	1, 7-10
1ES 0347-121	8-12	1, 8-12	1, 3, 7-12	3, 7, 8-11	1, 7-11	1, 2, 10
1ES 0414+00.9	1, 2, 8-12	1, 8-12	1, 3, 7-12	2, 8-12	1, 3, 7-11	10
PKS 0447-439			8, 12	1-4, 9-12	1, 4, 8-11	1-4, 8, 10
PKS 0537-441		10-12	1, 3-9	1-5, 9-12	1, 9-11	1-4, 8-10
PKS 0548-322	5, 9-12	1, 10-12	1, 3-5, 7-12	2-5, 9-12	1, 2, 4, 5, 9-11	1-5, 9, 10
PKS 0735+178		1, 9-12	1, 2-5, 9-12	1, 2-5, 10-12	1, 2, 4, 5, 9-11	1, 3-5
OJ 287	2, 5, 11, 12	1, 5, 6, 10-12	1, 2-6, 10-12	3-6, 11, 12	1, 3-6, 11	2, 4, 5, 11, 12
SHBL J101015.9-311908	1	5, 6, 11, 12	2-7	4-7	1, 3, 4, 6, 7	
1ES 1101-232	2, 6, 7, 11, 12	1, 5-7, 11, 12	1, 3-7, 11	1, 2-7, 12	1, 4-6	3-5, 7
Mrk 421	5	1, 6, 7, 12	1, 3-6	2		
1ES 1218+304			4-6	2, 3-7	3-6	2-8
W Comae		6, 7	1, 3-6	2, 4-7	4-6	3-5
1ES 1312-423		9, 12	1, 3-8	2-7	1, 2, 4-8	
PKS 1424+240			6-8	2-8	4-8	3-5
AP Lib				6-8	3-9	2-9
PG 1553+113	8, 9	8, 9	2-9	1, 2-9	4-9	3, 4-9
Mrk 501	5, 7, 8	5-7	3-7, 8	6, 7, 9	4, 5	3, 9
RGB J1725+118		10	3-9	6-9	5-9	3-9
PKS 2005-489	5-12	6-12	3-12	3-12	5-11	3-10
SHBL J213135.4-091523		7, 9, 10	3-10	4-8, 10, 11	6-10	4-7
PKS 2155-304	5-12	1, 6-12	1, 3-12	4-12	5-11	4-10
BL Lacertae		8-11	5-8, 10			6, 9

The table includes the periods of the ATOM monitoring of the selected blazars. The numbers indicate months, in which an object has been observed: 1 is for January, 2 for February, etc. A month number is given when a source was observed a least once in given month.

The study of color-magnitude diagrams for 30 blazars reveals different color behaviors. For 14 objects from the sample the Pearson correlation coefficient is greater than 0.5, which indicates a significant correlation between the optical color and magnitude. The strongest bluer-when-brighter trend is observed for: 1ES 0323+022, 1ES 0347+121, 1ES 1218+304, AP Librae, BL Lacertae, Mrk 421, Mrk 501, PKS 2005-489, RGB J0152+117, SHBL J032541.0-164618, SHBL J101015.9-311908 and W Comae. In the case of 7 of these objects the relation is very strong (correlation coefficient  $> 0.85$ ). The negative relation is found only in two sources: PG 1553+113 and PKS 1424+240, but the correlation is not significant. In the several case color-magnitude plot shows much complex structure, often including substructures with significant color-magnitude relation within.

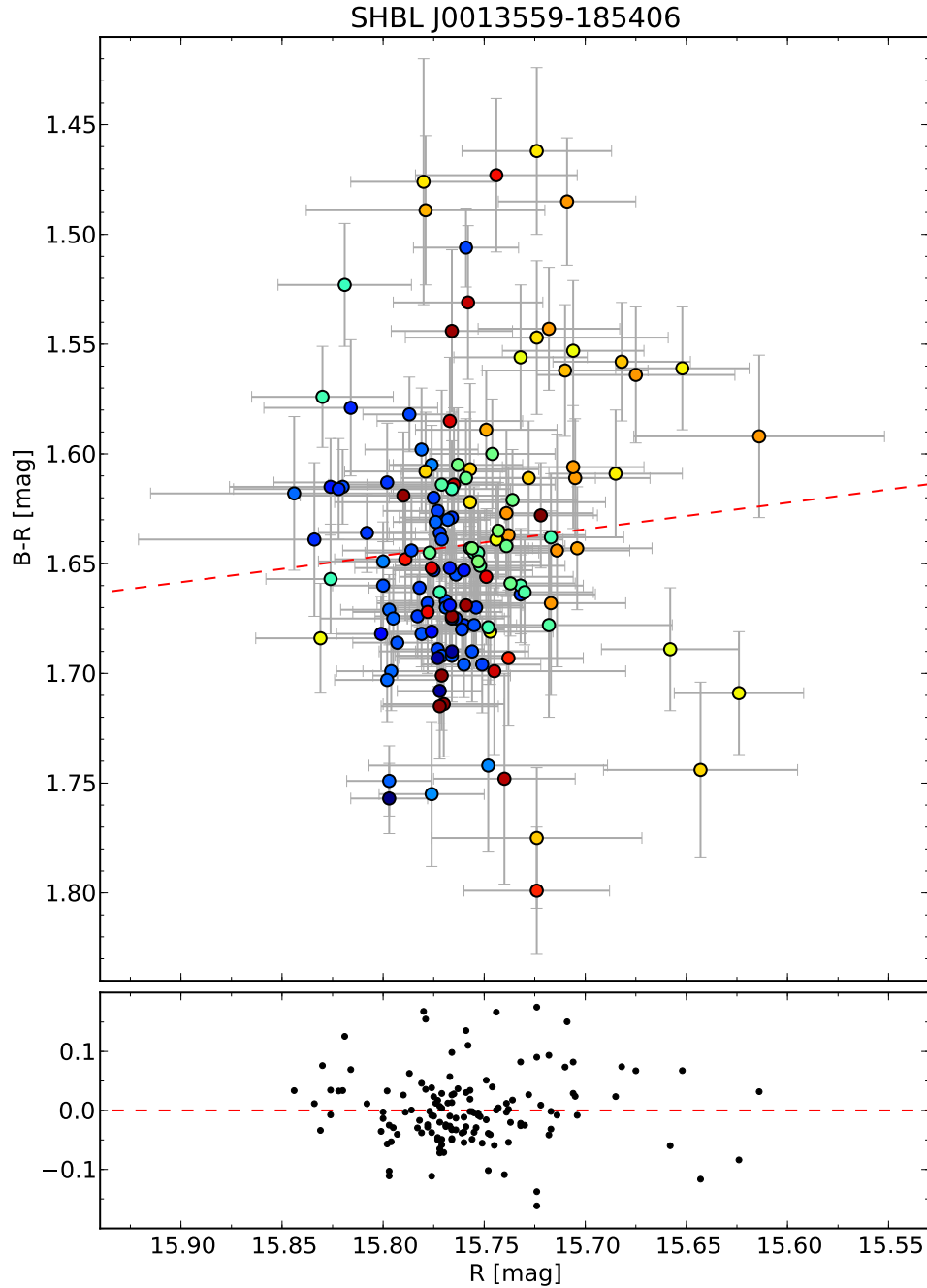


Figure 4.1: The  $B-R$  color index as a function of the  $R$ -band magnitude for the analyzed period for SHBL J001355.9-185406 is shown in the upper panel. The red, dashed line shows the correlation slope. The color of points in the plot is used to denote time: the earliest points are in dark blue, the subsequent points are in blue, then green, yellow, orange, red and the latest points are shown in dark red (see Appendix A). The bottom panel shows the residuals of the linear fit. The correlation coefficient and the slope of the fit are given in Table 4.1.

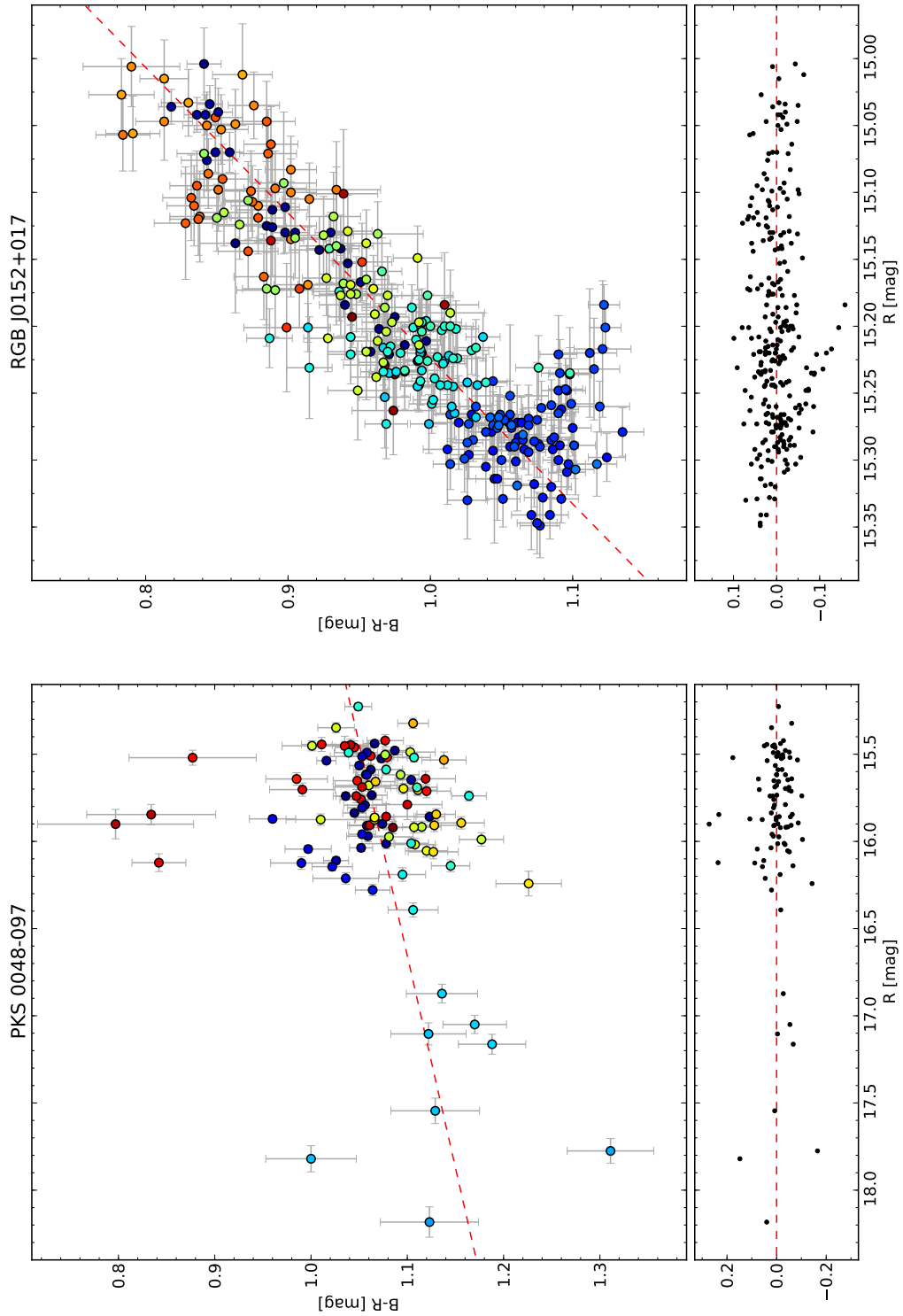


Figure 4.2: The  $B-R$  color index as a function of the  $R$ -band magnitude for the analyzed period for PKS 0048-097 and RGB J0152+017. The detailed explanation of the plot follows Fig. 4.1.

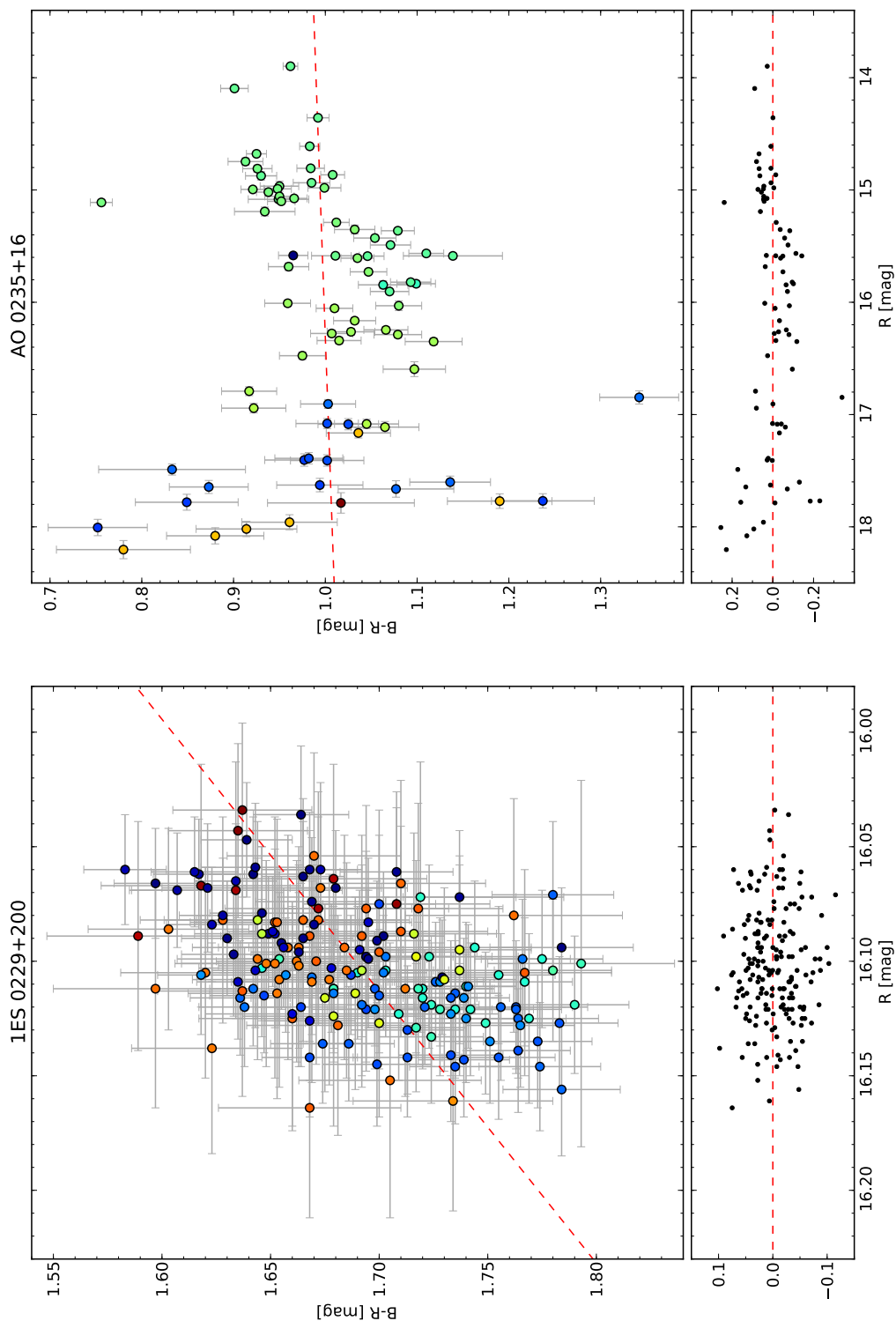


Figure 4.3: The  $B - R$  color index as a function of the  $R$ -band magnitude for the analyzed period for 1ES 0229+200 and AO 0235+16. The detailed explanation of the plot follows Fig. 4.1.

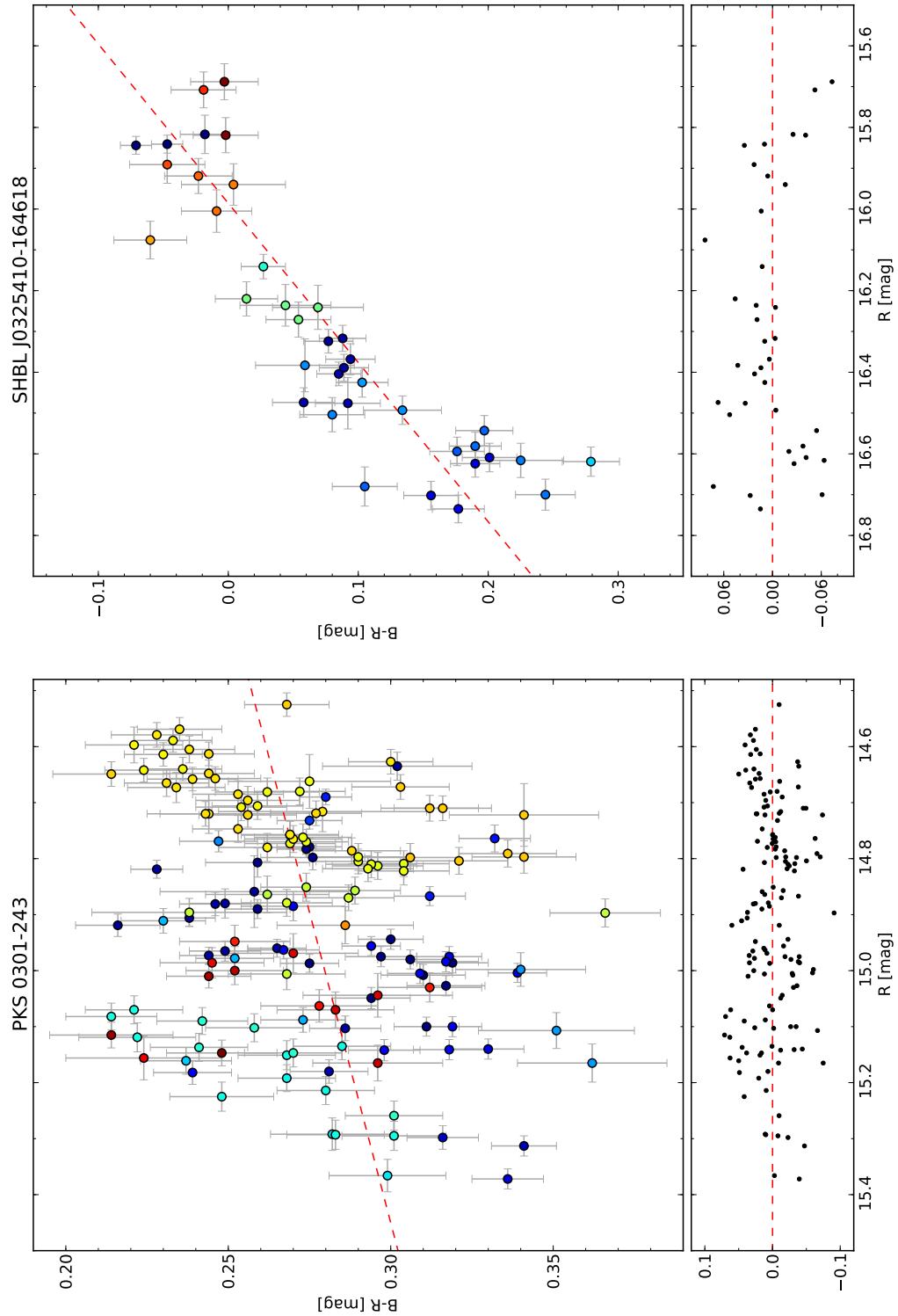


Figure 4.4: The  $B - R$  color index as a function of the  $R$ -band magnitude for the analyzed period for PKS 0301-243 and SHBL J032541.0-164618. The detailed explanation of the plot follows Fig. 4.1.

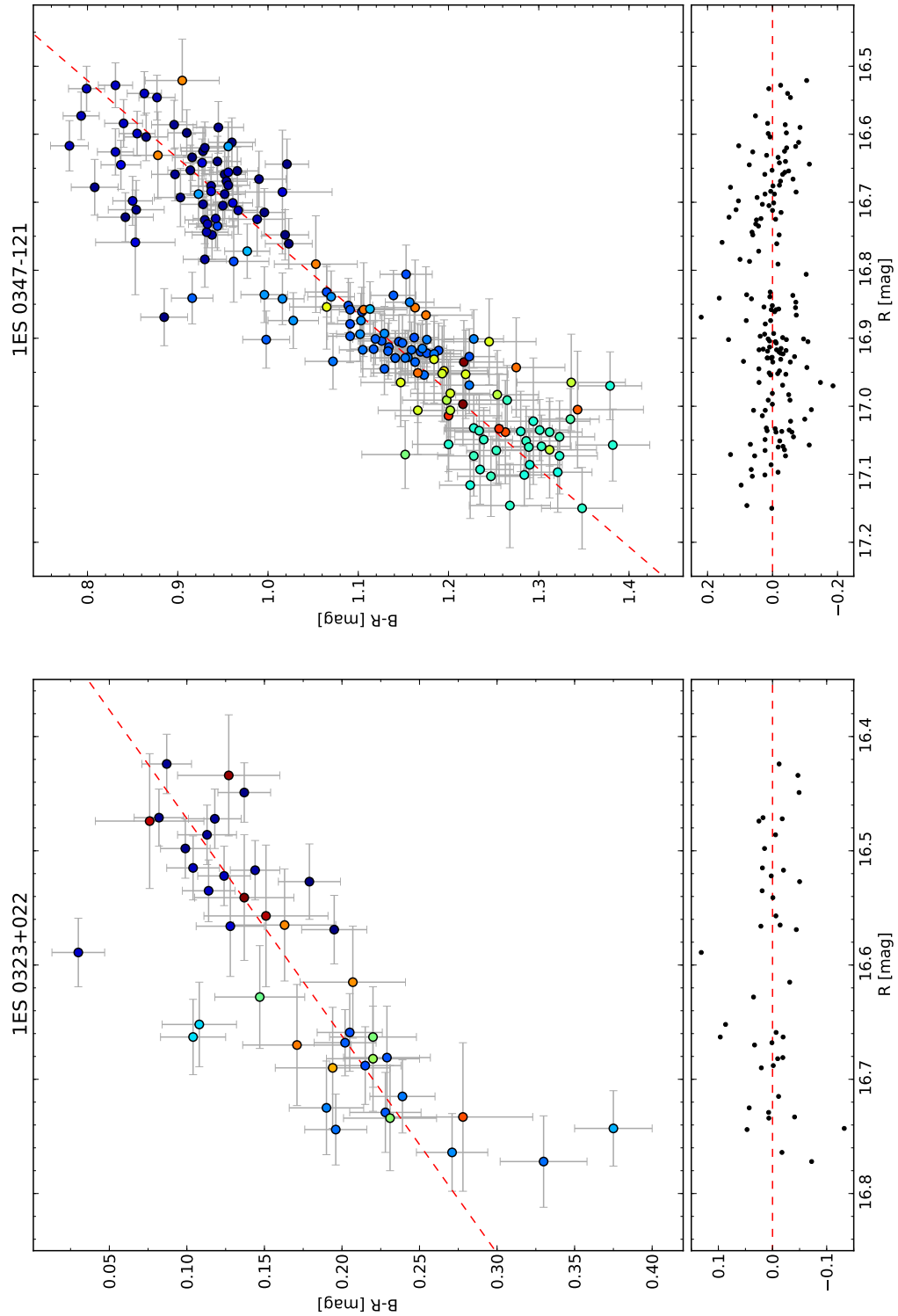


Figure 4.5: The  $B-R$  color index as a function of the  $R$ -band magnitude for the analyzed period for 1ES 0323+022 and 1ES 0347-121. The detailed explanation of the plot follows Fig. 4.1.

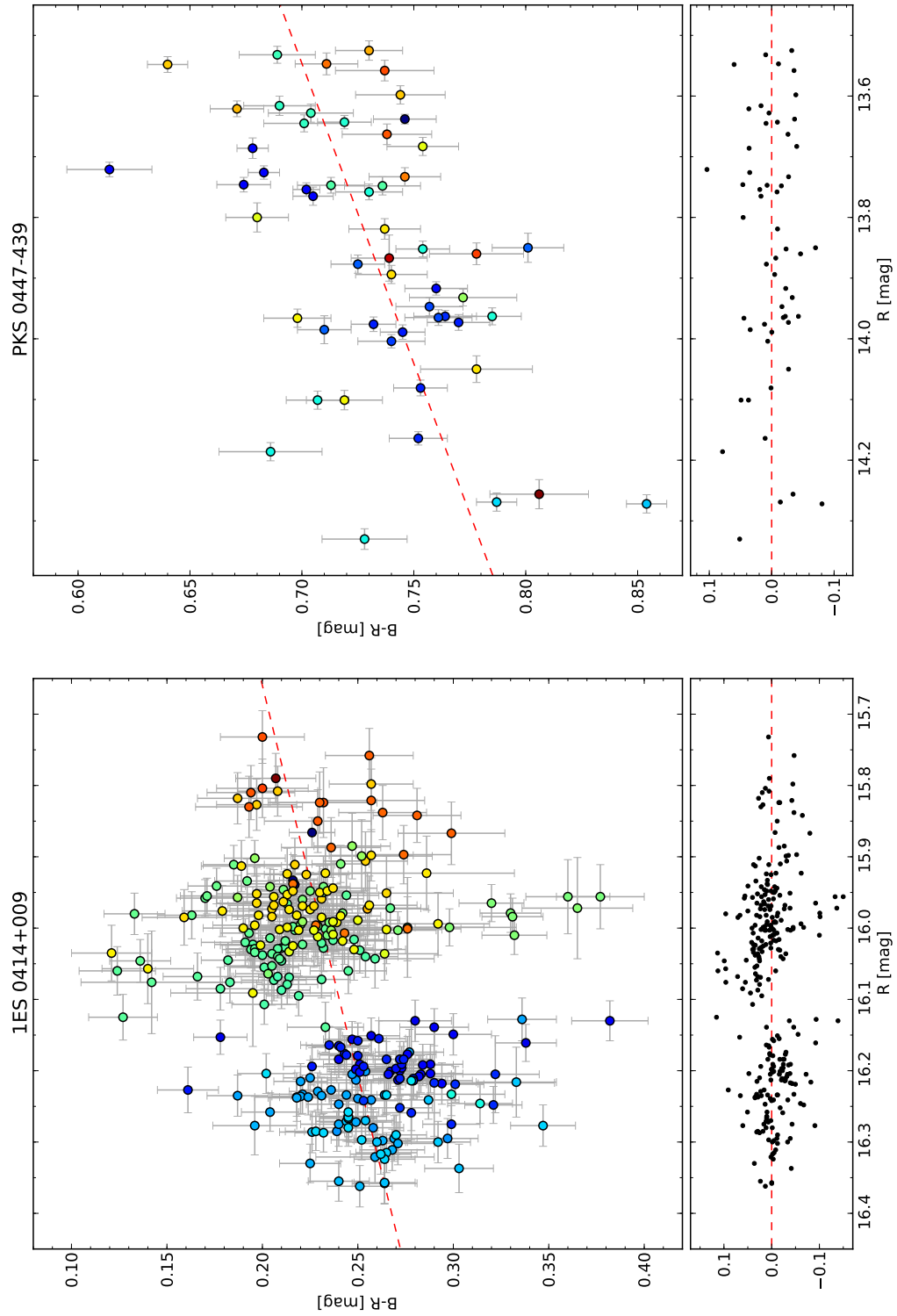


Figure 4.6: The  $B - R$  color index as a function of the  $R$ -band magnitude for the analyzed period for 1ES 0414+00.9 and PKS 0447-439. The detailed explanation of the plot follows Fig. 4.1.

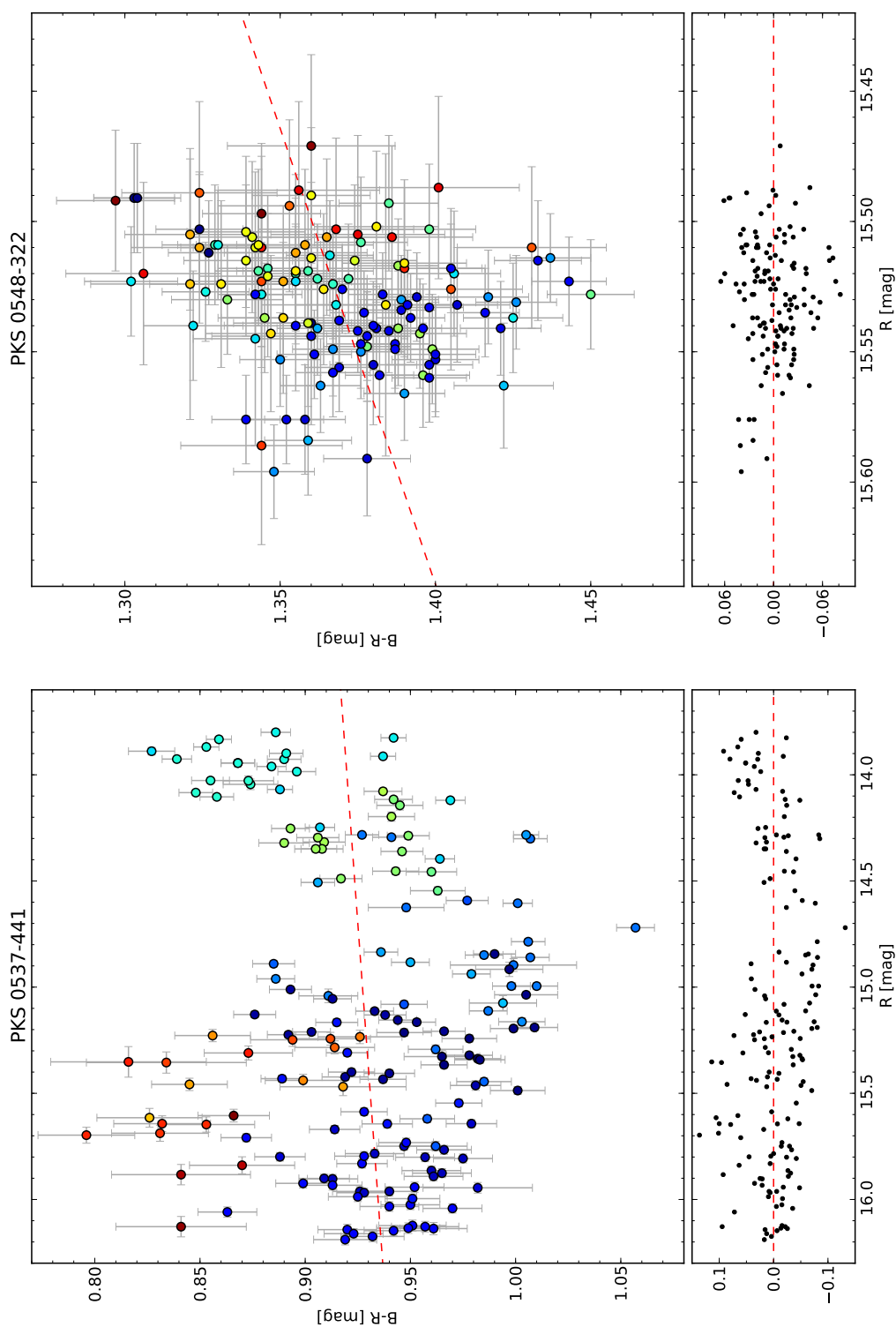


Figure 4.7: The  $B - R$  color index as a function of the  $R$ -band magnitude for the analyzed period for PKS 0537-441 and PKS 0548-322. The detailed explanation of the plot follows Fig. 4.1.

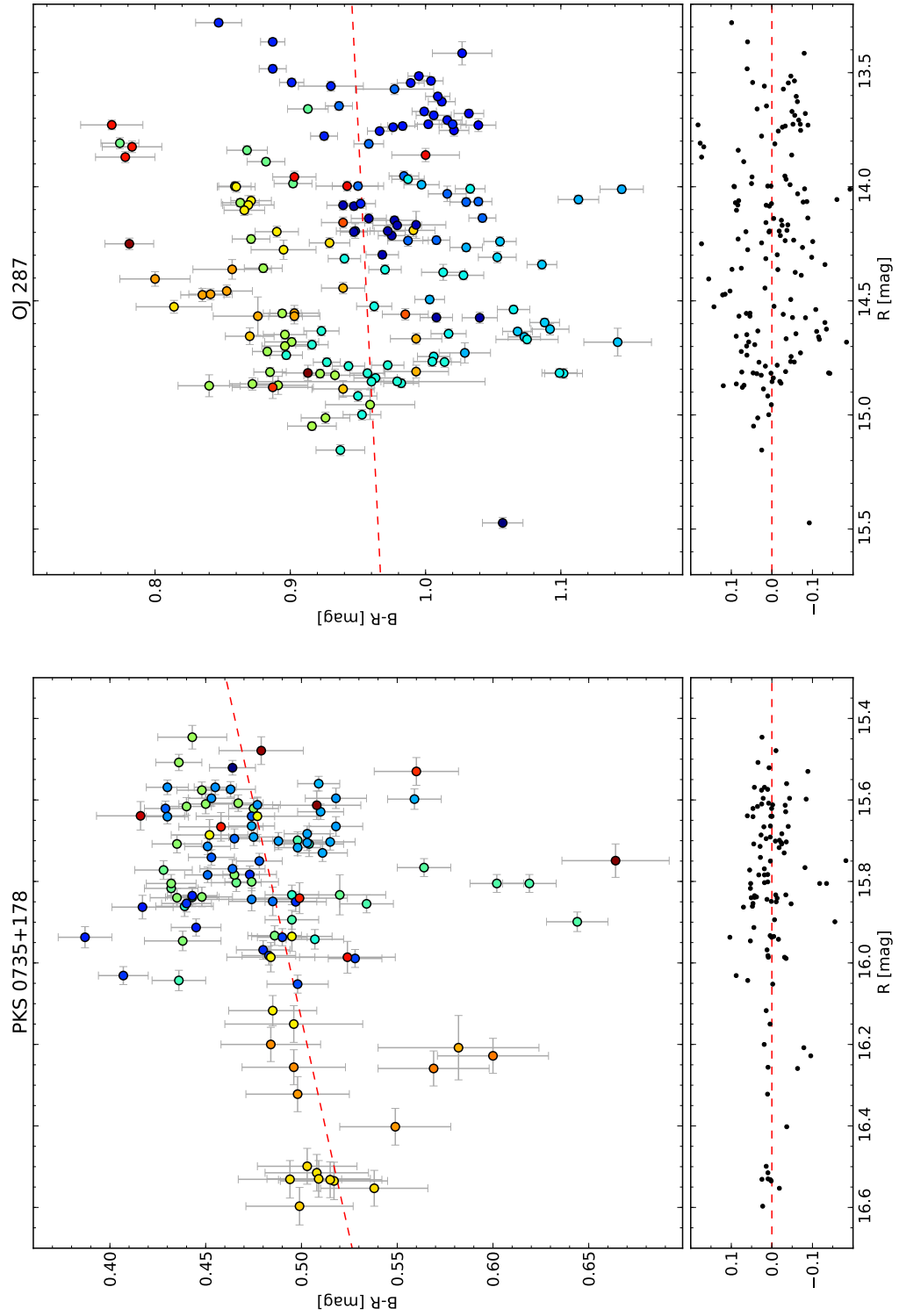


Figure 4.8: The  $B - R$  color index as a function of the  $R$ -band magnitude for the analyzed period for PKS 0735+178 and OJ 287. The detailed explanation of the plot follows Fig. 4.1.

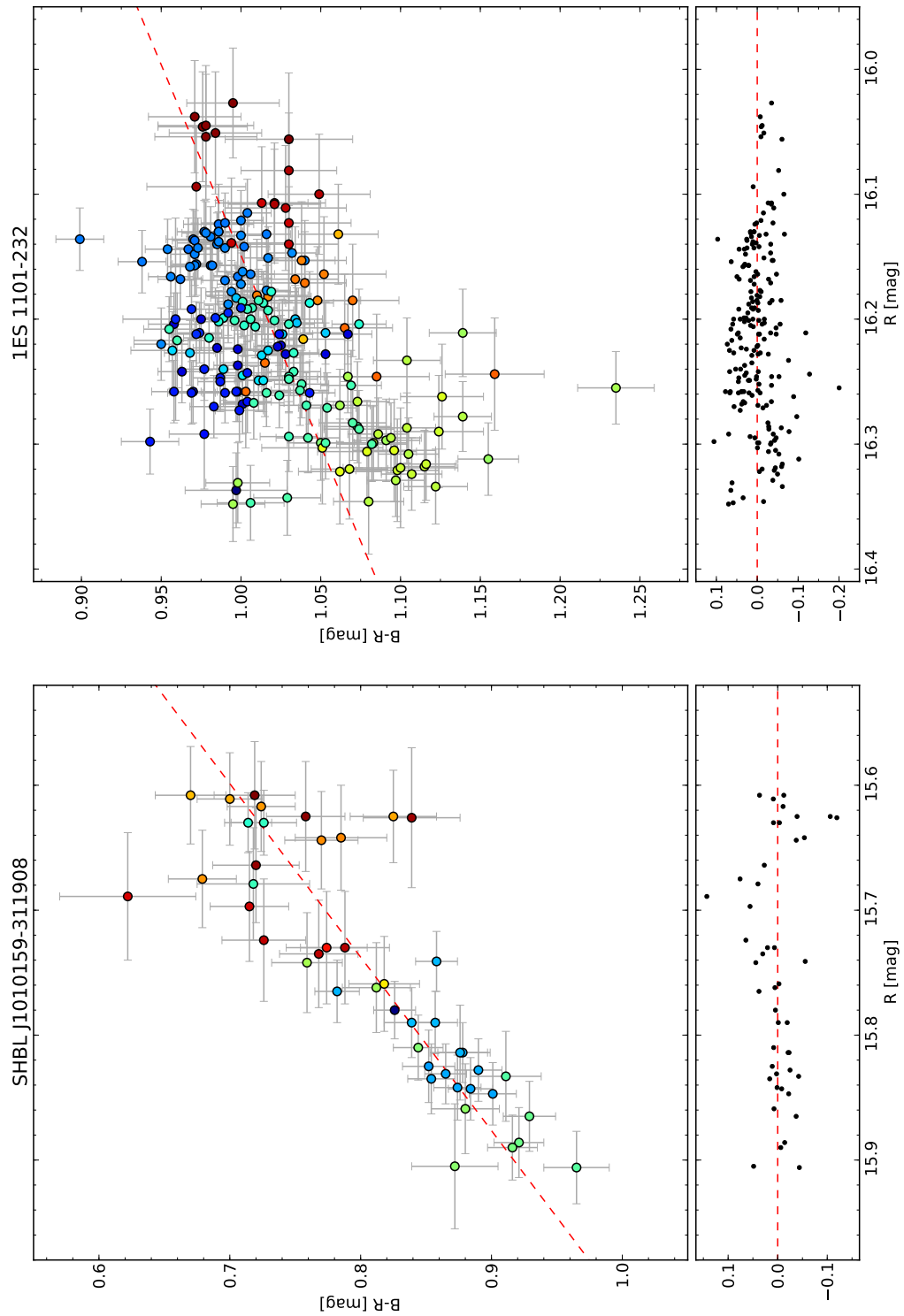


Figure 4.9: The  $B - R$  color index as a function of the  $R$ -band magnitude for the analyzed period for SHBL J101015.9-311908 and 1ES 1101-232. The detailed explanation of the plot follows Fig. 4.1.

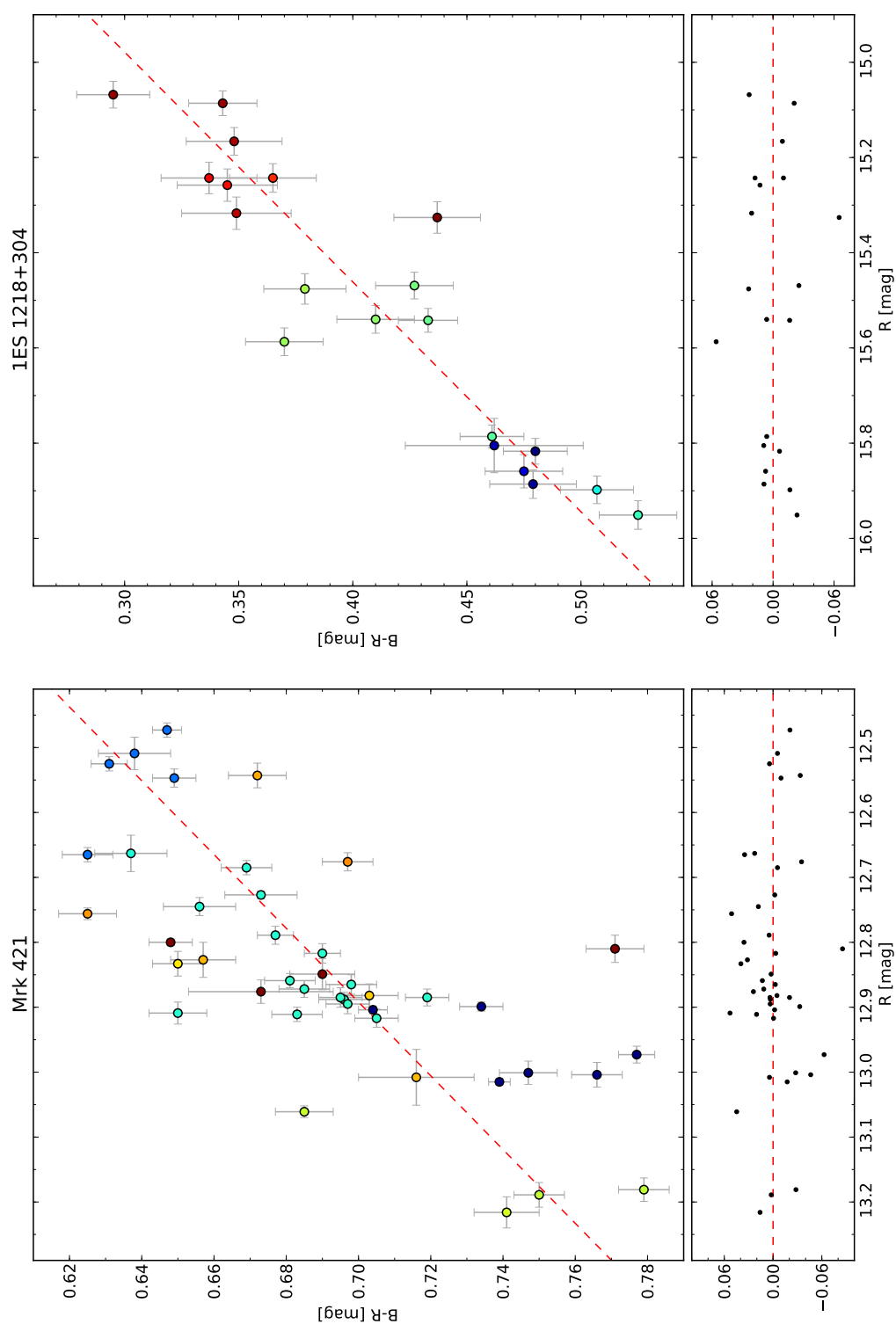


Figure 4.10: The  $B-R$  color index as a function of the  $R$ -band magnitude for the analyzed period for Markarian 421 and 1ES 1218+304. The detailed explanation of the plot follows Fig. 4.1.

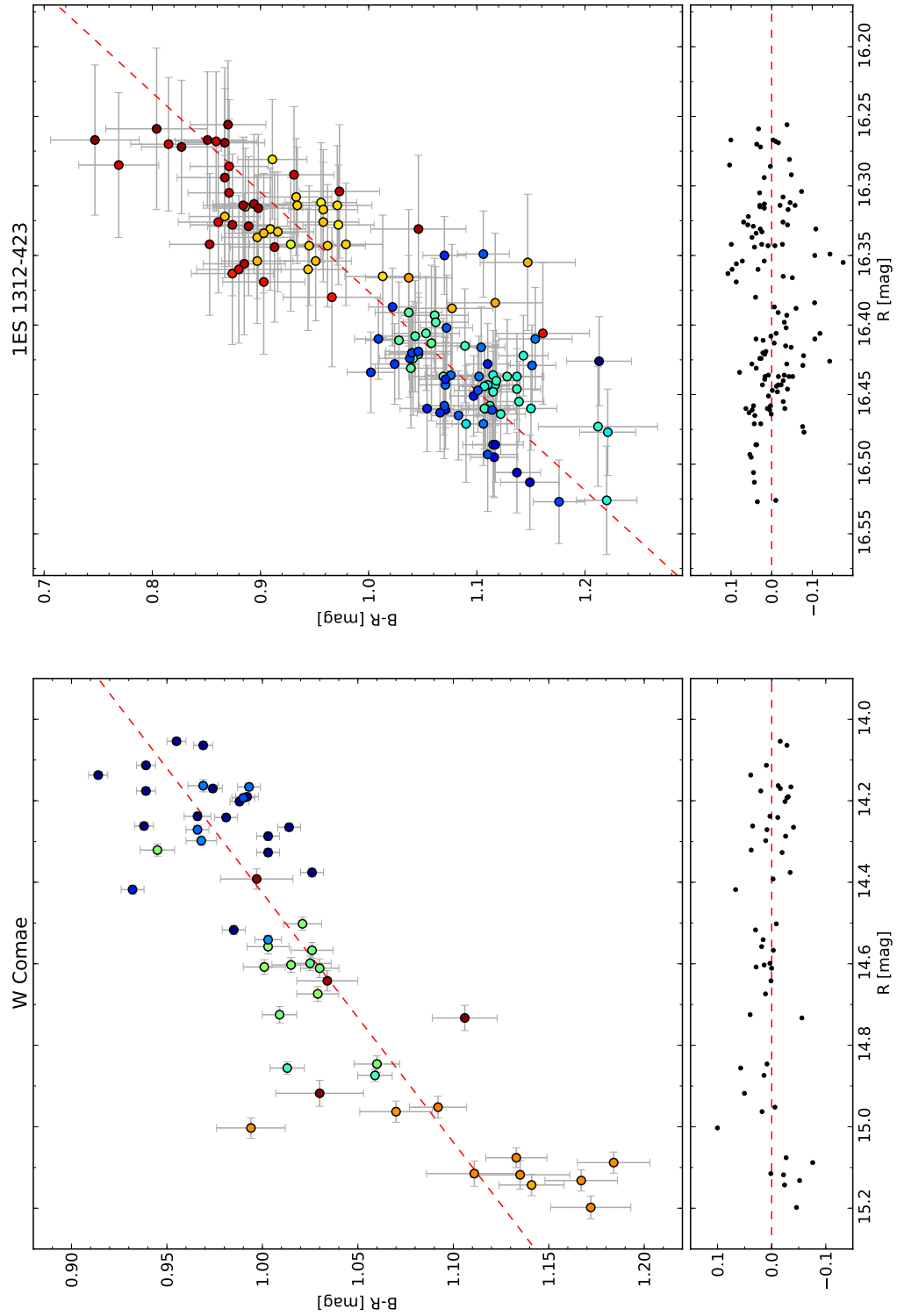


Figure 4.11: The  $B - R$  color index as a function of the  $R$ -band magnitude for the analyzed period for W Comae and 1ES 1312-42. The detailed explanation of the plot follows Fig. 4.1.

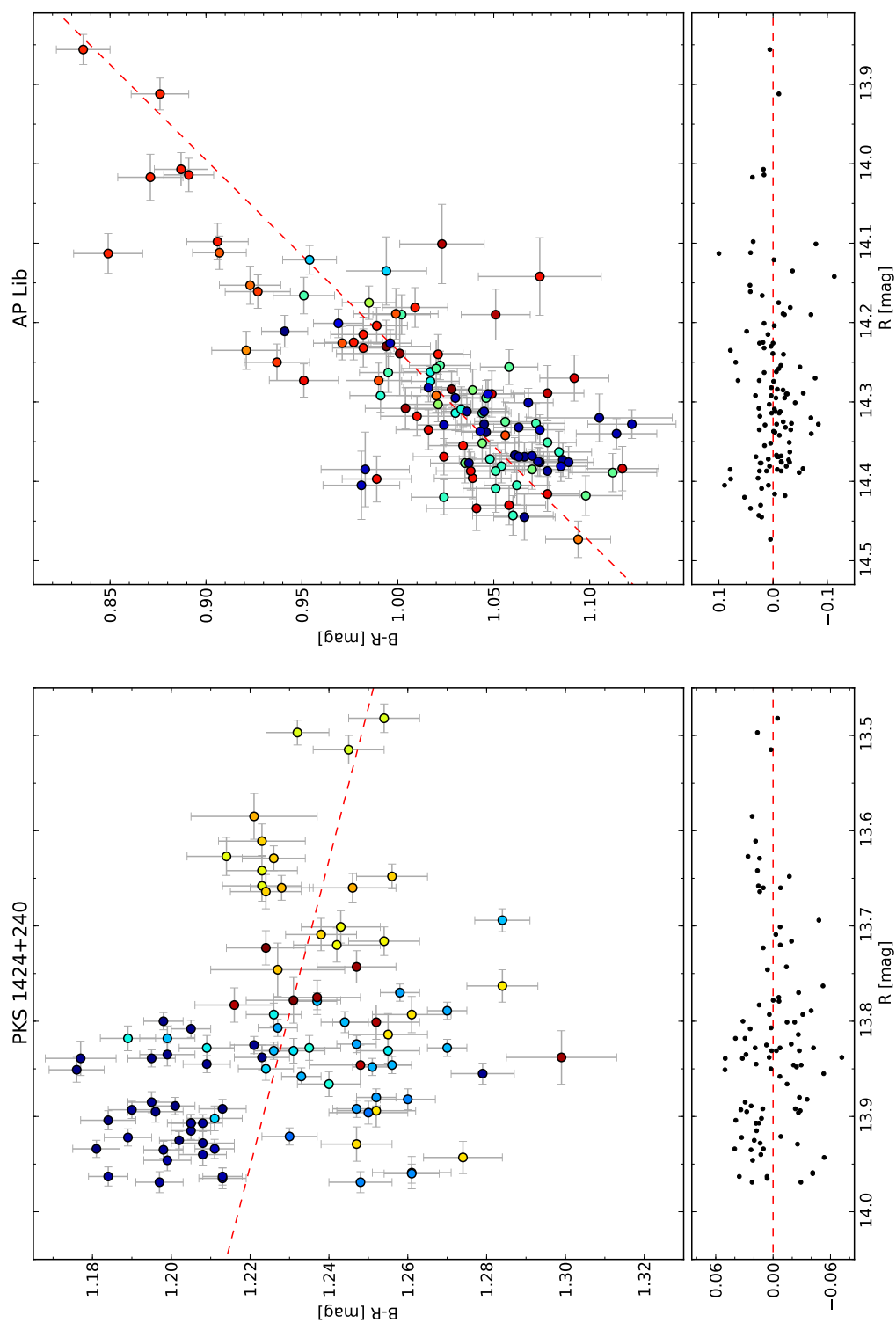


Figure 4.12: The  $B-R$  color index as a function of the  $R$ -band magnitude for the analyzed period for PKS 1424+240 and AP Librae. The detailed explanation of the plot follows Fig. 4.1.

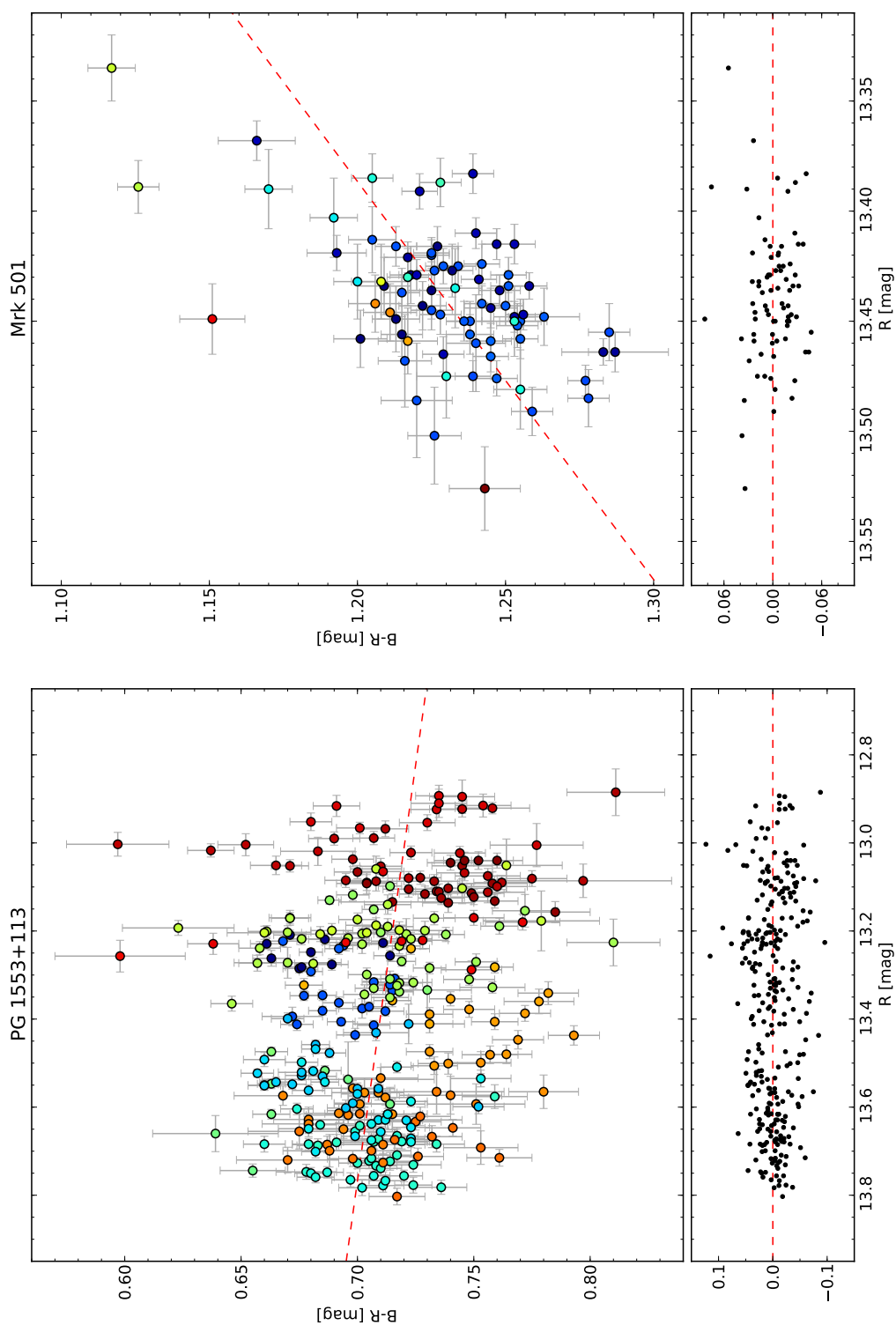


Figure 4.13: The  $B-R$  color index as a function of the  $R$ -band magnitude for the analyzed period for PG 1553+113 and Markarian 501. The detailed explanation of the plot follows Fig. 4.1.

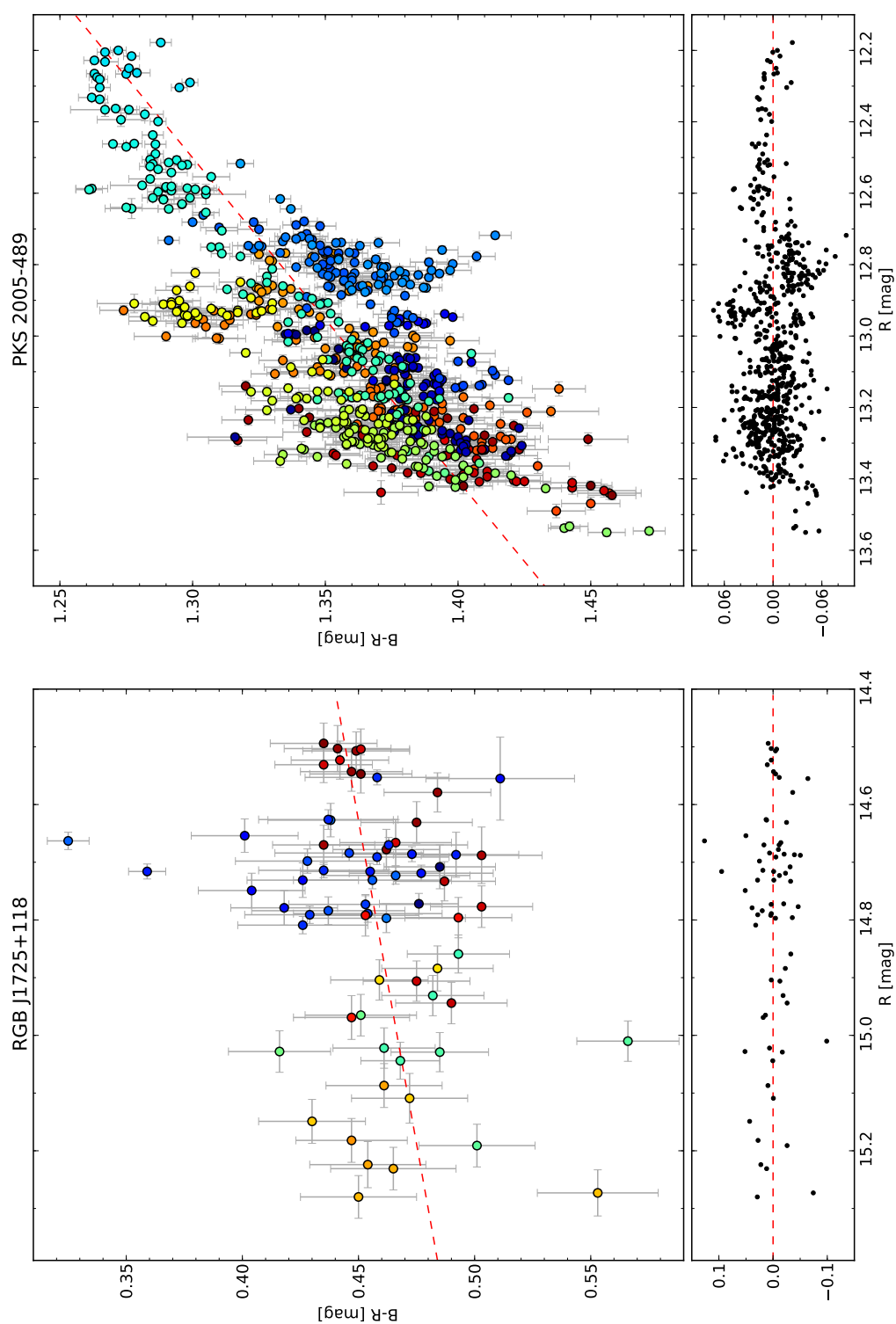


Figure 4.14: The  $B-R$  color index as a function of the  $R$ -band magnitude for the analyzed period for RGB J1725+118 and PKS 2005-489. The detailed explanation of the plot follows Fig. 4.1.

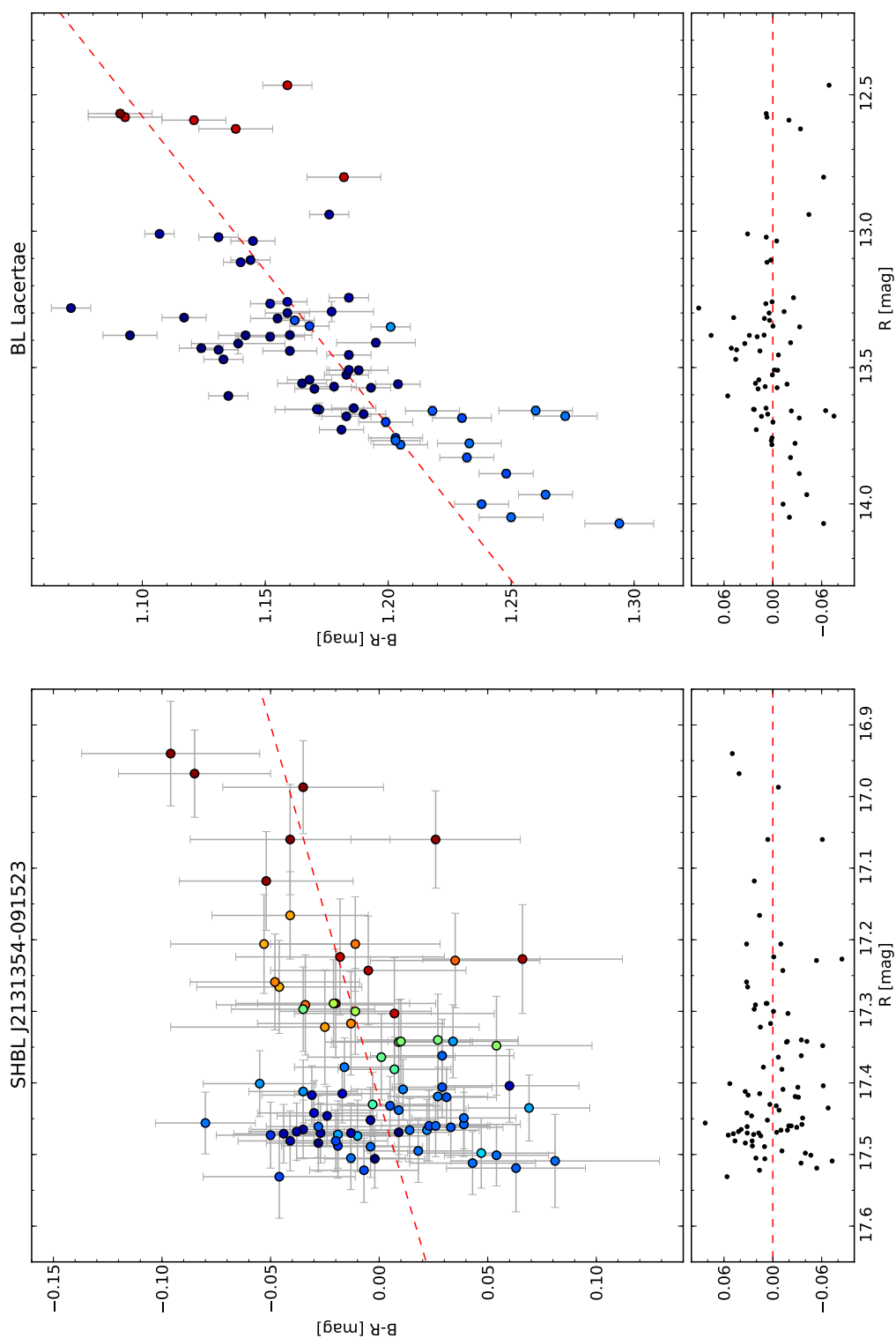


Figure 4.15: The  $B-R$  color index as a function of the  $R$ -band magnitude for the analyzed period for SHBL J213135.4-091523 and BL Lacertae. The detailed explanation of the plot follows Fig. 4.1.

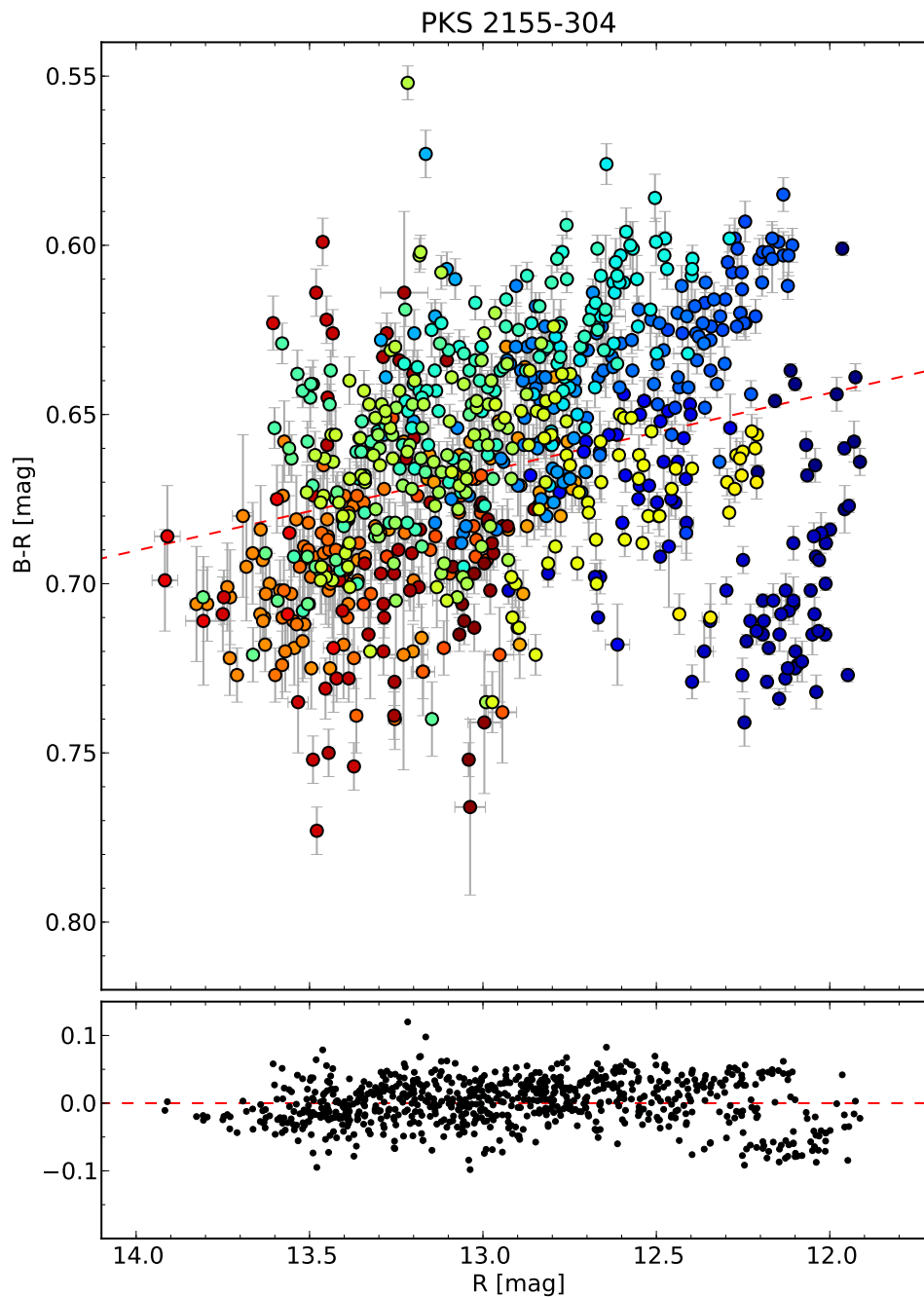


Figure 4.16: The  $B-R$  color index as a function of the  $R$ -band magnitude for the analyzed period for PKS 2155-304. The detailed explanation of the plot follows Fig. 4.1.

### 4.3 Multiwavelength properties of the ATOM blazars

In the further studies of the ATOM blazars, the optical observations are compared with quasi-simultaneous HE  $\gamma$ -ray and radio observations. The  $\gamma$ -ray data are taken from the Second Catalog of Fermi Sources (2FGL, Nolan et al. 2012) which is based on data in the 100 MeV to 100 GeV energy range. The radio observations, at 15 GHz come from The Owens Valley Radio Observatory (OVRO), a 40 m telescope dedicated to observe the Fermi-LAT targets (Richards et al. 2011).

It should be noted here that the ATOM data are from 2007-2012. The Second Fermi Catalog includes observation collected during the first 24 months of the science phase of the mission (Fermi was launched on the 11th of June 2008 at 16:05 GMT). The presented radio data were collected during the period 2008-2012 in the sources' visibility windows. These observations are here called quasi-simultaneous.

The comparison of the blazars' mean luminosities in the radio, optical ( $R$  filter) and gamma-ray bands are presented in Table 4.3. The content of this table is graphically shown in Figures 4.17 and 4.18. Each plot compares the radio, optical and gamma-ray luminosities, each blazar is represented by a single point in the plot. Different point shapes are used for indication of different blazars types: circles for high energy peaked (HBL), triangles for intermediate energy peaked (IBL) and stars for low energy peaked BL Lac objects (LBL).

The presented mean luminosities seem to be correlated, the brightest optical objects are also very bright in the radio and GeV ranges. It must be noted, that the considered observations are only quasi-simultaneous, which may lead to the fact that not all flares are included. In spite of this, the correlation coefficients for the correlations of luminosities are in all cases of about 0.9.

In Figure 4.19 the Fermi spectral index is compared to the optical luminosity of the ATOM blazars. The color of points in the plots corresponds to the value of the Pearson's correlation coefficient of the optical color-magnitude relation. The comparison shows that the sources characterized by a significant and positive color-magnitude correlation are HBLs, which are low-luminosity objects with flat GeV spectra (with Fermi indices  $< 2.0$ ). On the other hand, sources with only weak or even negative color-magnitude correlations are LBLs, which are higher-luminosity objects with steep GeV spectra (with Fermi indices  $> 2.0$ ).

The comparison of the luminosity in the GeV range and the average  $B - R$  optical color is presented in Fig. 4.20. The plots show no correlation between these two quantities. They also show that in the case of HBL type blazars the  $B - R$  color covers the range from 0.1 mag to 1.4 mag. In the case of the two other subclasses of BL Lac blazars this ranges are much narrower. It must be also underlined here that higher values of correlation coefficients of the color-magnitude relations seem to be characteristic for less

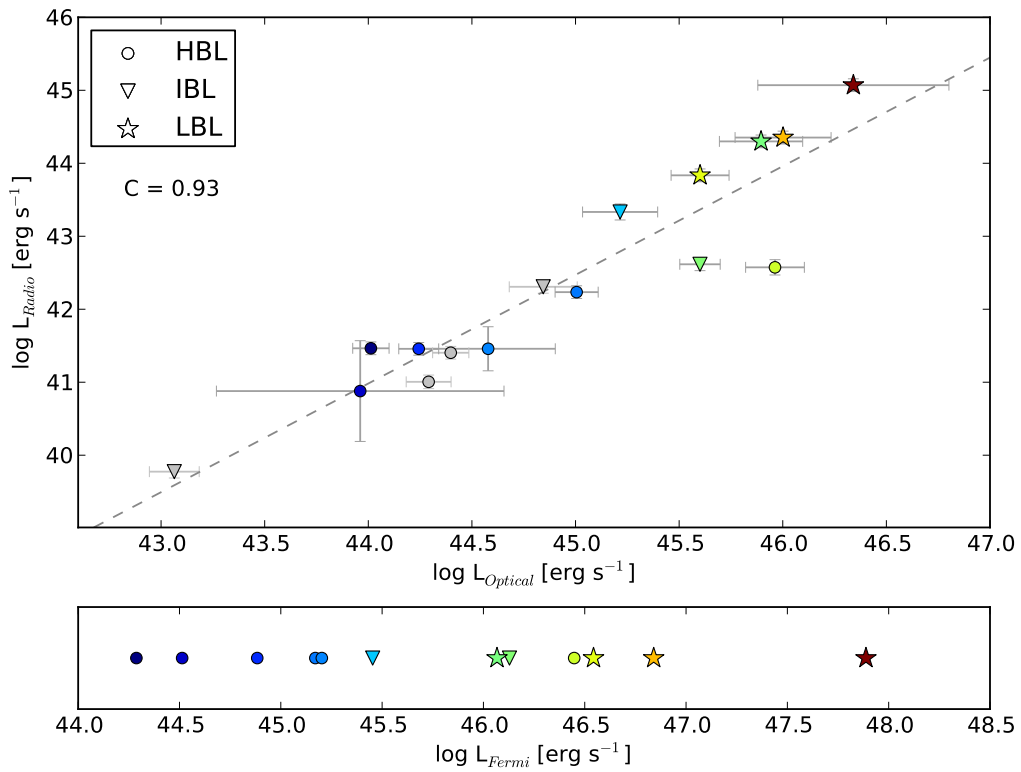


Figure 4.17: The comparison of gamma-ray, radio and optical luminosities of the ATOM blazars. The upper panel shows the relation between radio and optical luminosities. The color of the points depicts gamma-ray luminosity for a given blazar and the color-value coding is shown in the lower panel. If there is no complementary gamma-ray observations a gray color is used. The different point symbols are used for indication of different blazars types: circles for HBLs, triangles for IBLs and stars for LBLs. The correlation coefficient between radio and optical luminosities is 0.93.

luminous objects, typically HBLs. Analogous remarks are valid for the comparison of the optical luminosity and  $B - R$  optical color and the comparison of the radio luminosity and  $B - R$  optical color (see Fig. 4.21 and Fig. 4.22).

There is no significant correlation between the optical luminosity and the value of the optical color-magnitude correlation coefficient, presented in Fig. 4.23. On the other hand the plot suggests that the bluer-when-brighter chromatism is not strictly related to the type of the BL Lac blazars, but only occur in objects with optical luminosity below  $\sim 10^{45}$  erg s<sup>-1</sup>. Above this luminosity there are no sources with a significant color-magnitude correlation in selected sample.

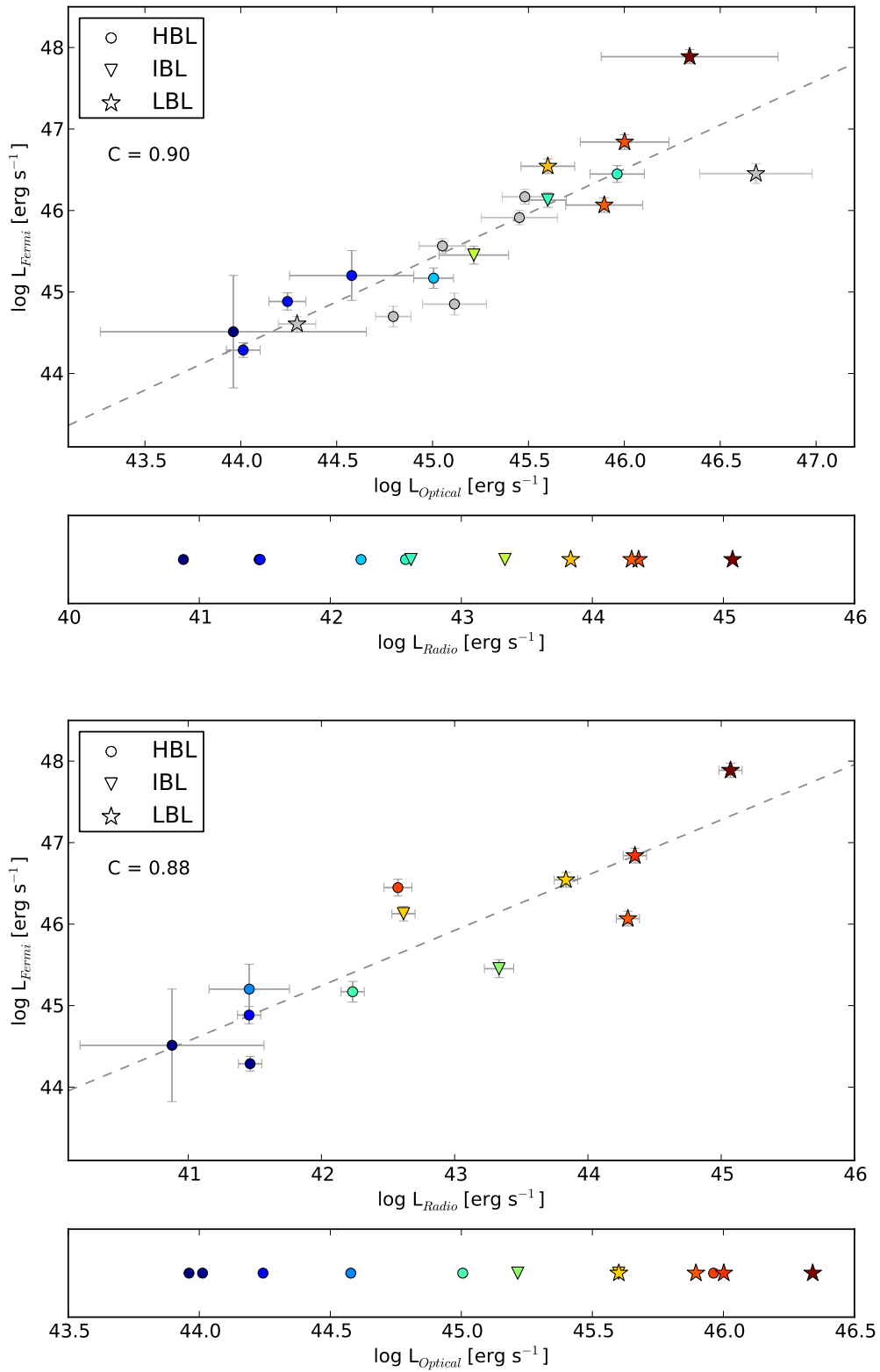


Figure 4.18: The comparison of the radio, optical and gamma-ray luminosities of the ATOM blazars. The meaning of symbols and colors are analogical to those described in Figure 4.17.

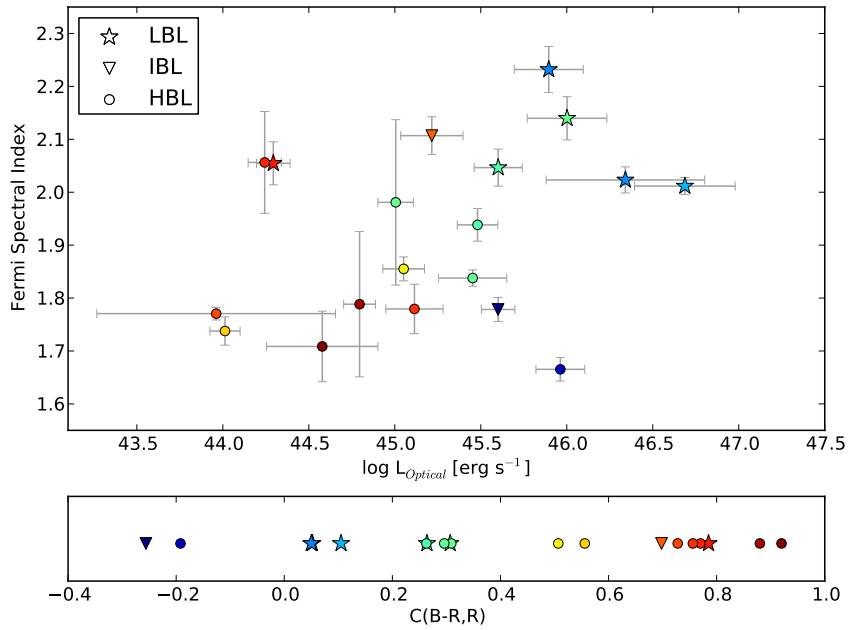


Figure 4.19: The comparison of the gamma-ray spectral index and optical luminosity. A color coding is used to show values of the color-magnitude correlation coefficients for the ATOM blazars. The different point symbols are used for different blazar types: circles for HBLs, triangles for IBLs and stars for LBLs.

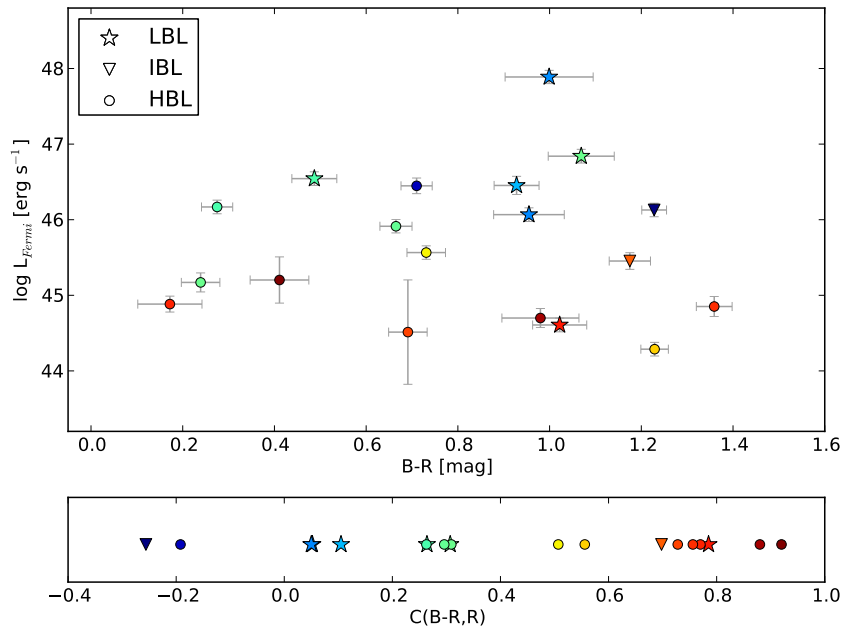


Figure 4.20: The comparison of the gamma-ray luminosity and the  $B - R$  optical color. A color coding is used to show values of the color-magnitude correlation coefficient for the ATOM blazars. The point symbols have the same meaning as in Figure 4.19.

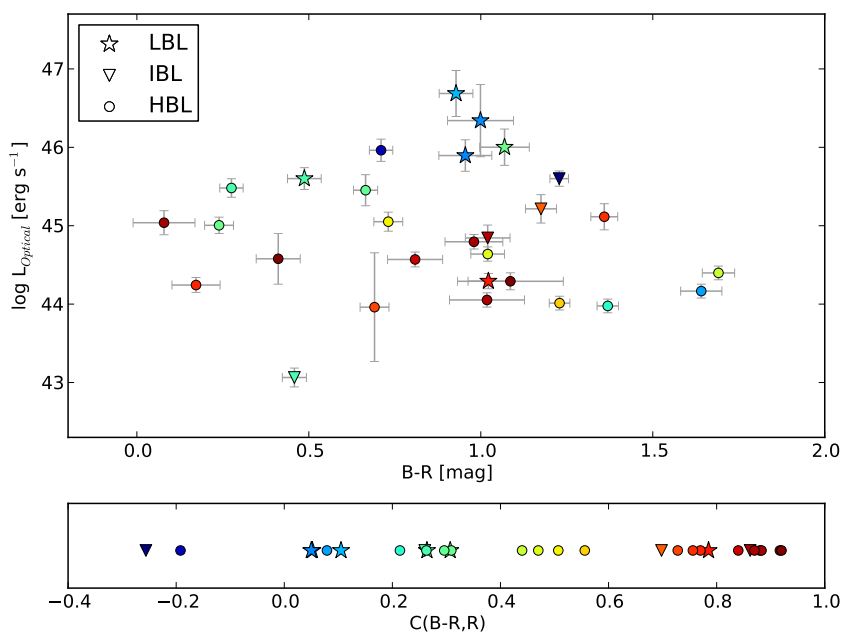


Figure 4.21: The optical luminosity versus the  $B - R$  optical color. A color coding is used to show values of the color-magnitude correlation coefficient for the analyzed blazars. The point symbols have the same meaning as in Figure 4.19.

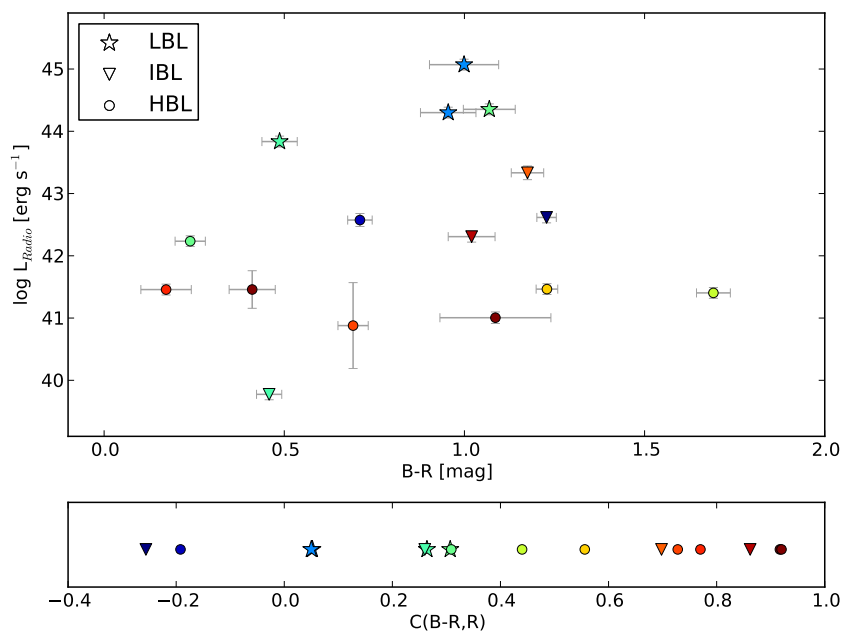


Figure 4.22: The radio luminosity versus the  $B - R$  optical color. A color coding is used to show values of the color-magnitude correlation coefficient for the ATOM blazars. The point symbols have the same meaning as in Figure 4.19.

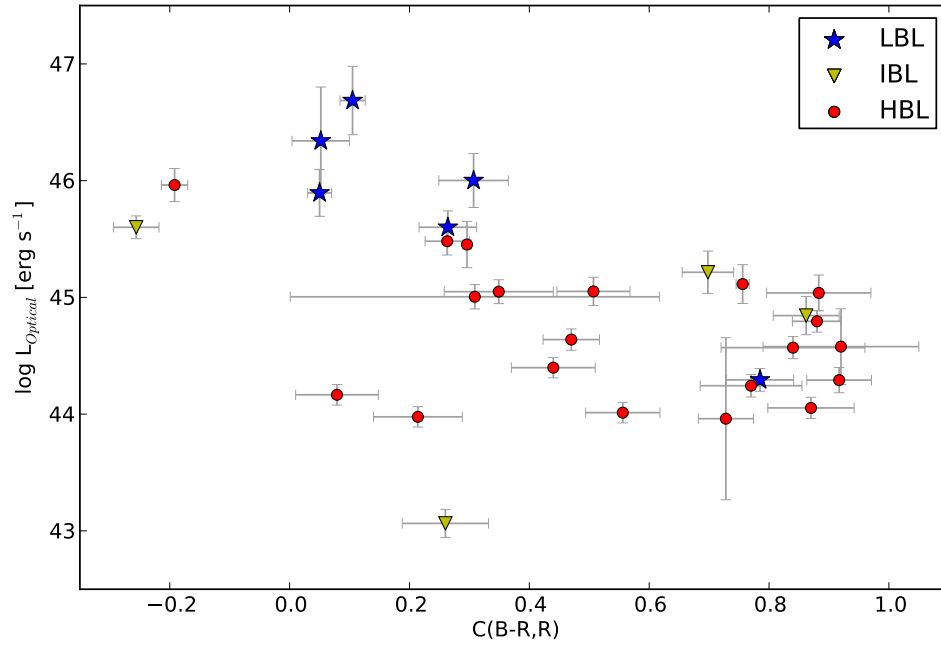


Figure 4.23: The comparison of the optical luminosity of the ATOM blazars and color-magnitude correlation coefficient. The different point symbols and colors are used for different blazars types: red circles for HBLs, yellow triangles for IBLs and blue stars for LBLs.

Table 4.3: The summary of the ATOM blazars luminosities.

Object (1)	Distance [Mpc] (2)	$L_{\text{optical}}$ [ergs $^{-1}$ ] (3)	$L_{\text{Radio}}$ [ergs $^{-1}$ ] (4)	$L_{\text{fermi}}$ [ergs $^{-1}$ ] (5)	Spectral Index (6)
SHBL J001355.9-185406	413	$(1.5 \pm 0.3) \cdot 10^{44}$	$(2.3 \pm 0.5) \cdot 10^{44}$	$(6.9 \pm 1.4) \cdot 10^{46}$	$2.14 \pm 0.04$
PKS 0048-097	3659	$(1.0 \pm 0.5) \cdot 10^{46}$		$(5.0 \pm 1.5) \cdot 10^{44}$	$1.79 \pm 0.14$
RGB J0152+017	660*	$(6.2 \pm 1.3) \cdot 10^{44}$			
1ES 0229+200	632	$(2.5 \pm 0.5) \cdot 10^{44}$	$(2.5 \pm 0.5) \cdot 10^{40}$	$(7.7 \pm 1.6) \cdot 10^{47}$	$2.02 \pm 0.03$
AO 0235+16	5967	$(2.2 \pm 2.0) \cdot 10^{46}$	$(1.2 \pm 0.2) \cdot 10^{45}$	$(1.5 \pm 0.3) \cdot 10^{46}$	$1.94 \pm 0.03$
PKS 0301-243	1268	$(3.0 \pm 0.8) \cdot 10^{45}$			
HBL J032541.0-164618	1444	$(1.1 \pm 0.4) \cdot 10^{45}$			
1ES 0323+022	668	$(1.8 \pm 0.4) \cdot 10^{44}$	$(2.9 \pm 0.6) \cdot 10^{41}$	$(7.7 \pm 1.9) \cdot 10^{44}$	$2.06 \pm 0.09$
1ES 0347-121	788*	$(1.9 \pm 0.5) \cdot 10^{44}$	$(1.0 \pm 0.2) \cdot 10^{41}$		
1ES 0414+00.9	1260*	$(1.0 \pm 0.2) \cdot 10^{45}$	$(1.7 \pm 0.3) \cdot 10^{42}$	$(1.5 \pm 0.4) \cdot 10^{45}$	$1.99 \pm 0.16$
PKS 0447-439	476	$(1.1 \pm 0.3) \cdot 10^{45}$		$(3.7 \pm 0.8) \cdot 10^{45}$	$1.86 \pm 0.02$
PKS 0537-441	5613	$(4.9 \pm 3.3) \cdot 10^{46}$		$(2.8 \pm 0.8) \cdot 10^{46}$	$2.01 \pm 0.02$
PKS 0548-322	299*	$(9.5 \pm 1.9) \cdot 10^{43}$			
PKS B0735+178	2256	$(4.0 \pm 1.3) \cdot 10^{45}$	$(6.8 \pm 1.4) \cdot 10^{43}$	$(3.5 \pm 0.7) \cdot 10^{46}$	$2.05 \pm 0.04$
OJ 287	1537	$(7.9 \pm 3.6) \cdot 10^{45}$	$(2.0 \pm 0.4) \cdot 10^{44}$	$(1.2 \pm 0.2) \cdot 10^{46}$	$2.23 \pm 0.04$
HBL J101015.9-311908	655	$(3.7 \pm 0.8) \cdot 10^{44}$			
1ES 1101-232	877	$(4.4 \pm 0.9) \cdot 10^{44}$			
Mrk 421	85.15 $\pm$ 67.67*	$(0.9 \pm 0.8) \cdot 10^{44}$	$(0.8 \pm 0.6) \cdot 10^{41}$	$(3.3 \pm 3.2) \cdot 10^{44}$	$1.771 \pm 0.012$
1ES 1218+304	594.00 $\pm$ 206.48*	$(3.8 \pm 2.8) \cdot 10^{44}$	$(2.9 \pm 2.0) \cdot 10^{41}$	$(1.6 \pm 1.1) \cdot 10^{45}$	$1.71 \pm 0.07$
W Comae	517*	$(7.0 \pm 2.6) \cdot 10^{44}$	$(2.0 \pm 0.4) \cdot 10^{42}$		
1ES 1312-423	485	$(1.1 \pm 0.2) \cdot 10^{44}$			
PKS 1424+240	882*	$(4.0 \pm 0.9) \cdot 10^{45}$	$(4.1 \pm 0.8) \cdot 10^{42}$	$(1.4 \pm 0.3) \cdot 10^{46}$	$1.78 \pm 0.02$
AP Lib	243*	$(2.0 \pm 0.4) \cdot 10^{44}$		$(4.1 \pm 0.9) \cdot 10^{44}$	$2.06 \pm 0.04$
PG 1553+113	1090.00 $\pm$ 127.28*	$(9.2 \pm 3.0) \cdot 10^{45}$	$(3.8 \pm 0.9) \cdot 10^{42}$	$(2.8 \pm 0.7) \cdot 10^{46}$	$1.67 \pm 0.02$
Mrk 501	119*	$(1.0 \pm 0.2) \cdot 10^{44}$	$(2.9 \pm 0.6) \cdot 10^{41}$	$(1.9 \pm 0.4) \cdot 10^{44}$	$1.74 \pm 0.03$
RGB J1725+118	74.6	$(1.2 \pm 0.3) \cdot 10^{43}$	$(6.0 \pm 1.2) \cdot 10^{39}$	$(7.1 \pm 2.2) \cdot 10^{44}$	$1.78 \pm 0.05$
PKS 2005-489	351.50 $\pm$ 51.62*	$(1.3 \pm 0.5) \cdot 10^{45}$			
HBL J213135.4-091523	2405	$(1.1 \pm 0.3) \cdot 10^{45}$			
PKS 2155-304	492*	$(2.8 \pm 1.3) \cdot 10^{45}$		$(8.2 \pm 1.7) \cdot 10^{45}$	$1.838 \pm 0.015$
BL Lacertae	472.0 $\pm$ 59.4*	$(1.6 \pm 0.7) \cdot 10^{45}$	$(2.2 \pm 0.5) \cdot 10^{43}$	$(2.8 \pm 0.7) \cdot 10^{45}$	$2.11 \pm 0.04$

(1) Object name. (2) The distance to the object based on NED. If object is marked with \* the metric distance is used, otherwise the luminosity one. If there is no distance uncertainty a 10% uncertainty is assumed for further analysis. (3) Optical luminosity in R band. (4) Radio luminosity based on OVRO monitoring (Richards et al. 2011). (5) Gamma-ray luminosity based on 2FGL (Nolan et al. 2012). (6) Gamma-ray spectral index, taken from 2FGL.

# H.E.S.S. observations of PKS 2155-304

The analysis of the color-magnitude diagrams for 30 BL Lacs shows variety of behaviors of these sources in the optical band. In several cases the color-magnitude plots are complex, with several substructures. For the further analysis in the VHE  $\gamma$ -rays and studies of the relation between optical and gamma-ray emission of the blazar, one bright object has been chosen. This is PKS 2155-304, the source with the longest simultaneous monitoring in both bands: optical with the ATOM telescope and VHE gamma-ray with the H.E.S.S. telescopes.

## 5.1 Selected observations

The source has been observed by four H.E.S.S. telescopes in each year since 2004 and it is one of the best monitored source by H.E.S.S.. There are only a few blazars, which can be detected by H.E.S.S. during their quiescence states in short (hour-scale) exposures. One of them is PKS 2155-304, what allows for interesting physical studies of the sources. Every year, the source is observed during its visibility window which spans, typically from May to December (see a visibility plot in Fig. 5.1).

The observations presented here include data collected in archival campaigns (2004-2011) and in 2012, which were conducted within a multiwavelength observational campaign, described in Appendix D. The author of this thesis was a principal investigator of this project. The observations performed in proposal were carried out, but due to bad weather conditions and H.E.S.S. II tests, the number of hours of observations was smaller than expected. No ToO observations were carried out.

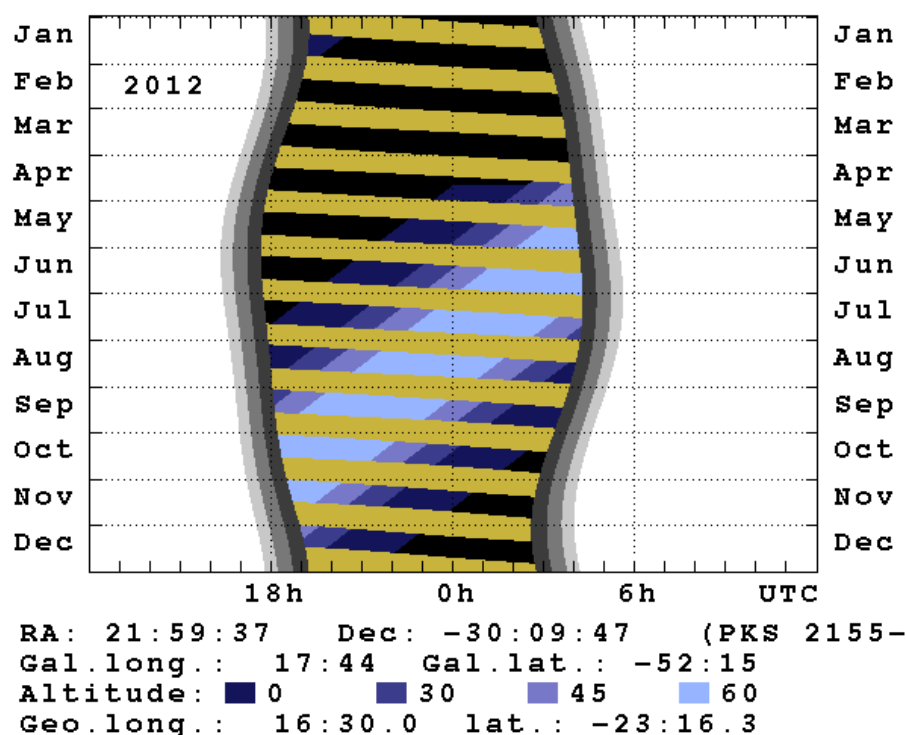


Figure 5.1: The visibility of PKS 2155-304 in 2012. Dates indicated on the right-hand side correspond to the day starting at midnight. The Sun is up during the times indicated by the white areas. Grey levels: light, dark and very dark correspond to civil, naval, and astronomical twilight (or dawn), respectively. The moon is up or making twilight in the yellow areas. The times when the object is above 0, 30, 45 and 60 degree altitudes are indicated by the blue colors from the darkest to the lightest, respectively.

### The analysis details

For the analysis of PKS 2155-304 observational data, all good quality data collected in 2004-2012 are used. The data were analyzed following the method described in Aharonian et al. (2006). A  $0.2^\circ$  circular region centered on PKS 2155-304 was used to collect the on-source events. The data have been calibrated using the standard H.E.S.S. calibration method; loose cuts were used for events selection with the background estimated using the Reflected Background method (Aharonian et al. 2006). The standard Hillas method was used to analyze the data. For all light curves the energy threshold is 200 GeV. The results were cross-checked with an independent analysis method (called Model++) with different calibration (de Naurois & Rolland 2009).

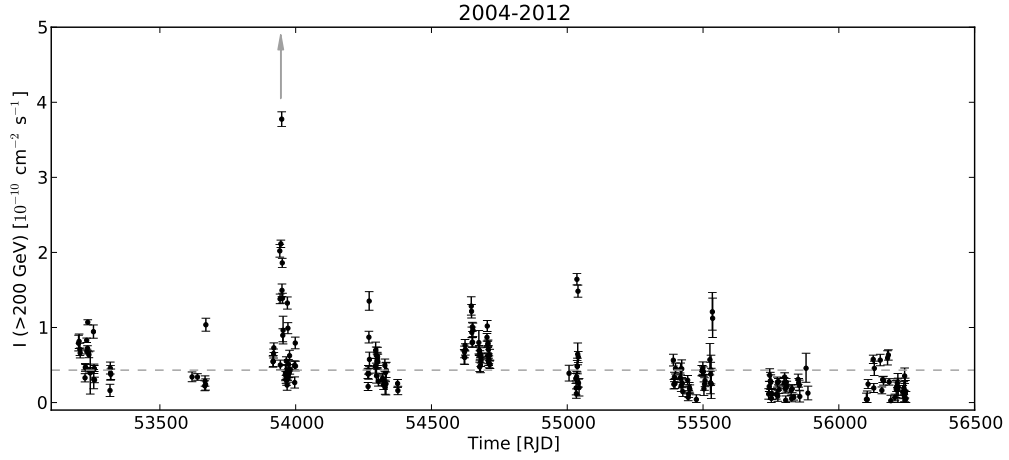


Figure 5.2: The long-term H.E.S.S. light curve, including 2004-2012 observations. The data are binned in a single night intervals. For clarity, the flare in 2006 (marked by the arrow) is not shown in the plot. During this flare the flux was about 20 times higher than in the quiescent state, see Fig. 5.3. The horizontal, dashed line shows the quiescence state of the source, as defined by Abramowski et al. (2010).

## 5.2 Light curves and variability

The long-term light curve of the source is presented in Fig. 5.2, the data are binned in a single night intervals. Night-by-night light curves for all analyzed years are presented in Fig. 5.3-5.5. For convenient night-by-night data comparison time is given in Reduced Julian Date (RJD), i.e.  $RJD \equiv JD - 2400000 \equiv MJD + 0.5$ . The energy threshold for presented light curves is 200 GeV. In the plots a dashed line shows the quiescence state of the source, as defined by Abramowski et al. (2010).

The source is characterized by the changes of the flux in year-by-year observations. Mean values of the observed fluxes in each year are collected in Table 5.1. The most exceptional outburst was observed in 2006 (Aharonian et al. 2007). The quiescence state of the source (Abramowski et al. 2010) is characterized by its mean flux level:  $I(> 200 \text{ GeV}) = 4.32 \pm 0.09_{\text{stat}} \pm 0.86_{\text{sys}} \cdot 10^{-11} \text{ s}^{-1} \text{ cm}^{-2}$ . In 2005, 2007, 2009, 2010 the source was in the quiescence state during H.E.S.S. observation campaigns. On last two years (2011-2012) the mean flux of the source is lower than the indicated quiescence level. During the other years (2004, 2008) of observations the flux of the source is above the quiescence level, but much lower than in 2006 with its an exceptional flare.

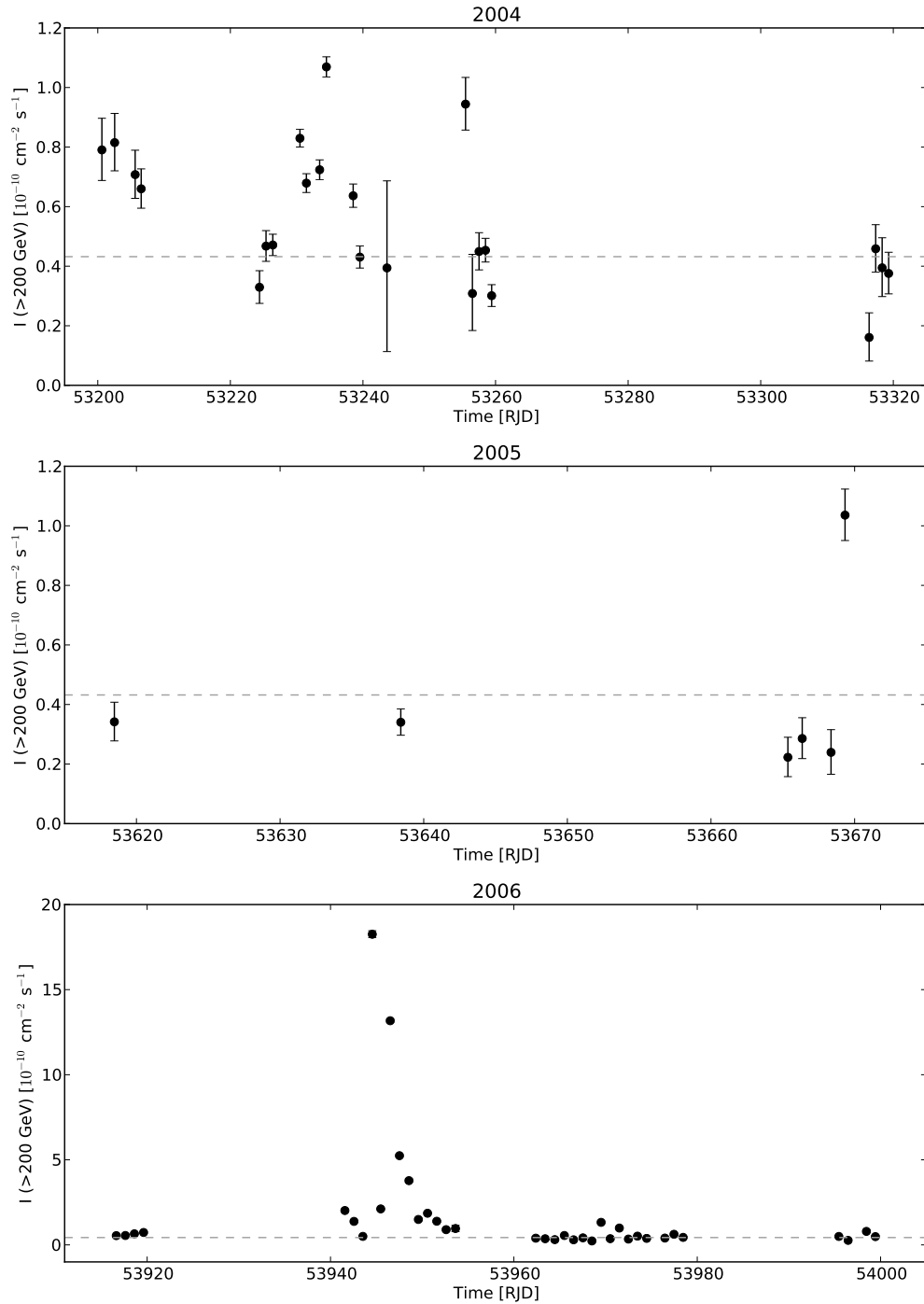


Figure 5.3: The H.E.S.S. light curves for 2004, 2005, 2006. The data are binned in a single night intervals. The horizontal, dashed line shows the quiescence state of the source, as defined by Abramowski et al. (2010).

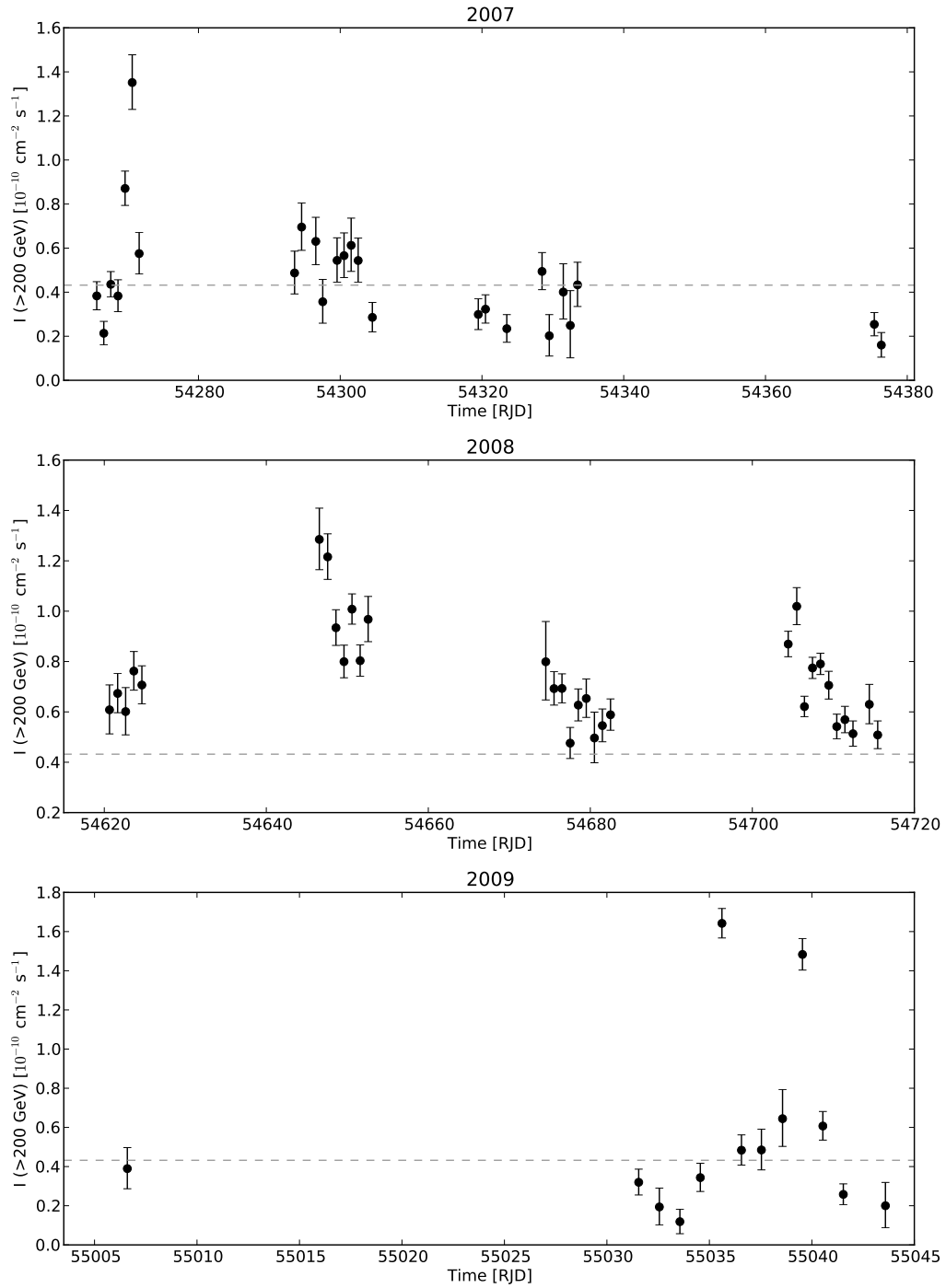


Figure 5.4: The H.E.S.S. light curves for 2007, 2008, 2009. The data are binned in a single night intervals. The horizontal, dashed line shows the quiescence state of the source, as defined by Abramowski et al. (2010).

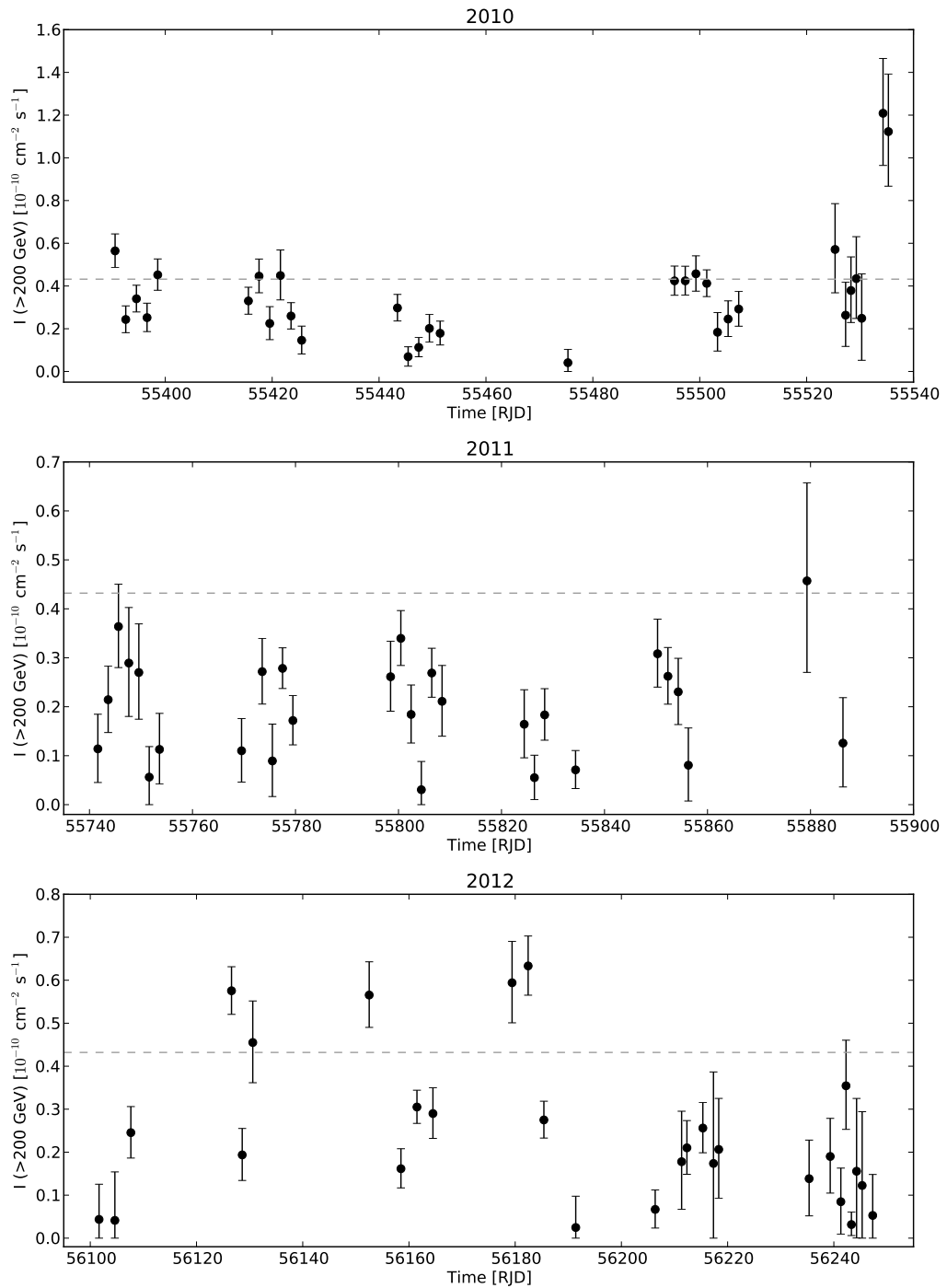


Figure 5.5: The H.E.S.S. light curves for 2010, 2011, 2012. The data are binned in a single night intervals. The horizontal, dashed line shows the quiescence state of the source, as defined by Abramowski et al. (2010).

Table 5.1: The comparison of mean year values of gamma fluxes in 2004-2012. In 2006 the data with excluded big flare are marked with a star.

Year	Mean flux [ $10^{-11} \text{ s}^{-1} \text{ cm}^{-2}$ ]	Year	Mean flux [ $10^{-11} \text{ s}^{-1} \text{ cm}^{-2}$ ]
2004	$5.59 \pm 2.26$	2008	$7.34 \pm 1.98$
2005	$4.11 \pm 2.83$	2009	$5.51 \pm 4.58$
2006	$17.71 \pm 35.27$	2010	$3.64 \pm 2.49$
2006*	$7.6 \pm 5.2$	2011	$1.99 \pm 1.05$
2007	$4.61 \pm 2.46$	2012	$2.37 \pm 1.77$

### 5.3 The relation of gamma-ray and optical fluxes

Since 2007 the ATOM observations are simultaneous with the H.E.S.S. ones and it is possible to make comparison of respective night-by-night light curves. The VHE  $\gamma$ -ray light curve of PKS 2155-304, the photon flux  $I(> 200 \text{ GeV})$ , is shown in the lower panel of Fig. 5.9. All the selected H.E.S.S. observational runs are combined to derive nightly flux values. These VHE  $\gamma$ -ray flux changes were compared with the optical fluxes in the  $B$  and  $R$  bands is given in the Fig. 5.9.

Relation between VHE gamma-rays and optical fluxes based on H.E.S.S. and ATOM data for PKS 2155-304 was investigated by Aharonian et al. (2009b). The authors found a strong indication for the correlation of the gamma and optical fluxes (the Pearson's correlation coefficient  $0.77 \leq C \leq 0.86$ ) for 12 days of simultaneous observations. The large set of "simultaneous" data collected by H.E.S.S. and ATOM during 2007-2012 allows selecting 12 new intervals of observations, similar to the ones as presented in Aharonian et al. (2009b). The details of the selected intervals are presented in Table 5.2. The Table includes the periods of observations, Pearson's correlation coefficients and the correlation slopes found by linear fits to gamma-ray flux plotted against the  $B$  band flux.

Within the whole analyzed 2007-2012 dataset, in addition to the campaign discussed in Aharonian et al. (2009b) and denoted below as 'interval D', there are 11 other intervals (hereafter 'A-C' and 'E-L') with simultaneous night-by-night observations involving more than four consecutive nights (in some cases with one-day gaps). These are all presented in different panels of Figures 5.6-5.8. The correlation coefficients and correlations slopes (for the cases of significant correlation coefficients) derived for these intervals are listed in Table 5.2. As it is shown in the figure and quantified in the table, there is no universal relation between VHE  $\gamma$ -rays and the optical flux changes on a week timescale: the fluxes seem correlated at some occasions, but uncorrelated or even anti-correlated at the other occasions. According to these results, it can conclude that short intervals of simultaneous monitoring show that there is no the general relation for such timescales.

Table 5.2: Correlation coefficients for analyzed subsets of data.

Interval	Time [RJD]	Correlation coeff.	Correlation slope
A	54294-54304	$0.35 \pm 0.26$	–
B	54646-54651	$-0.85 \pm 0.27$ (21 %)	$-2.06 \pm 0.65$
C	54674-54682	$0.32 \pm 0.21$	–
D	54704-54715	$0.75 \pm 0.15$ (7 %)	$0.97 \pm 0.28$
E	55031-55043	$0.58 \pm 0.08$ (30 %)	$2.62 \pm 1.18$
F	55390-55398	$0.15 \pm 0.25$	–
G	55417-55426	$-0.25 \pm 0.34$	–
H	55443-55451	$0.78 \pm 0.40$ (12 %)	$1.00 \pm 0.47$
I	55495-55507	$0.11 \pm 0.26$	–
J	55741-55753	$0.10 \pm 0.31$	–
K	55768-55780	$0.29 \pm 0.32$	–
L	55798-55808	$-0.15 \pm 0.28$	–

Correlation coefficients and correlations slopes derived for the analyzed intervals A-L constituting simultaneous night-by-night ATOM and H.E.S.S. observations of PKS 2155-304. A chance probability for significant correlation coefficients are indicated in the parenthesis.

The further studies includes overall large set of optical and VHE gamma-ray observations, starting with the reminder of color-magnitude diagram for this source. In the Fig. 5.10 VHE  $\gamma$ -ray data and  $B - R$  color are shown are compared with the optical flux in the  $B$  band. It should be noted here that the color-magnitude diagram for PKS 2155-304 is reveals two separate substructures, called here branches. The “lower” branch includes 2007 observations till MJD 54385, while the “upper” branch includes the rest of 2007, 2008-2012 observations. In the treated separately “upper” branch significant bluer-when-brighter trend is noticed with the Pearson’s correlation coefficient  $C_U = 0.91 \pm 0.02$ , while in “lower” one  $C_L = 0.68 \pm 0.04$ .

The color-magnitude diagram in the upper panel of Fig. 5.10 is compared with the corresponding relation of VHE gamma-ray and optical fluxes. The data from different time intervals are coded with different colors. In the whole 2007-2012 observation set, the general gamma-optical correlation is visible, with the Pearson correlation coefficient is  $C = 0.51 \pm 0.03$ . The analysis of the gamma-optical relation for the “lower” and “upper” branch shows correlation coefficients  $C_L = 0.52 \pm 0.11$  and  $C_U = 0.68 \pm 0.03$ , for the “lower” and “upper” branch, respectively.

The “lower” and “upper” branches in PKS 2155-304 are not caused by any atmospheric or instrumental effects. The color-magnitude diagram for a comparison star located 1 arcmin away from PKS 2155-304, which was always in the same raw image, does not show such feature. Also the data presented in the color-magnitude diagrams for other blazars observed during the same nights as PKS 2155-304 do not show any separate states.

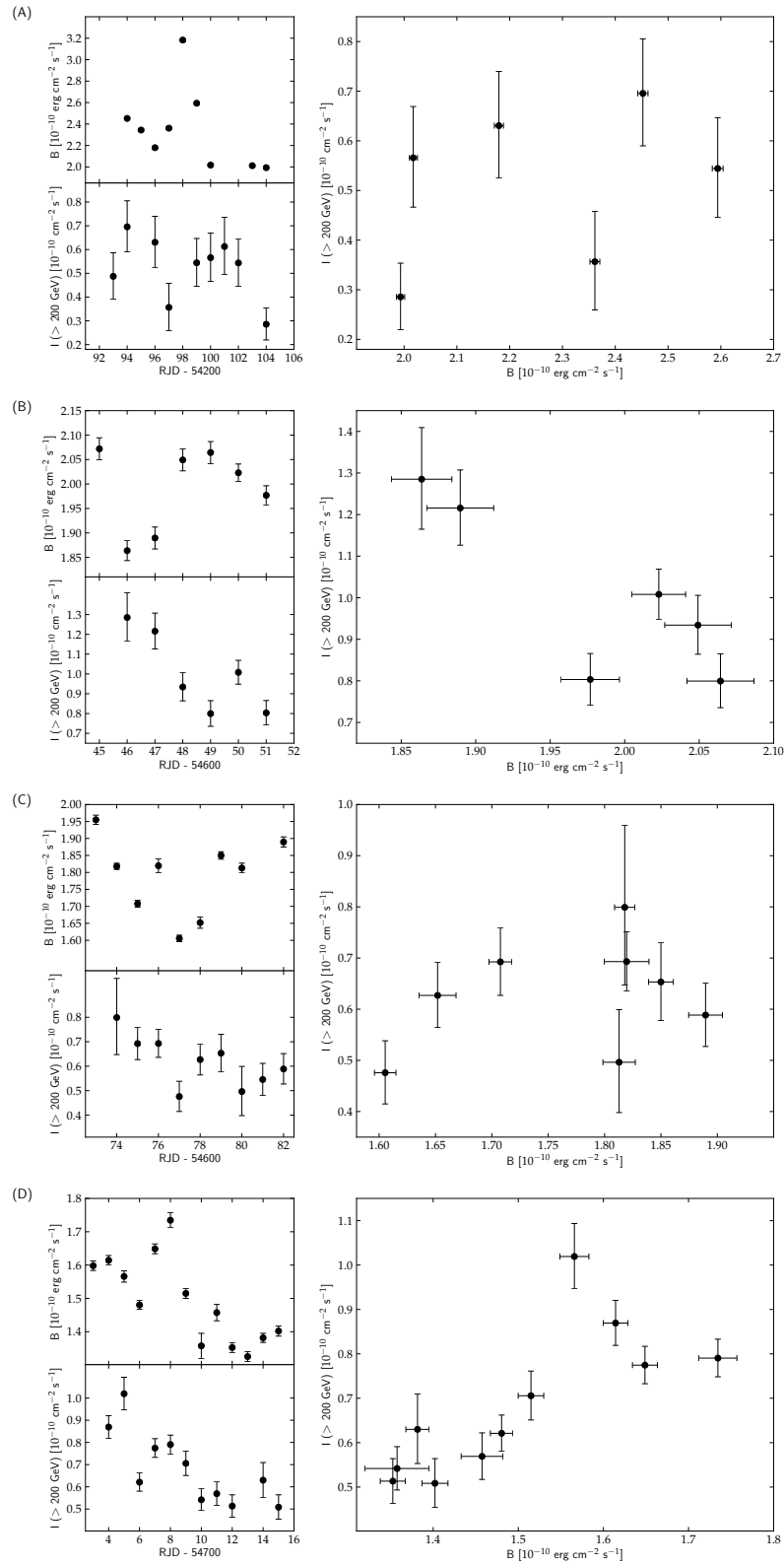


Figure 5.6: ATOM and H.E.S.S. light curves (left panels) and flux-flux diagrams (right panels) for intervals A-D (see Table 5.2).

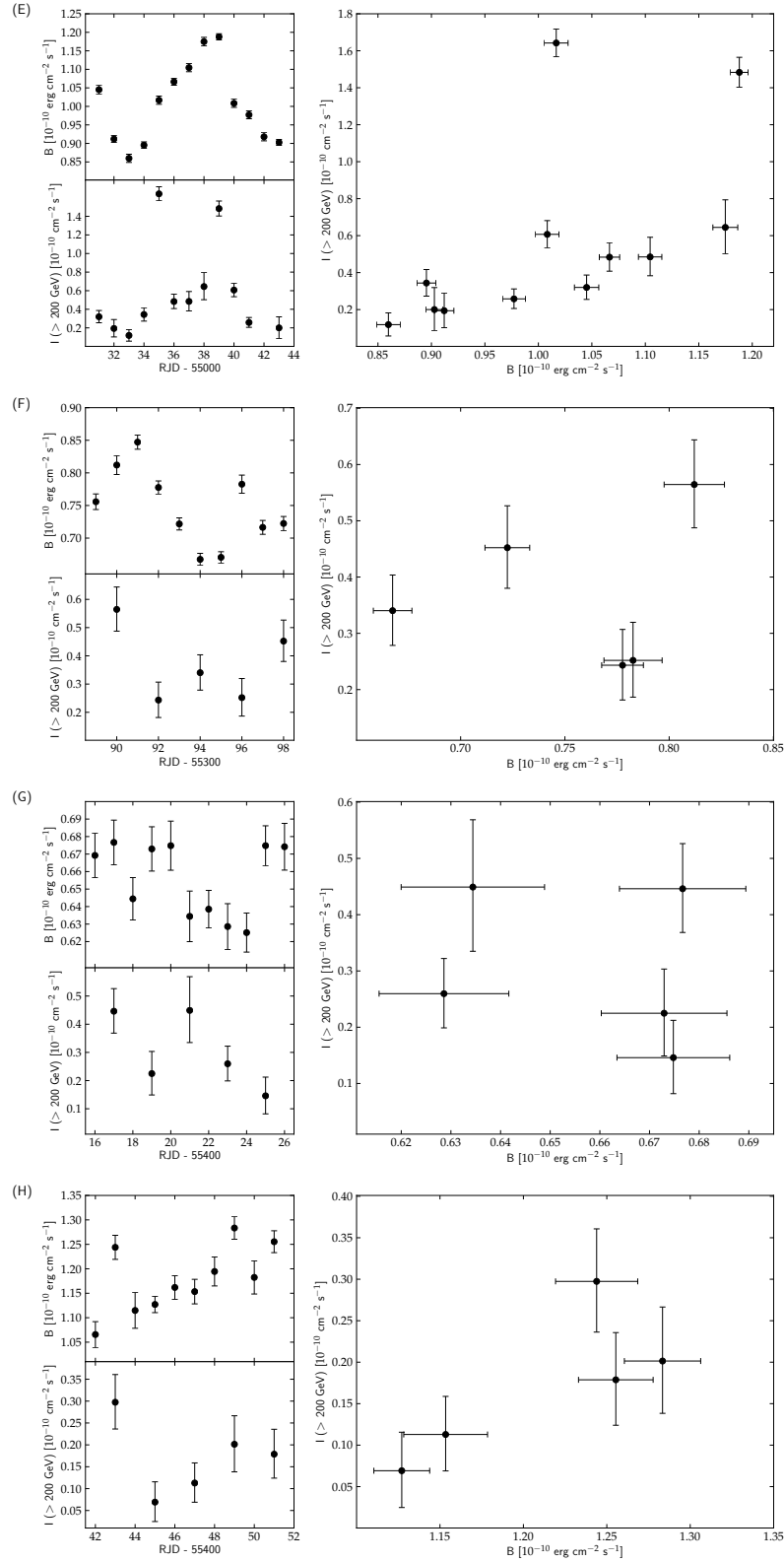


Figure 5.7: ATOM and H.E.S.S. light curves (left panels) and flux-flux diagrams (right panels) for intervals E-H (see Table 5.2).

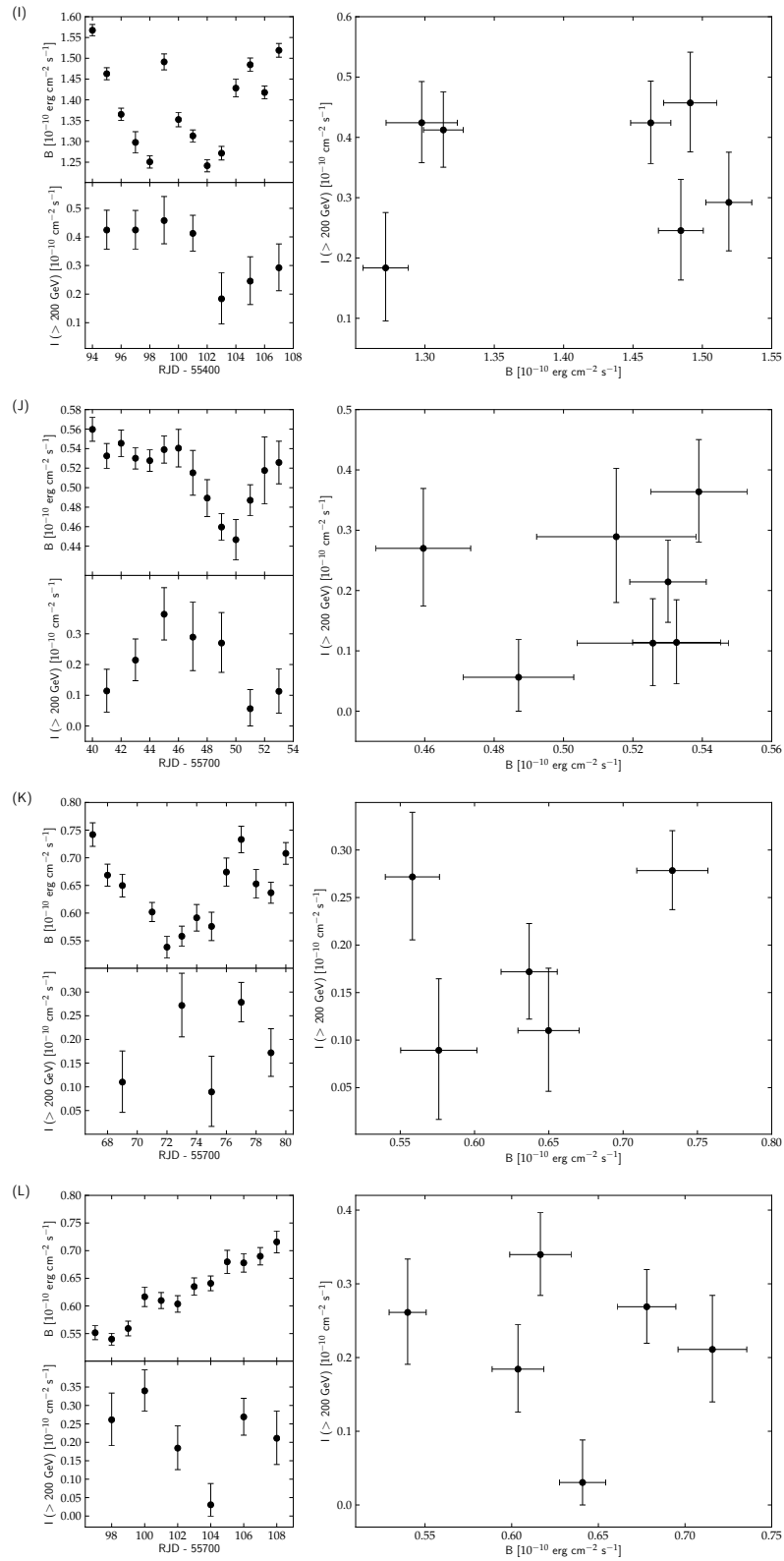


Figure 5.8: ATOM and H.E.S.S. light curves (left panels) and flux-flux diagrams (right panels) for intervals I-L (see Table 5.2).

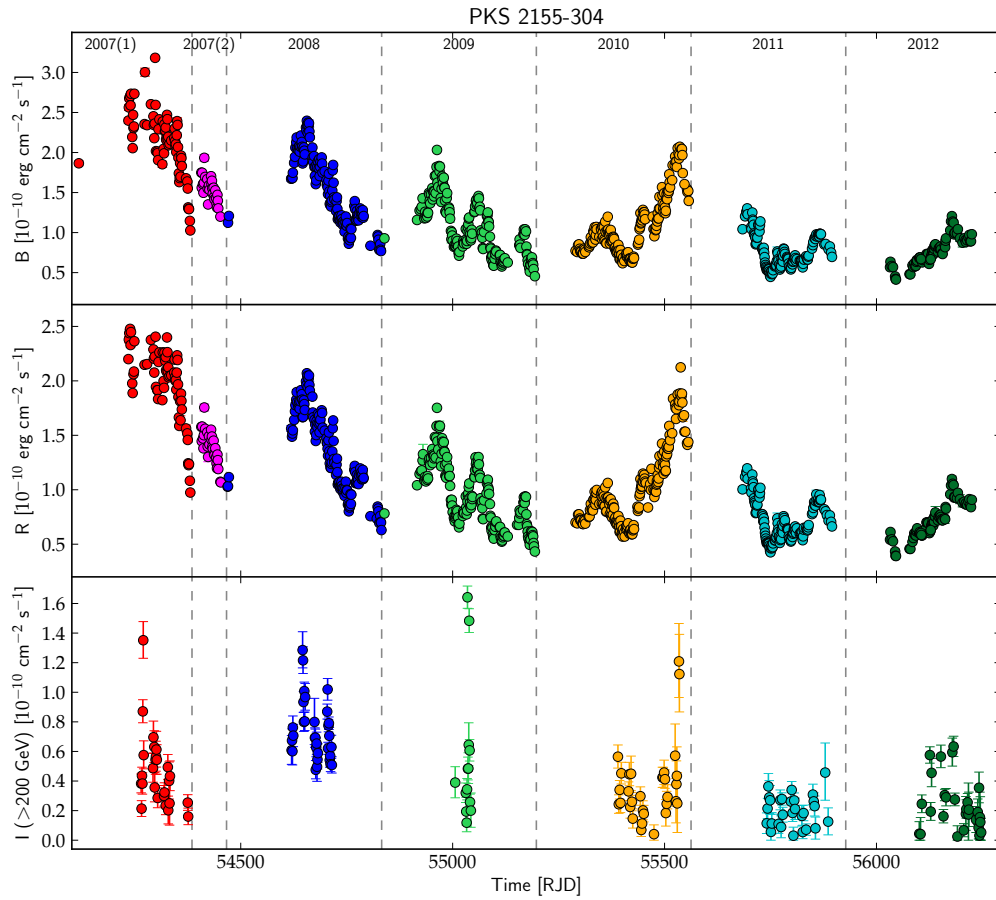


Figure 5.9: The optical (ATOM) light curves in the  $B$  and  $R$  bands and VHE  $\gamma$ -ray (H.E.S.S.) light curve of PKS 2155-304 during the period 2007-2012 (upper, middle and lower panels, respectively). The observations performed in 2007 till RJD 54385 are denoted by red symbols, in 2007 after RJD 54385 by magenta symbols, in 2008 by blue symbols, in 2009 by green symbols, in 2010 by yellow symbols, in 2011 by light blue symbols and in 2012 by dark green symbols. The optical and VHE light curves are binned into one-night intervals.

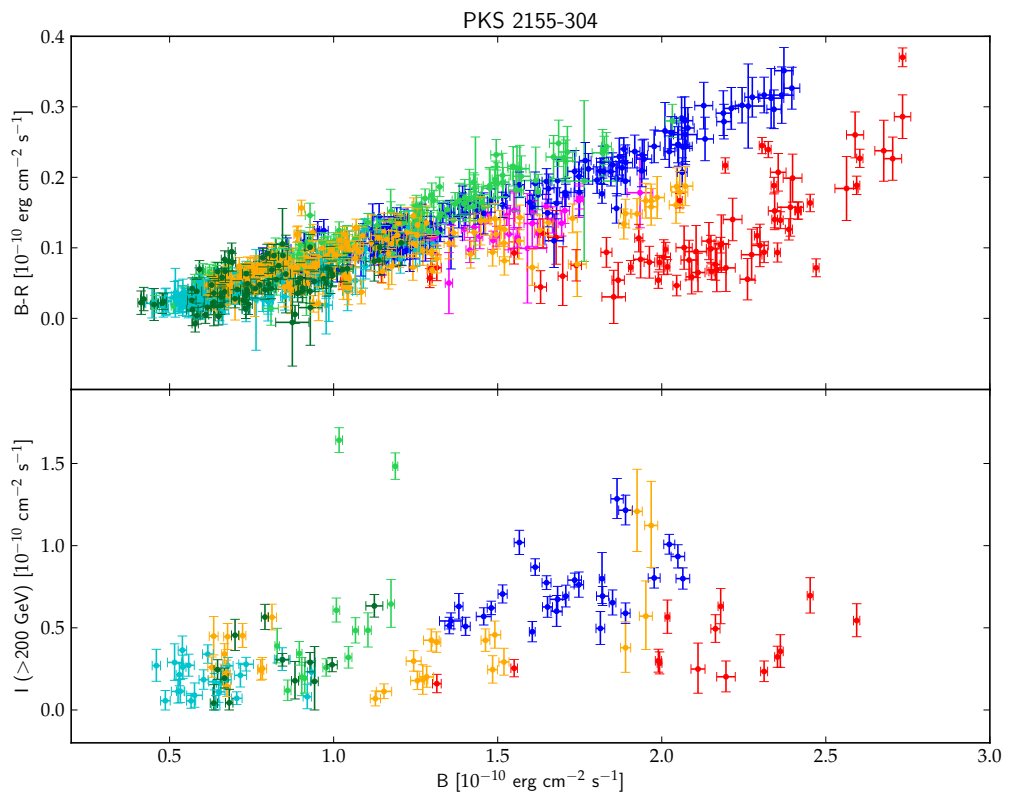


Figure 5.10:  $B-R$  color versus optical flux in  $B$  band (upper panel) and VHE  $\gamma$ -ray photon flux ( $I > 200 \text{ GeV}$ ) vs. flux in  $B$  band (lower panel) for PKS 2155-304 during the 2007-2012 period. The applied color coding is the same as in Figure 5.9.

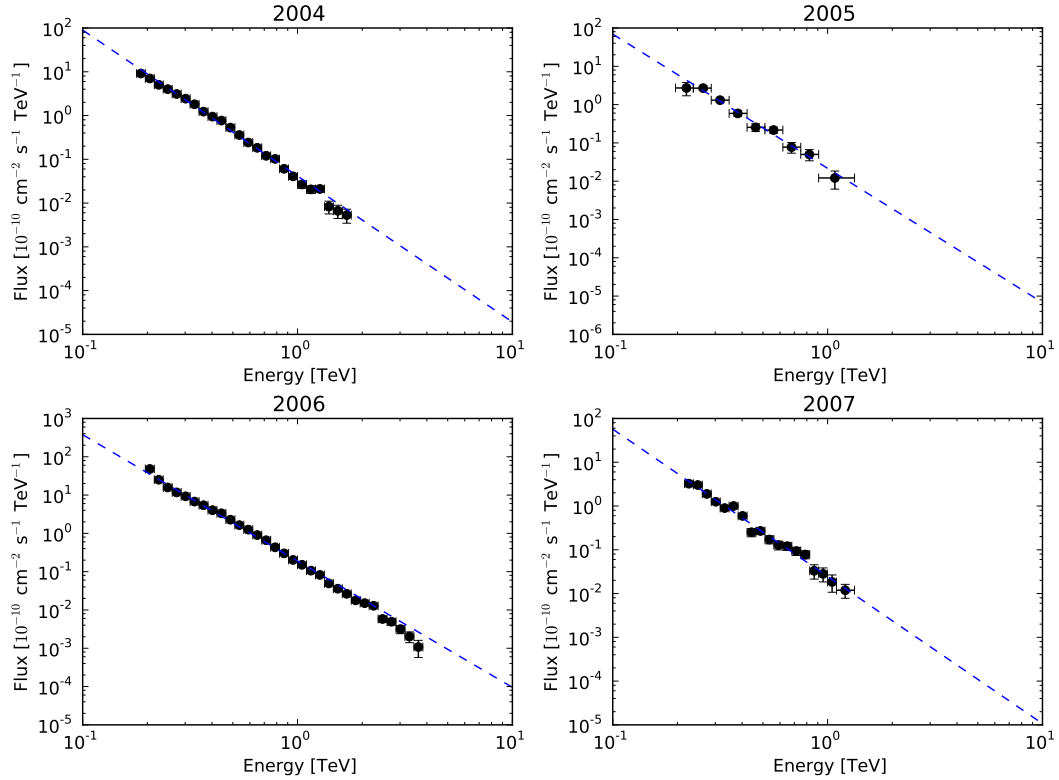


Figure 5.11: The 2004-2007 spectral for PKS 2155-304 obtained with H.E.S.S. data. The fit parameters are presented in Table 5.3.

## 5.4 Gamma-ray spectra and gamma-optical SEDs

The H.E.S.S. spectra for different years are derived using the forward-folding maximum likelihood method (Piron et al. 2001). The data are well fitted by the power-law model  $dN/dE = N_0 (E/E_0)^{-\Gamma}$ , where  $N_0$  is the normalization of the differential photon flux and  $\Gamma$  is the photon index. The VHE  $\gamma$ -ray spectra are corrected for the absorption on the extragalactic background light using the model by Domínguez et al. (2011). The fit parameters are collected in Table 5.3, while the plots are presented in Fig. 5.11 and 5.12.

No significant variability of spectral indices between different years is detected. The lowest values of spectral indices are measured for observations from 2009 and 2010, and the highest index is derived for 2005. Then VHE spectra are compared with corresponding optical spectra, obtain using ATOM data. Figure 5.13 presents the quasi-simultaneous broad-band SEDs (Spectral Energy Distribution) of PKS 2155-304 corresponding to the 2007-2012 epochs, when both ATOM and H.E.S.S. simultaneous observations were available. In the figure the VHE  $\gamma$ -ray data from H.E.S.S. and the optical data from ATOM are included.

Presented the year-averaged broad-band spectra of PKS 2155-304 during the analyzed period 2007-2012 are characterized by only moderate flux changes in the optical

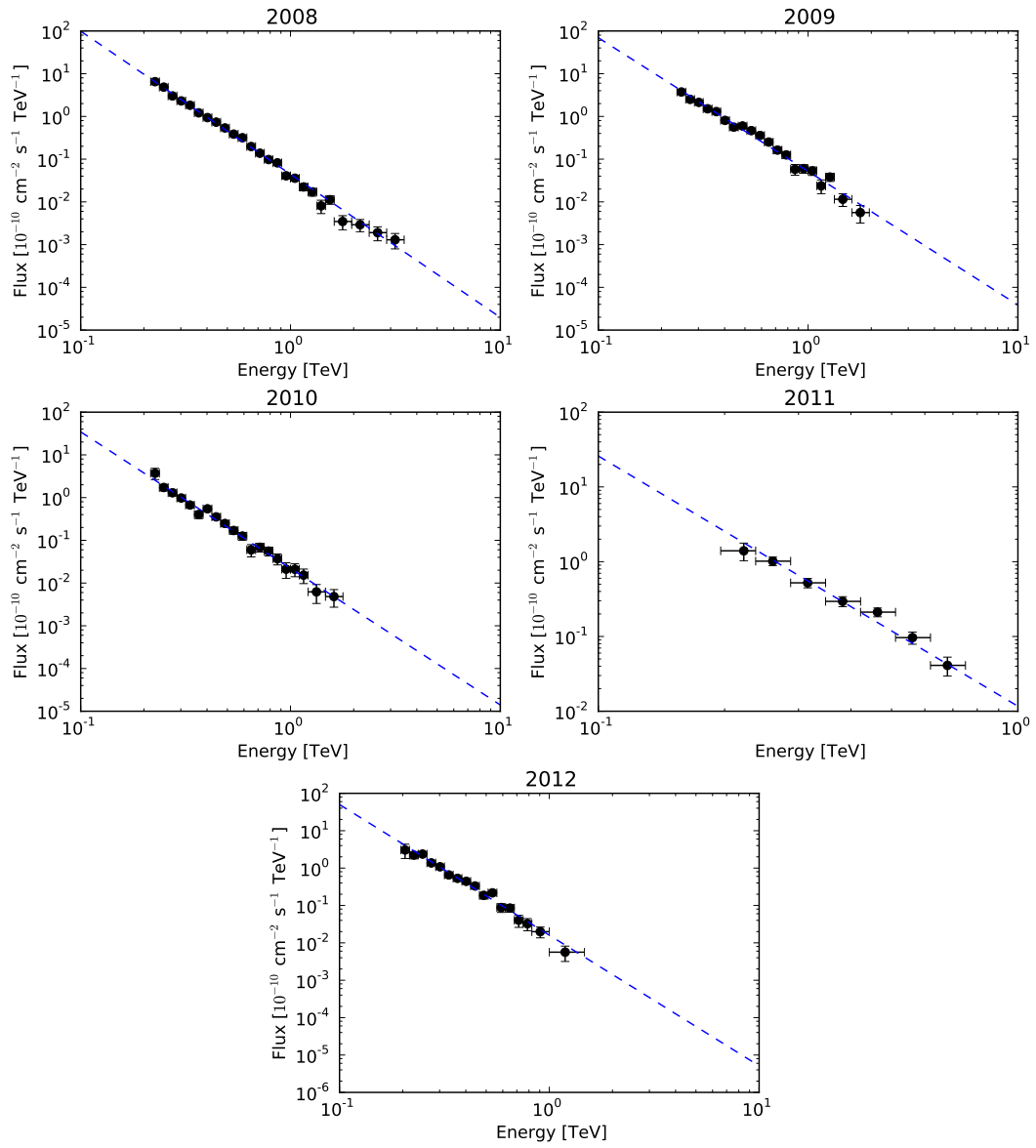


Figure 5.12: The 2008-2012 spectral for PKS 2155-304 obtained with H.E.S.S. data. The fit parameters are presented in Table 5.3.

Table 5.3: The derived model power-law fit parameters to the H.E.S.S. spectra for PKS 2155-304 in years 2004-2012.

Year	$\Gamma$	$N_0$ [ $10^{-12} \text{ TeV}^{-1} \text{ s}^{-1} \text{ cm}^{-2}$ ]
2004	$3.334 \pm 0.028$	$4.15 \pm 0.13$
2005	$3.505 \pm 0.163$	$2.17 \pm 0.38$
2006	$3.298 \pm 0.010$	$18.96 \pm 0.18$
2007	$3.400 \pm 0.085$	$2.48 \pm 0.09$
2008	$3.352 \pm 0.036$	$4.30 \pm 0.07$
2009	$3.116 \pm 0.058$	$5.20 \pm 0.18$
2010	$3.196 \pm 0.088$	$2.20 \pm 0.19$
2011	$3.346 \pm 0.128$	$1.17 \pm 0.17$
2012	$3.349 \pm 0.046$	$1.60 \pm 0.07$

and VHE  $\gamma$ -ray bands. In the optical band the SED points form 4 states: 2007 with the highest flux, 2008 with flux below the 2007 flux level, then the flux in 2009 is at the same flux level as observed in 2010, and the lowest optical flux level is for 2011 and 2012 observations. In the VHE  $\gamma$ -ray regime the uncertainties in the derived values of the photon indices and fluxes are relatively large, precluding therefore any definitive statements about spectral changes and differences between the selected years.

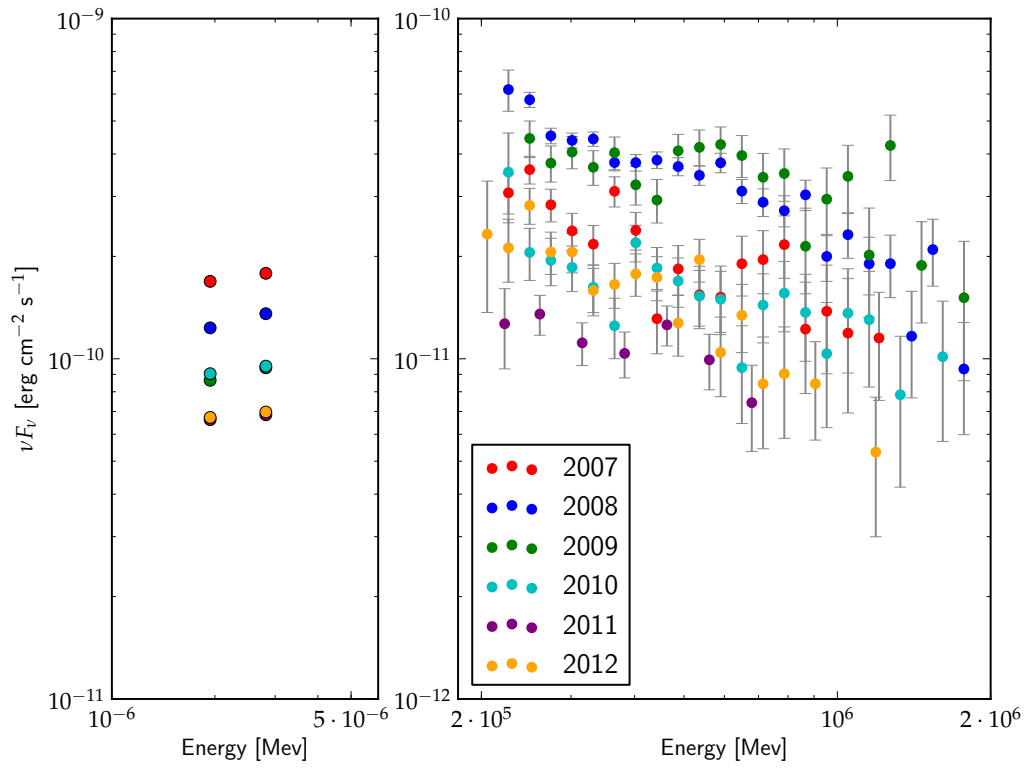


Figure 5.13: Two spectral ranges of SED of PKS 2155-304 for the years 2007-2012 (different colors are used for selected years), constructed using quasi-simultaneous data collected by ATOM (in *B* and *R* band) and H.E.S.S. (left and right panel, respectively).

## Discussion and Summary

### 6.1 Optical monitoring of the blazars

The optical monitoring presented in this thesis provided a unique set of optical data, including 6 years of observations of 30 BL Lac type blazars (LBL, IBL and HBL types). Such a large sample of long-term, systematic observations was not earlier analyzed in the literature. It should be noted here that the analyzed sample was not selected based on some physical criterion, but includes only BL Lacs, selected for the monitoring by ATOM.

Studies of color-magnitude diagrams for the blazars show different type of behavior, but with a general preference for the bluer-when-brighter trend. In the case of 14 from the sample exhibit a significant bluer-when-brighter correlation with the Pearson's correlation coefficient larger than 0.5. These are: 1ES 0323+022, 1ES 0347-121, 1ES 1218+304, AP Librae, BL Lacertae, Markarian 421, Markarian 501, PKS 2005-489, RGB J0152+017, SHBL J032541.0-164618, SHBL J101015.9-311908 and W Comae. The bluer-when-brighter relation was earlier discussed in the literature, commonly for BL Lacs (e.g. Fan et al. 1998; Massaro et al. 1998; Clements & Carini 2001; Vagnetti et al. 2003; Wu et al. 2005, 2007; Rani et al. 2010). This trend is usually explained as a shift to higher peak frequencies during a flare (e.g. Pian et al. 1998; Takahashi et al. 1999; Massaro et al. 1998; Giommi et al. 2012), but there is so far no clear understanding as to why such a shift should occur.

A negative correlation is found only in two sources: PG 1553+113 and PKS 1424+240, but the correlation is not significant. This opposite trend was also widely discussed in the literature (e.g. Miller 1981; Clements & Carini 2001; Osterman Meyer et al. 2008, 2009) and is usually attributed to FSRQs.

In the case of several color-magnitude diagrams presented in this thesis, the plots show complex structures. Often, the total color-magnitude diagram shows of separate individual substructures, revealing varying physical conditions in the emission region.

An interesting example is PKS 0301-243. The analysis of all available observations does not indicate either the bluer-when-brighter or the redder-when-brighter chromatism. However for selected the two selected periods (see Fig. 6.1), the subsequent observations form two separate branches with a 0.4 mag gap and a clear bluer-when-brighter trend visible in each branch. Similar behavior with clear color-magnitude trends in limited periods of observations can be found in other objects presented in this thesis. The example is RGB J0152+017, which in the color-magnitude diagram form two substructures, which correspond to the changes of chromatism in the object, from redder-when-brighter to bluer-when-brighter.

Another interesting example is PKS 2005-489 (Fig. 6.2). In this case the bluer-when-brighter relation is clearly detected in all observations presented here. A year-by-year analysis of the color behavior reveals substructures, in which the color-magnitude chromatism holds, but linear fits to the data points in the substructures of the color-magnitude diagrams are characterized by slightly different slopes. For example, for the brightest outburst the correlation coefficient is larger ( $C = 0.94 \pm 0.01$ ) than in the case of the whole data set ( $C = 0.76 \pm 0.01$ ).

A lack of an observed bluer-when-brighter trend in blazars can be accounted for the real absence of the bluer-when-brighter chromatism in these objects. Alternatively, it is possible that the bluer-when-brighter trend is hidden in the substructures in the color-magnitude plot, as e.g. in PKS 0301-243. In such cases further detailed studies of observations at other wavelengths are required.

A qualitative analysis of the color-magnitude diagram in terms of variability does not show any general relation. It seems that for most of objects with weakly varying flux (with  $\sim 0.15$  mag variation) no clear color-magnitude relation is present. A significant part of the sample with optical variations in a range of  $\sim 0.6$ -1.2 mag shows a strong bluer-when-brighter correlation. However for prominent outbursts (with amplitude for at least 1.0 mag) the trend is not always present, as in the case of PKS 0537-441 shown in Fig. 6.3. The trend is visible in PKS 2005-489 even though it is in the flaring state with the amplitude  $> 1$  mag.

A comparison of the optical luminosities of the ATOM blazars and the color-magnitude correlation coefficients gives a constraint on this relation. The bluer-when-brighter relation is observed only for the low-power BL Lac blazars with the optical  $R$  band luminosity below  $\sim 10^{45}$  erg s $^{-1}$  (Fig. 4.23). Above this luminosity there are no sources with a significant bluer-when-brighter correlation. Such a constraint was not earlier noted in the literature.

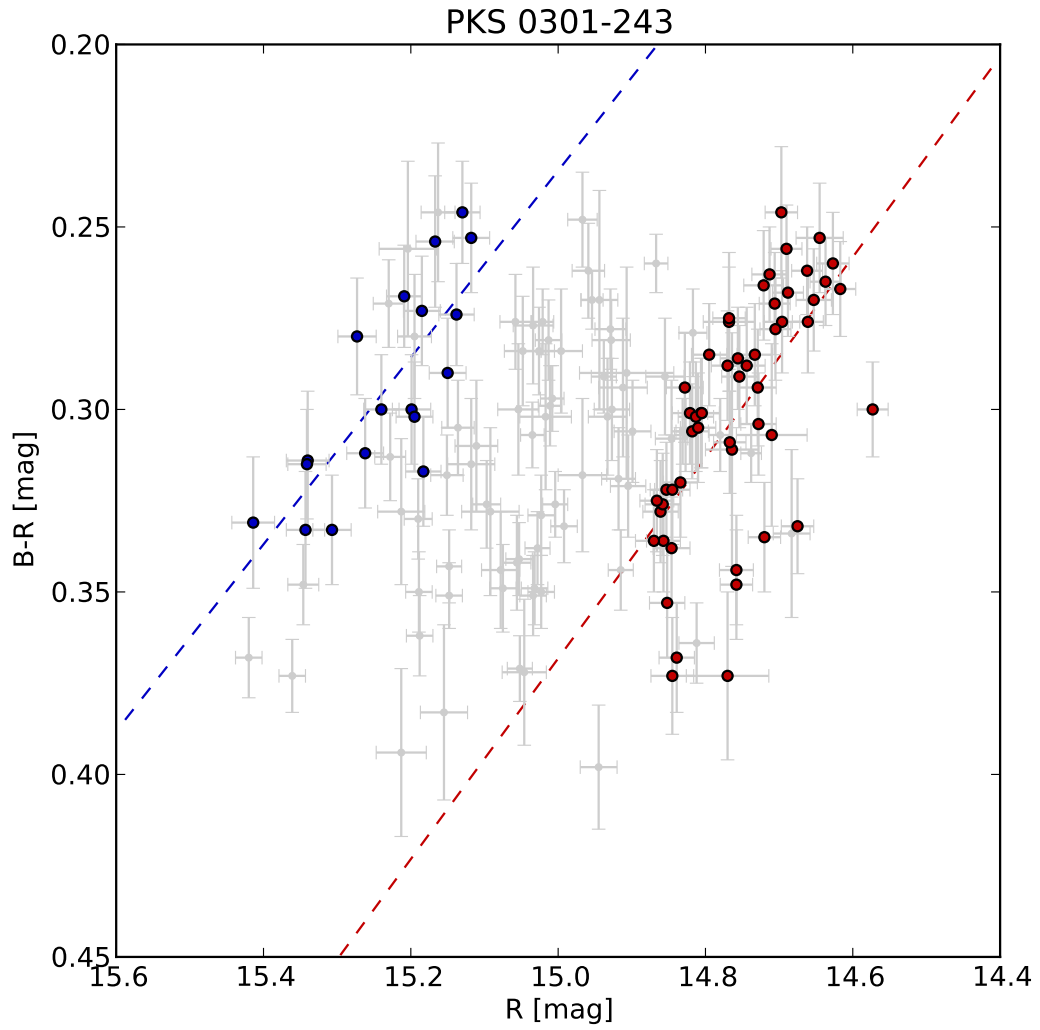


Figure 6.1: The  $B - R$  color as a function of the  $R$ -band magnitude for PKS 0301-243. The red and blue points show the selected intervals of observations. The red and blue, dashed lines show correlation slopes.

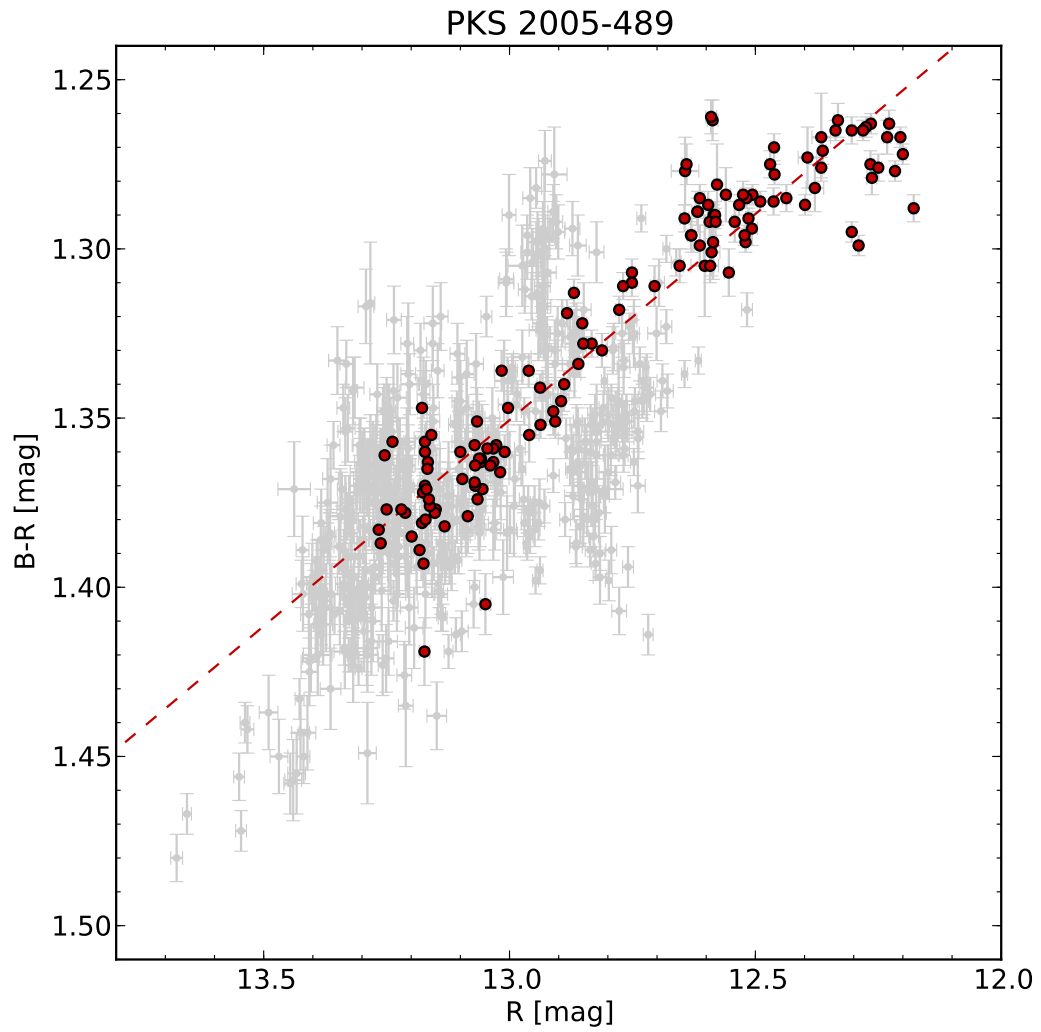


Figure 6.2: The  $B - R$  color indices as functions of the  $R$ -band magnitude for PKS 2005-489. The red points show the selected interval of observations. The red dashed line shows correlation slope.

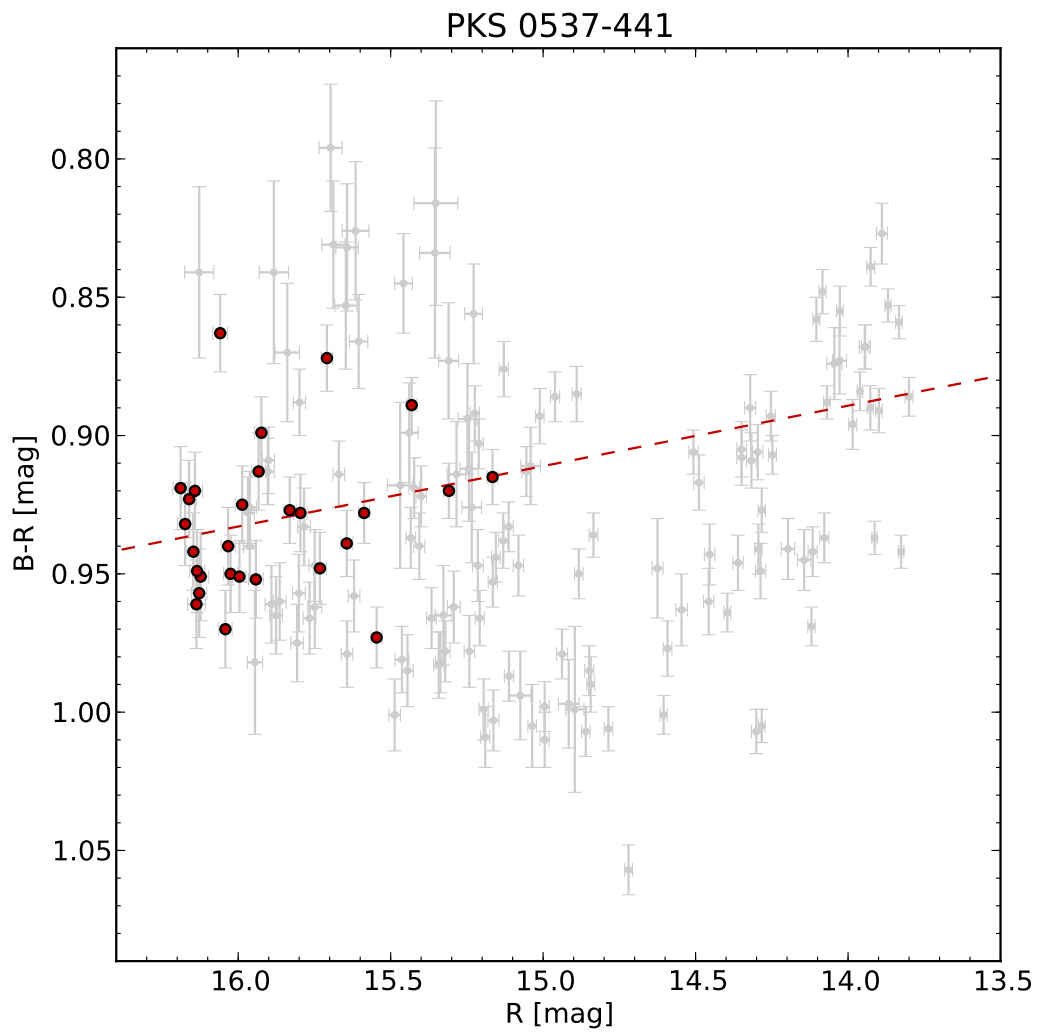


Figure 6.3: The  $B - R$  color index as a function of the  $R$ -band magnitude for PKS 0537-441. The red points show the selected interval of observations and the red dashed line shows the correlation slope.

## 6.2 Multiwavelength properties of the blazars

The analysis of the ATOM blazars and comparison of radio, optical and gamma-ray luminosities strongly suggest that more luminous objects in the optical band are also more luminous at radio and high energy gamma-ray wavelengths. The strong correlations, with the Pearson's correlation coefficient  $\sim 0.9$ , between quasi-simultaneous observations suggest the existence of a direct coupling between the involved emission mechanisms, possibly operating in the same region of the relativistic jet. Unfortunately, such a comparison of luminosities including very high energy gamma-ray observations (e.g. from H.E.S.S.) was not possible due to a small number of simultaneous observations available only a for few sources from the sample.

The analysis includes all the subclasses (LBL, IBL, HBL) of the BL Lac type objects, and the comparison of the luminosities show that almost every object follows the "blazar sequence". The outliers are: PG 1553+113, a high-redshift, HBL type source, which is characterized by low radio power and a very flat GeV spectral index (as expected for HBL) but at the same time with a relatively high luminosity in the optical and GeV range, and also AP Librae, LBL object. This deviation can suggest a wrong classification or redshift determination for these two blazars or their different physical properties in them.

## 6.3 Observations of PKS 2155-304

PKS 2155-304 is one of the best monitored sources among the H.E.S.S. targets, it is also often a target of MWL campaigns (see e.g. Aharonian et al. 2009a,b; Abramowski et al. 2012). The connection between emission at different frequencies for this source was widely studied and analyzed in the context of multiwavelength variability in blazars. Observations of objects in the VHE range with modern-generation Cherenkov telescopes (H.E.S.S.II, MAGIC-II, VERITAS) revealed or at least suggested a positive correlation between the optical and VHE  $\gamma$ -ray emission for several objects (e.g. Abdo et al. 2011a,b; Aharonian et al. 2009b).

The longterm monitoring in the VHE gamma-ray and optical band and the analysis of these observations, presented in this thesis, reveal different spectral states in the case of PKS 2155-304. In the color-magnitude diagram two branches are visible, called the "lower" and the "upper" branch. The lower one is characterized by steeper optical spectrum occurring in the phase of the brightest optical flaring in the blazar in 2007. For all collected data, there exists a significant VHE gamma-ray – optical correlation with  $C = 0.51 \pm 0.03$ , but the relation becomes much more significant for the "upper branch" where  $C_U = 0.67 \pm 0.03$ , while in the lower branch  $C_L = 0.52 \pm 0.11$ .

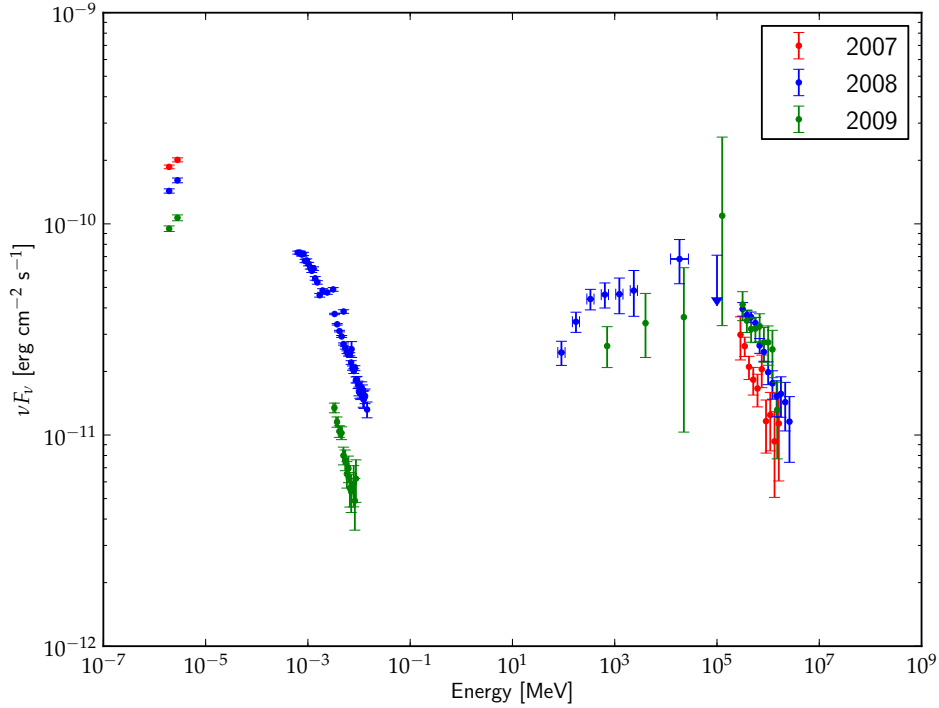


Figure 6.4: Average broad-band SEDs of PKS 2155-304 for the years 2007, 2008, and 2009 (red, blue and green symbols, respectively), constructed using quasi-simultaneous data from ATOM, RXTE, Swift, Fermi-LAT and H.E.S.S..

These two different spectral states are also visible in other ranges (HE gamma-rays and X-rays), which is presented for 2007-2009 observations of PKS 2155-304 by the author of this dissertation (Abramowski et al., 2013, in prep.) (Fig. 6.4).

The existing multiwavelength blazar observations show that even with the sets of simultaneous observations, the emission processes are still not well understood, especially the broad-band variability of the TeV-emitting objects. For such objects a simple homogeneous emission model seems to be insufficient. Therefore, multi-zone or multi-component emission models are widely discussed now. The reasons for the formation of numerous and/or compact zones of the enhanced energy dissipation are uncertain, but relativistic reconnection events and MHD instabilities operating close to the jet base, generating particle beams or compact blobs moving relativistically within the outflow, are the widely invoked possibilities. Such possibilities were explored in e.g. the inhomogeneous jet model proposed by Boutelier et al. (2008), multi-blob synchrotron self-Compton model by Lenain et al. (2008), jets-in-a-jet scenario by Giannios et al. (2009), or mini jets scenario suggested by Nalewajko et al. (2011).

## Outlook

The results obtained in this thesis suggest possible directions for further investigations. The analysis of color-magnitude relations for ATOM blazars allowed identifying several substructures in these plots. As in the case of PKS 2155-304, such substructures require further multiwavelength studies, including radio, optical, HE gamma-rays and possible infrared VHE gamma-rays observations, to get deeper insight into the considered physical processes. The blazars recommended for further, detailed studies are:

- **AO 0335+16** – the blazar with highly variable flux and optical color, with both the bluer-when-brighter and redder-when-brighter substructures in the color-magnitude plot;
- **PKS 0301-243** – the object without a general color-magnitude relation, but with at least two substructures showing the bluer-when-brighter chromatism in the color-magnitude (mentioned in Sect. 6.1);
- **1ES 0414-00.9** – the source with data points in color-magnitude plot divided into two separate parts;
- **PKS 0537-441** – the object with complex color magnitude plot, including substructures with the bluer-when-brighter and redder-when-brighter relation;
- **PKS 2005-489** – the blazar, which is well monitored not only by ATOM, but also in the other bands;
- **PG 1553+113** – the high-redshift, HBL type source, which is characterized by low radio power and very flat spectral index (as expected for HBLs) but at the same time with a relatively high luminosity in the optical and GeV range.

PKS 2155-304 is a particularly interesting object, which has been monitored by H.E.S.S. since 2004 in each year. These observations will be continued in 2013, as a part of longterm H.E.S.S.-ATOM monitoring and also PKS 2155-304 will be a target of a dedicated, multiwavelength campaign. The latter project includes simultaneous observations by ATOM, SCUBA-2, NuStar, Fermi-LAT and H.E.S.S.II, what will allow to collect a unique set of simultaneous observations. The author of the dissertation is one of the PIs of this proposal.

# **Appendices**

## Color coding in color-magnitude diagrams

In Section 4 the color-magnitude diagrams for the ATOM blazars are presented. Due to ATOM data policy it was not possible to include light curves with exact observation times in this dissertation. Thus, to indicate the time evolution of the presented objects in the color-magnitude plots, different colors (color coding) are applied. The whole time span of observations considered is linearly represented by the rainbow color scale extending from dark blue, through green, yellow, orange to red (Fig. A.1).

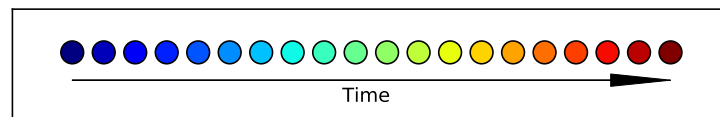


Figure A.1: The color scale used in color-magnitude diagrams to encode the time evolution of the source.

The coding system is presented in a schematic way presented in Fig. A.2. In the figure three light curves corresponding to optical observations of PKS 2155-304 are shown. The upper part of panel A includes all observations between 2007-2012. The upper part of panel B includes the same light curve without the initial and the final observations. In the case of the upper part of panel C the middle observations have been rejected from the data set. In the bottom parts of all panels the color-magnitude diagrams corresponding to the light curves are presented. This schematic view shows a way how to decode the time evolution of color-magnitude diagrams, and this method is useful to identify substructures of subsequent data points in these plots: each real of substructure in time is plotted with data points coded with a similar color. The plots in Fig. A.2 show how the color coding reacts on changing the time range of the light curve.

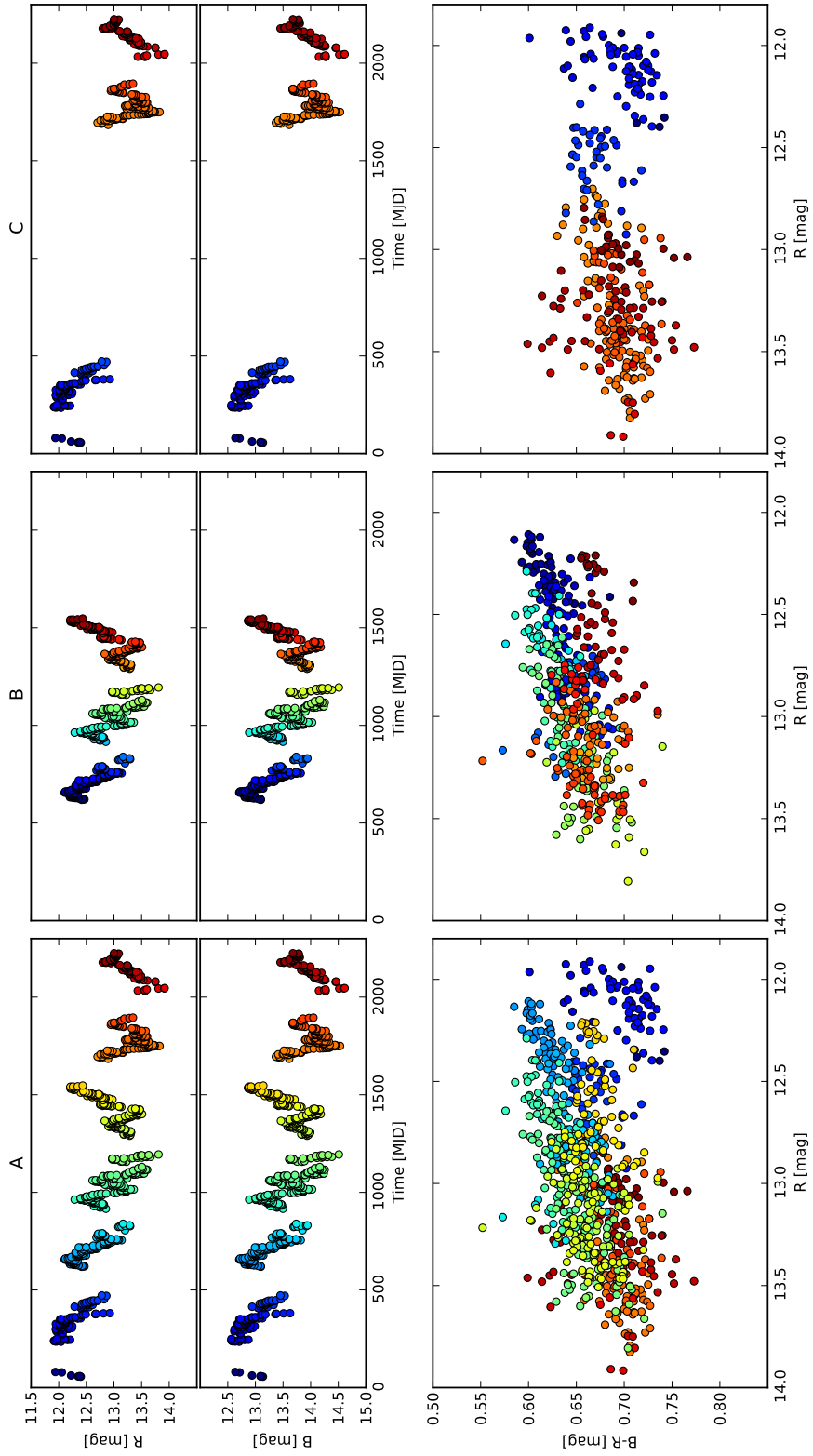


Figure A.2: Example of the color coding applied in this work in the case of color-magnitude diagrams. Three panels present real light curve and corresponding color-magnitude diagram for PKS 2155-304. The panel A shows optical light curve and color-magnitude diagram for whole period of observations. The panel B includes only the data of the middle part of the light curve, and the panel C only the initial and final part of the analyzed light curve.

## Error estimation for the Pearson's correlation coefficient

To estimate an uncertainty of the Pearson's correlation coefficient one can use the Monte Carlo approach (Sanchez 2010). Here it is assumed that we have a set of points  $A = \{(x_i, y_i)\}$  and each of the point has its own corresponding uncertainty values  $(\Delta x_i, \Delta y_i)$ . In the first step, for each point new coordinates are drawn randomly according to the normal distribution for which the mean is set to  $x_i$  (or  $y_i$ ) and the standard deviation to  $\Delta x_i$  (or  $\Delta y_i$ ). It results in a new set of points  $A'$  and its Pearson's correlations coefficient is  $C'$ .

Repeating the procedure  $N$  times gives a set of Pearson's coefficients  $\{C'_n\}$ . If  $N$  is large enough a histogram of the  $\{C'_n\}$  should have roughly a Gaussian shape. However due to fact that Pearson's coefficient has only values in range  $[-1, 1]$  it is good to apply a Fisher transformation (see below) on each of the  $C'$  value before making the histogram. An example of such histogram is shown in Figure B.1.

To find the uncertainty of the Pearson's coefficient a Gaussian function is fitted to the histogram. The standard deviation of this fit can be used as an estimation of the Pearson's coefficient uncertainty of the original set of points  $A$ . The value found by fitting should be transformed back by the reverse Fisher transformation.

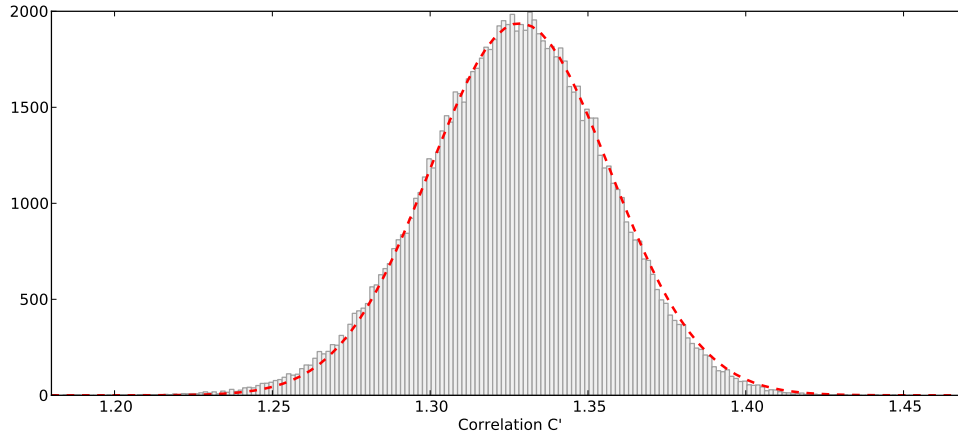


Figure B.1: A histogram of the Monte Carlo generated set of  $10^5$  Pearson's correlation coefficients  $\{C'\}$ . The red line shows the Gaussian fit. The  $C'$  values were transformed with the Fisher transformation. The reverse Fisher transformation of the fit gives the Pearson's correlation coefficient equal to 0.87 and its error is estimated to 0.03.

### Fisher transformation

The Fisher transformation allows to represent values which spans from  $[-1, 1]$  in range of  $(-\infty, \infty)$ . It is defined as follows:

$$z = \frac{1}{2} \ln \left( \frac{1+r}{1-r} \right) = \operatorname{atanh} r, \quad (\text{B.1})$$

and the reverse one:

$$r = \frac{\exp(2z) - 1}{\exp(2z) + 1}. \quad (\text{B.2})$$

## Optical spectral index

The mean optical color of blazar corresponds to the optical spectral index.  $B - R$  color can be expressed as:

$$B - R = -2.5(\log_{10}(a_{BR}) - \log_{10}(f_{B0}/f_{R0})), \quad (\text{C.1})$$

where  $a_{BR}$  is the slope of the best-fit regression line of  $B$ -flux and  $R$ -flux diagram,  $f_{B0}$  and  $f_{R0}$  are the fluxes at zero magnitude in  $B$  and  $R$  bands, respectively. For the power-law spectrum the spectral index  $\alpha_{BR}$  between the  $B$  and  $R$  bands can be calculated as:

$$\alpha_{BR} = \frac{\log_{10}(a_{BR})}{\log_{10}(v_B/v_R)}, \quad (\text{C.2})$$

where  $v_B$  and  $v_R$  are the effective frequencies of  $B$  and  $R$  bands. Then, using C.1 and C.2, a relation between optical spectral index and mean  $B - R$  color is given:

$$\alpha_{BR} = \frac{\log_{10}(f_{B0}/f_{R0}) - 0.4(B - R)}{\log_{10}(v_B/v_R)}. \quad (\text{C.3})$$

For example:

- for  $B - R = 0.5$      $\alpha = -0.35$ ,
- for  $B - R = 1.0$      $\alpha = -1.53$ ,
- for  $B - R = 1.5$      $\alpha = -2.70$ .

## Proposal description

The project includes joint multiwavelength observations of PKS 2155-304 in VHE  $\gamma$ -rays, complemented by simultaneous optical and HE  $\gamma$ -ray observations of the source with ATOM, ROTSE, and *Fermi*-LAT. The main goals of the campaign are: (1) to enable a better understanding of quiescence states in blazars, (2) to improve constraints on the duty cycle and the long-term variability in PKS 2155-304 within the VHE range, (3) to extend multiwavelength studies of the source by means of the unbiased cross-band correlation analysis, and finally (4) to monitor the  $\gamma$ -ray activity of PKS 2155-304 in a regular way, looking for rare but spectacular flaring events.

The performed observations of PKS 2155–304 included monitoring of the object in 2012 every 2nd night for 1 hour around culmination, through the entire visibility window. This gives 7 monthly shifts with 6 observations each, and amounts to a total of 42 hours exposure. The exposure time of 1 h per night is required for the detection of the source at the sufficient significance level ( $7-10\sigma$ ) during the quiescence state, and for a proper spectral characterization of the detected flux. The two-day-long time interval separating the subsequent pointing is dictated by the integration time needed to achieve a significant detection of the target with *Fermi*-LAT. In the case when not all of the four H.E.S.S. telescopes are operational, the exposure time per pointings should be increased to achieve the desired significance of the detection (e.g. 1.5 h for 3 telescopes, 2 h for 2 telescopes). Also, the target of opportunity (ToO) observations were proposed in the case of a high flux level of the source ( $> 1$  Crab)<sup>1</sup>. The observation within a given night should be extended until the source is below a zenith angle of  $45^\circ$ . In the case of a particularly strong outburst ( $> 2$  Crab), follow up observations for the next 3-4 days should be triggered.

---

<sup>1</sup>Crab is a unit of flux frequently use in VHE gamma-ray astronomy and corresponds to the value of  $(2.28 \pm 0.08) \cdot 10^{-11} \text{ cm}^{-2} \text{ s}^{-1}$  (Aharonian et al. 2006)

# Bibliography

- Abdo, A. A., Ackermann, M., Ajello, M., et al. 2011a, ApJ, 727, 129
- Abdo, A. A., Ackermann, M., Ajello, M., et al. 2011b, ApJ, 736, 131
- Abramowski, A., Acero, F., Aharonian, F., et al. 2012, A&A, 539, A149
- Abramowski, A., Acero, F., Aharonian, F., et al. 2010, A&A, 520, A83
- Aharonian, F., Akhperjanian, A. G., Anton, G., et al. 2009a, A&A, 502, 749
- Aharonian, F., Akhperjanian, A. G., Anton, G., et al. 2009b, ApJ, 696, L150
- Aharonian, F., Akhperjanian, A. G., Aye, K.-M., et al. 2005a, A&A, 430, 865
- Aharonian, F., Akhperjanian, A. G., Barrio, J. A., et al. 1999, A&A, 349, 29
- Aharonian, F., Akhperjanian, A. G., Bazer-Bachi, A. R., et al. 2007, ApJ, 664, L71
- Aharonian, F., Akhperjanian, A. G., Bazer-Bachi, A. R., et al. 2006, A&A, 457, 899
- Aharonian, F., Akhperjanian, A. G., Bazer-Bachi, A. R., et al. 2005b, A&A, 442, 895
- Aharonian, F. A. 2000, *New Astronomy*, 5, 377
- Aharonian, F. A. 2004, *Very high energy cosmic gamma radiation : a crucial window on the extreme Universe*, by F.A. Aharonian. River Edge, NJ: World Scientific Publishing, 2004
- Atoyan, A. M. & Dermer, C. D. 2003, ApJ, 586, 79
- Begelman, M. C., Blandford, R. D., & Rees, M. J. 1984, *Rev. of Mod. Phys.*, 56, 255
- Berge, D. 2006, PhD Thesis, A detailed study of the gamma-ray supernova remnant RX J1713.7–3946 with H.E.S.S.
- Bessell, M. S. 1990, PASP, 102, 1181
- Bettoni, D., Falomo, R., Fasano, G., & Govoni, F. 2003, *New Astronomy Rev.*, 47, 179

- Bevington, P. & Robinson, D. 2003, *Data reduction and error analysis for the physical sciences*, McGraw-Hill Higher Education (McGraw-Hill)
- Blandford, R. D. & Rees, M. J. 1974, *MNRAS*, 169, 395
- Blandford, R. D. & Rees, M. J. 1978, in *BL Lac Objects*, ed. A. M. Wolfe, 328–341
- Błażejowski, M., Blaylock, G., Bond, I. H., et al. 2005, *ApJ*, 630, 130
- Böttcher, M. 2005, *ApJ*, 621, 176
- Boutelier, T., Henri, G., & Petrucci, P.-O. 2008, *MNRAS*, 390, L73
- Brinkmann, W., Maraschi, L., Treves, A., et al. 1994, *A&A*, 288, 433
- Carini, M. T., Miller, H. R., Noble, J. C., & Goodrich, B. D. 1992, *AJ*, 104, 15
- Chadwick, P. M., Lyons, K., McComb, T. J. L., et al. 1999, *ApJ*, 513, 161
- Clements, S. D. & Carini, M. T. 2001, *AJ*, 121, 90
- Courvoisier, T. J.-L., Blecha, A., Bouchet, P., et al. 1995, *ApJ*, 438, 108
- Dai, Y., Wu, J., Zhu, Z.-H., Zhou, X., & Ma, J. 2011, *AJ*, 141, 65
- de Naurois, M. & Rolland, L. 2009, *Astroparticle Physics*, 32, 231
- Dermer, C. D. & Schlickeiser, R. 1993, *ApJ*, 416, 458
- Domínguez, A., Primack, J. R., Rosario, D. J., et al. 2011, *MNRAS*, 410, 2556
- Dominici, T. P., Abraham, Z., Teixeira, R., & Benevides-Soares, P. 2004, *AJ*, 128, 47
- Dunlop, J. S., McLure, R. J., Kukula, M. J., et al. 2003, *MNRAS*, 340, 1095
- Falomo, R., Kotilainen, J. K., Pagani, C., Scarpa, R., & Treves, A. 2004, *ApJ*, 604, 495
- Falomo, R., Pesce, J. E., & Treves, A. 1993, *ApJ*, 411, L63
- Fan, J. H., Xie, G. Z., Pecontal, E., Pecontal, A., & Copin, Y. 1998, *ApJ*, 507, 173
- Fanaroff, B. L. & Riley, J. M. 1974, *MNRAS*, 167, 31P
- Foschini, L., Treves, A., Tavecchio, F., et al. 2008, *A&A*, 484, L35
- Ghisellini, G., Celotti, A., Fossati, G., Maraschi, L., & Comastri, A. 1998, *MNRAS*, 301, 451
- Ghisellini, G. & Madau, P. 1996, *MNRAS*, 280, 67
- Ghisellini, G. & Tavecchio, F. 2008, *MNRAS*, 387, 1669

- Ghisellini, G., Tavecchio, F., Foschini, L., et al. 2010, MNRAS, 402, 497
- Ghisellini, G., Villata, M., Raiteri, C. M., et al. 1997, A&A, 327, 61
- Ghosh, K. K., Ramsey, B. D., Sadun, A. C., & Soundararajaperumal, S. 2000, ApJS, 127, 11
- Giannios, D., Uzdensky, D. A., & Begelman, M. C. 2009, MNRAS, 395, L29
- Giommi, P., Polenta, G., Lähteenmäki, A., et al. 2012, A&A, 541, A160
- Govoni, F., Falomo, R., Fasano, G., & Scarpa, R. 2000, A&A, 353, 507
- Griffiths, R. E., Briel, U., Chaisson, L., & Tapia, S. 1979, ApJ, 234, 810
- Gu, M. F. & Ai, Y. L. 2011, A&A, 534, A59
- Gu, M. F., Lee, C.-U., Pak, S., Yim, H. S., & Fletcher, A. B. 2006, A&A, 450, 39
- Gupta, A. C., Acharya, B. S., Bose, D., Chitnis, V. R., & Fan, J.-H. 2008, Chinese J. Astron. Astrophys., 8, 395
- Hauser, M., Möllenhoff, C., Pühlhofer, G., et al. 2004, Astronomische Nachrichten, 325, 659
- Heck, D., Peirog, T., & Knapp, J. 2012, CORSIKA: An Air Shower Simulation Program, Astrophysics Source Code Library, 1202.006
- Heidt, J., Wagner, S. J., & Wilhelm-Erkens, U. 1997, A&A, 325, 27
- Heitler, W. 1954, Quantum theory of radiation, International Series of Monographs on Physics, Oxford: Clarendon, 1954, 3rd ed.
- Hill, G. J. & Lilly, S. J. 1991, ApJ, 367, 1
- Hillas, A. M. 1985, in International Cosmic Ray Conference, Vol. 3, International Cosmic Ray Conference, ed. F. C. Jones, 445–448
- Hofmann, W., Jung, I., Konopelko, A., et al. 1999, Astroparticle Physics, 12, 135
- Hunter, J. D. 2007, Computing In Science & Engineering, 9, 90
- Ikejiri, Y., Uemura, M., Sasada, M., et al. 2011, PASJ, 63, 639
- Kellermann, K. I., Sramek, R., Schmidt, M., Shaffer, D. B., & Green, R. 1989, AJ, 98, 1195
- Konigl, A. 1981, ApJ, 243, 700
- Krawczynski, H., Hughes, S. B., Horan, D., et al. 2004, ApJ, 601, 151

- Lenain, J.-P., Boisson, C., Sol, H., & Katarzyński, K. 2008, *A&A*, 478, 111
- Li, T.-P. & Ma, Y.-Q. 1983, *ApJ*, 272, 317
- Liu, Y., Jiang, D. R., & Gu, M. F. 2006, *ApJ*, 637, 669
- Longair, M. S. 2010, *High Energy Astrophysics*, Cambridge University Press, 2010
- Mannheim, K. & Biermann, P. L. 1992, *A&A*, 253, L21
- Maraschi, L., Ghisellini, G., & Celotti, A. 1992, *ApJ*, 397, L5
- Marscher, A. P. & Gear, W. K. 1985, *ApJ*, 298, 114
- Massaro, E., Nesci, R., Maesano, M., Montagni, F., & D'Alessio, F. 1998, *MNRAS*, 299, 47
- Miller, H. R. 1981, *ApJ*, 244, 426
- Nakamura, K. & Particle Data Group. 2010, *Journal of Physics G Nuclear Physics*, 37, 075021
- Nalewajko, K., Giannios, D., Begelman, M. C., Uzdensky, D. A., & Sikora, M. 2011, *MNRAS*, 413, 333
- Nolan, P. L., Abdo, A. A., Ackermann, M., et al. 2012, *ApJS*, 199, 31
- Oliphant, T. E. 2007, *Computing in Science & Engineering*, 9, 10
- Osterman, M. A., Miller, H. R., Marshall, K., et al. 2007, *ApJ*, 671, 97
- Osterman Meyer, A., Miller, H. R., Marshall, K., et al. 2009, *AJ*, 138, 1902
- Osterman Meyer, A., Miller, H. R., Marshall, K., et al. 2008, *AJ*, 136, 1398
- Owen, F. N. 1993, in *Lecture Notes in Physics*, Vol. 421, *Jets in Extragalactic Radio Sources*, ed. H.-J. Röser & K. Meisenheimer, 273
- Padovani, P. 1997, *Mem. Soc. Astron. Italiana*, 68, 47
- Paltani, S., Courvoisier, T. J.-L., Blecha, A., & Bratschi, P. 1997, *A&A*, 327, 539
- Pe'er, A. & Waxman, E. 2005, *ApJ*, 628, 857
- Pesce, J. E., Urry, C. M., Maraschi, L., et al. 1997, *ApJ*, 486, 770
- Pian, E., Urry, C. M., Treves, A., et al. 1997, *ApJ*, 486, 784
- Pian, E., Vacanti, G., Tagliaferri, G., et al. 1998, *ApJ*, 492, L17

- Piron, F., Djannati-Atai, A., Punch, M., et al. 2001, in International Cosmic Ray Conference, Vol. 7, 2601
- Pohl, M. & Schlickeiser, R. 2000, A&A, 354, 395
- Raiteri, C. M., Villata, M., Aller, H. D., et al. 2001, A&A, 377, 396
- Rani, B., Gupta, A. C., Strigachev, A., et al. 2010, MNRAS, 404, 1992
- Reimer, A., Böttcher, M., & Postnikov, S. 2005, ApJ, 630, 186
- Richards, J. L., Max-Moerbeck, W., Pavlidou, V., et al. 2011, ApJS, 194, 29
- Sanchez, D. 2010, PhD Thesis, Étude et modélisation des noyaux actifs de galaxie les plus énergétiques avec le satellite Fermi
- Schlafly, E. F. & Finkbeiner, D. P. 2011, ApJ, 737, 103
- Schmidt, M. & Green, R. F. 1983, ApJ, 269, 352
- Schwartz, D. A., Griffiths, R. E., Schwarz, J., Doxsey, R. E., & Johnston, M. D. 1979, ApJ, 229, L53
- Sikora, M. 1994, ApJS, 90, 923
- Sikora, M., Begelman, M. C., Madejski, G. M., & Lasota, J.-P. 2005, ApJ, 625, 72
- Sikora, M., Begelman, M. C., & Rees, M. J. 1994, ApJ, 421, 153
- Sikora, M., Błażejowski, M., Moderski, R., & Madejski, G. M. 2002, ApJ, 577, 78
- Sikora, M., Stawarz, Ł., & Lasota, J.-P. 2007, ApJ, 658, 815
- Takahashi, T., Madejski, G., & Kubo, H. 1999, Astroparticle Physics, 11, 177
- Urry, C. M. 1999, Astroparticle Physics, 11, 159
- Urry, C. M. & Padovani, P. 1995, PASP, 107, 803
- Urry, C. M., Treves, A., Maraschi, L., et al. 1997, ApJ, 486, 799
- Vagnetti, F., Trevese, D., & Nesci, R. 2003, ApJ, 590, 123
- Vercellone, S., Striani, E., Vittorini, V., et al. 2011, ApJ, 736, L38
- Vestrand, W. T., Stacy, J. G., & Sreekumar, P. 1995, ApJ, 454, L93
- Villata, M., Raiteri, C. M., Kurtanidze, O. M., et al. 2004, A&A, 421, 103
- Villata, M., Raiteri, C. M., Kurtanidze, O. M., et al. 2002, A&A, 390, 407

Wagner, S. 2009, in *Astrophysics with All-Sky X-Ray Observations*, ed. N. Kawai, T. Mihara, M. Kohama, & M. Suzuki, 186

Wagner, S. J. & Witzel, A. 1995, *ARA&A*, 33, 163

Wu, J., Peng, B., Zhou, X., et al. 2005, *AJ*, 129, 1818

Wu, J., Zhou, X., Ma, J., et al. 2007, *AJ*, 133, 1599

Zhang, Y. H., Bai, J. M., Zhang, S. N., et al. 2006, *ApJ*, 651, 782



# List of Tables

3.1	Characteristics of the H.E.S.S. telescopes. . . . .	20
4.1	A list of blazars. . . . .	32
4.2	Observations within the long-term monitoring of blazars. . . . .	39
4.3	The summary of blazars luminosities. . . . .	62
5.1	The comparison of mean year values of gamma fluxes in 2004-2012. . . . .	69
5.2	Correlation coefficients for analyzed subsets od data. . . . .	70
5.3	Model parameters for H.E.S.S. spectra in years 2004-2012. . . . .	78

# List of Figures

2.1	The AGN in unified scheme. . . . .	5
2.2	Unified scheme for different AGNs. . . . .	6
3.1	The transparency of the atmosphere. . . . .	14
3.2	A simple model for an electromagnetic shower. . . . .	15
3.3	The electromagnetic and hadronic cascades. . . . .	16
3.4	A view of H.E.S.S.II array. . . . .	19
3.5	Front view of a H.E.S.S.I telescope. . . . .	19
3.6	The safe energy thresholds for selection cuts. . . . .	22
3.7	Hillas parameters and differences between MRSW (mean reduced scaled width) distribution for gamma-ray and hadron induced showers . . . . .	24
3.8	The applied methods of the background estimation. . . . .	25
3.9	An optical depth of EBL . . . . .	27
3.10	The ATOM telescope . . . . .	28
3.11	The ATOM's transmission filter curves. . . . .	29
4.1	A color-magnitude diagram for SHBL J001355.9-185406 . . . . .	40
4.2	A color-magnitude diagram for PKS 0048-097 and RGB J0152+017 . . . . .	41
4.3	A color-magnitude diagram for 1ES 0229+200 and AO 0235+16. . . . .	42
4.4	A color-magnitude diagram for PKS 0301-243 and SHBL J032541.0-164618 . . . . .	43
4.5	A color-magnitude diagram for 1ES 0323+022 and 1ES 0347-121 . . . . .	44
4.6	A color-magnitude diagram for 1ES 0414+00.9 and PKS 0447-439 . . . . .	45
4.7	A color-magnitude diagram for PKS 0537-441 and PKS 0548-322 . . . . .	46
4.8	A color-magnitude diagram for PKS 0735+178 and OJ 287 . . . . .	47
4.9	A color-magnitude diagram for SHBL J101015.9-311908 and 1ES 1101-232 . . . . .	48
4.10	A color-magnitude diagram for Markarian 421 and 1ES 1218+304 . . . . .	49
4.11	A color-magnitude diagram for W Comae and 1ES 1312-423 . . . . .	50
4.12	A color-magnitude diagram for PKS 1424+240 and AP Librae . . . . .	51
4.13	A color-magnitude diagram for PG 1553+113 and Markarian 501 . . . . .	52
4.14	A color-magnitude diagram for RGB J1725+118 and PKS 2005-489 . . . . .	53
4.15	A color-magnitude diagram for SHBL J213135.4-091523 and BL Lacertae . . . . .	54

<i>List of Figures</i>	105
4.16 A color-magnitude diagram for PKS 2155-304 . . . . .	55
4.17 Comparison of radio, optical and gamma-ray luminosities of the ATOM blazars. 57	
4.18 Comparison of the radio, optical and gamma-ray luminosities of the ATOM blazars. . . . .	58
4.19 Comparison of the gamma-ray spectral index and optical luminosity. . . . .	59
4.20 Comparison of the gamma-ray luminosity and $B - R$ optical color. . . . .	59
4.21 The optical luminosity versus the $B - R$ optical color. . . . .	60
4.22 The radio luminosity versus the $B - R$ optical color. . . . .	60
4.23 The comparison of the optical luminosity of the ATOM blazars and color- magnitude correlation coefficient. . . . .	61
5.1 The visibility of PKS 2155-304 in 2012 . . . . .	64
5.2 The long-term H.E.S.S. light curve. . . . .	65
5.3 The H.E.S.S. light curves for 2004, 2005, 2006. . . . .	66
5.4 The H.E.S.S. light curves for 2007, 2008, 2009. . . . .	67
5.5 The H.E.S.S. light curves for 2010, 2011, 2012. . . . .	68
5.6 ATOM and H.E.S.S. light curves intervals A-D. . . . .	71
5.7 ATOM and H.E.S.S. light curves intervals E-H. . . . .	72
5.8 ATOM and H.E.S.S. light curves intervals I-L. . . . .	73
5.9 Long-term ATOM and H.E.S.S. light curves. . . . .	74
5.10 Comparison of gamma flux and optical $B - R$ color. . . . .	75
5.11 The 2004-2007 spectral for PKS 2155-304 obtained with H.E.S.S. data. . . . .	76
5.12 The 2008-2012 spectral for PKS 2155-304 obtained with H.E.S.S. data. . . . .	77
5.13 Spectral energy distrution for VHE gamma and optical observations. . . . .	79
6.1 Color-magnitude diagram for PKS 0301-243. . . . .	82
6.2 Color-magnitude diagram for PKS 2005-489. . . . .	83
6.3 Color-magnitude diagram for PKS 0537-441. . . . .	84
6.4 Average broad-band SEDs of PKS 2155-304 for the years 2007, 2008, and 2009. 86	
A.1 The color scale used in color-magnitude diagrams. . . . .	90
A.2 The explanation of color coding in color-magnitude diagrams. . . . .	91
B.1 A histogram of the set of Pearson's correlation coefficients. . . . .	93